DECIPHERING THE KALEIDOSCOPIC UNIVERSE WITH MULTIMESSENGER PHYSICS

by

Cyril Creque-Sarbinowski

A dissertation submitted to The Johns Hopkins University in conformity with the requirements for the degree of Doctor of Philosophy

Baltimore, Maryland

July 2022

Abstract

Cosmology is entering a new era as the number and precision of probes perpetually increase. Long-standing probes, such as the cosmic microwave background (CMB) and galaxy surveys, are cultivating high-precision tests for a wide array of cosmological models. Gravitational waves (GW), line-intensity mapping (IM), and other more recent probes are beginning to yield intricate astrophysical information about the creation of their distinct signals. In the upcoming decade, potential probes, such as active galactic nuclei (AGN) and neutrinos, will see favorable improvements in their characterizations. My research interests span across the various theoretical analyses of these types of probes, as each reveals a unique and complementary slice of information about the Universe. These slices, together, further complete a picture of the entire Universe, as well as cross-check the conclusions drawn from any single probe. Thus far, I have tested astrophysical and inflationary signatures with CMB secondaries; constrained dark matter and the anomalous EDGES signal with IM; characterized AGN variability with time-domain astronomy; and investigated

ABSTRACT

the nature of astrophysical neutrinos with optical and neutrino telescopes.

Primary Reader and Advisor: Marc Kamionkowski

Secondary Reader: Emanuele Berti

Acknowledgments

I'm no wordsmith. Here's a list of people I greatly appreciate and would like to thank for supporting me in my journey through graduate school and research: Marc Kamionkowski, Byron Freelon, Ibrahima Bah, Ely Kovetz, Yacine Ali-Haïmoud, Jeff Hyde, Albert Ratner, Bei Zhou, Chanda Prescod-Weinstein, and Stephon Alexander. I would also like to thank the Gates Millennium Scholars Program, the National Science Foundation, and the Simons Foundation for funding either me or my research.

Contents

List of Tables

List of Figures

Chapter 1

Introduction

The current era of cosmology is equipped to tackle questions arising from multiple sectors - from astronomy to particle physics - at high precision. This era has been ushered in by the development of a multitude of experiments in the electromagnetic, gravitational, and neutrino observational windows and, moving forward, will continue to increase in scope. In this thesis, I will present multiple different avenues of using current and future cosmological probes to answer fundamental questions in the Universe. In particular, I will focus on three different types of cosmological probes: line-intensity mapping, active galactic nuclei, and neutrinos.

In Chapter 2 I discuss the use of line-intensity mapping in cosmology (IM). The purpose of IM, an emerging tool for extragalactic astronomy and cosmology, is to measure the integrated emission along the line of sight from spectral

lines emitted from galaxies and the intergalactic medium. The observed frequency of the line then provides a distance determination allowing the three-dimensional distribution of the emitters to be mapped. In Sec. 2.1 I discuss the possibility to use these measurements to seek monoenergetic photons from dark-matter decay or possibly annihilation. The photons from decays or annihilations (should such lines arise) will be correlated with the mass distribution, which can be determined from galaxy surveys, weak-lensing surveys, or the IM mapping experiments themselves. I discuss how to seek this cross-correlation and then estimate the sensitivity of various IM experiments in the dark-matter mass-lifetime parameter space. I find prospects for improvements of nine orders of magnitude in sensitivity to decaying/annihilating dark matter in the frequency bands targeted for IM experiments.

In addition, heat transfer between baryons and millicharged dark matter has been invoked as a possible explanation for the anomalous 21-cm absorption signal seen by the IM experiment EDGES. Prior work has shown that the solution requires that millicharged particles make up only a fraction $(m_\chi/\mathrm{MeV})\,0.0115\% \lesssim f \lesssim 0.4\%$ of the dark matter and that their mass m_χ and charge q_χ have values $0.1 \lesssim (m_\chi/\mathrm{MeV}) \lesssim 10$ and $10^{-6} \lesssim (q_\chi/e) \lesssim 10^{-4}$. In Sec 2.2 I show that such particles come into chemical equilibrium before recombination, and so are subject to a constraint on the effective number N_{eff} of relativistic degrees of freedom, which we update using Planck 2018 data.

I moreover determine the precise relic abundance f that results for a given mass m_χ and charge q_χ and incorporate this abundance into the constraints on the millicharged-dark-matter solution to the EDGES signal. With these two results, the solution is ruled out if the relic abundance is set by freeze-out.

Moving onto the next probe, I show the prospects of learning about active galactic nuclei (AGN) with the Vera C. Rubin Observatory (Rubin) in Chapter 3. Over the next ten years, Rubin will observe $\sim$10 million AGN with a regular and high cadence. During this time, the intensities of most of these AGN will fluctuate stochastically. Here, we explore the prospects to quantify precisely these fluctuations with Rubin measurements of AGN light curves. To do so, we suppose that each light curve is described by a damped random walk with a given fluctuation amplitude and correlation time. Theoretical arguments and some current measurements suggest that the correlation timescale and fluctuation amplitude for each AGN may be correlated with other observables. We use an expected-information analysis to calculate the precision with which these parameters will be inferred from the measured light curves. We find that the measurements will be so precise as to allow the AGN to be separated into up to ~ 10 different correlation-timescale bins. We then show that if the correlation time varies as some power of the luminosity, the normalization and power-law index of that relation will be determined to $\mathcal{O}(10^{-4}\%)$. These results suggest that with Rubin, precisely measured variability parameters will

take their place alongside spectroscopy in the detailed characterization of individual AGN and in the study of AGN population statistics. Analogous analyses will be enabled by other time-domain projects, such as CMB-S4.

Lastly, I demonstrate the capability of current and future neutrino telescopes to infer properties about neutrinos and their astrophysical sources in Chapter 4. If neutrinos have self-interactions, these will induce scatterings between astrophysical and cosmic neutrinos. Prior work proposed looking for possible resulting resonance features in astrophysical neutrino spectra in order to seek a neutrino self-interaction which can be either diagonal in the neutrino flavor space or couple different neutrino flavors. The calculation of the astrophysical spectra involves either a Monte Carlo simulation or a computationally intensive numerical integration of an integro-partial-differential equation. As a result only limited regions of the neutrino self-interaction parameter space have been explored, and only flavor-diagonal self-interactions have been considered. In Sec 4.1, I present a fully analytic form for the astrophysical neutrino spectra for arbitrary neutrino number and arbitrary self-coupling matrix that accurately obtains the resonance features in the observable neutrino spectra. The results can be applied to calculations of the diffuse supernova neutrino background and of the spectrum from high-energy astrophysical neutrino sources. I illustrate with a few examples.

In addition, active galactic nuclei (AGN) are a promising source for high-

energy astrophysical neutrinos (HEANs).In Sec 4.2, I evaluate the capacity of Rubin, in tandem with various current and upcoming neutrino telescopes, to establish AGN as HEAN emitters. To do so, I assume that the neutrino luminosity from any given AGN at any given time is proportional to the electromagnetic luminosity. I then estimate the error with which this fraction can be measured through spatial and temporal cross-correlation of Rubin light curves with IceCube, KM3NeT, and Bakail-GVD. I find that it may be possible to detect AGN contributions at the $\sim 3\sigma$ level to the HEAN flux even if these AGN contribute only $\sim 10\%$ of the HEAN flux. The bulk of this information comes from spatial correlations, although the temporal information improves the sensitivity a bit. The results also imply that if an angular correlation is detected with high signal-to-noise, there may be prospects to detect a correlation between AGN variability and neutrino arrival times. The small HEAN fraction estimated here to be accessible to the entirety of the Rubin AGN sample suggests that valuable information on the character of the emitting AGN may be obtained through similar analyses on different sub-populations of AGN.

Moreover, cosmic strings that couple to neutrinos may account for a portion of the high-energy astrophysical neutrino (HEAN) flux seen by IceCube. In Sec 4.3 I calculate the observed spectrum of neutrinos emitted from a population of cosmic string loops that contain quasi-cusps, -kinks, or kink-kink collisions. I consider two broad neutrino emission models: one where these

string features emit a neutrino directly, and one where they emit a scalar particle which then eventually decays to a neutrino. In either case, the spectrum of cosmic string neutrinos does not match that of the observed HEAN spectrum. I thus find that the maximum contribution of cosmic string neutrinos, through these two scenarios, to be at most $\sim 30\%$ of the observed flux. However, I also find that the presence of cosmic string neutrinos can lead to bumps in the observed neutrino spectrum. Finally, for each of the models presented, I present the viable parameter space for neutrino emission.

Chapter 2

Line-Intensity Mapping (LIM)

2.1 Decaying and Annihilating DM

Measurements of the cosmic microwave background (CMB) temperature and polarization angular power spectra agree at the percent level with the predictions of ΛCDM, a six-parameter phenomenological model [3, 4]. However, the nature of the cold dark matter required by the model remains a mystery. It could be primordial black holes [5–7], axions [8–12], sterile neutrinos [13], weakly interacting massive particles [14–16], something related to baryons [17], or any of a rich array of other possibilities [18]. There is, however, no prevailing frontrunner among this vast assemblage of ideas, and so any empirical avenue that might provide some hint to the nature of dark matter should be pursued.

In some scenarios a feeble, but nonzero, electromagnetic coupling of the dark-matter particle allows it to decay to a photon line. For example, the axion undergoes two-photon decay, and there are ideas (e.g., axion-mediated dark-photon mixing [19–22]) in which the standard axion phenomenology may be extended. Monoenergetic photons may be emitted in the decay of sterile-neutrino dark matter [13], and there are other ideas (e.g., exciting dark matter [23]) in which two dark-matter states are connected by emission of a photon of some fixed energy. It is also conceivable that monoenergetic photons might be produced in dark-matter annihilation. These possibilities have fueled an extensive search for cosmic-background photons from dark-matter decays or annihilations at an array of frequencies through an array of techniques, among them searches in the extragalactic background light [24–26].

In this work, we propose to use line-intensity mapping (IM) [27–29], an emerging technique in observational cosmology, to seek radiative dark-matter decays/annihilations in the extragalactic background light. Intensity-mapping experiments measure the brightness of a given galactic emission line as a function of position on the sky and observer frequency (which provides a proxy for the distance) to infer the three-dimensional distribution of the emitters. A considerable intensity-mapping effort with neutral hydrogen's 21-cm line is already underway [30], and efforts are now afoot to develop analogous capabilities with CO and CII molecular lines, hydrogen's Hα line (e.g., with SPHEREx

[31], now in a NASA Phase A MidEx study), and others. If dark matter decays or annihilates to a line, the resulting photons will be correlated with the mass distribution, which can be inferred from galaxy surveys, weak-gravitational-lensing maps, or from the intensity-mapping surveys themselves.

Our work follows in spirit Refs. [32, 33], who sought a cross -correlation of an axion decay line with the mass distribution within a given galaxy cluster, but substitutes the cosmic mass distribution for the mass distribution within an individual cluster. We extend on Ref. [34] which sought angular infrared-background-light fluctuations from dark-matter decay, by our inclusion of frequency dependence and cross-correlation with the three-dimensional mass distribution. We take here a theorist's perspective, initially exploring possibilities limited only by astrophysical backgrounds and assuming perfect measurements. Doing so, we find the potential for improvements over current sensitivities of up to nine orders of magnitude, in frequency bands targeted by forthcoming IM efforts. We then show that the improvements in sensitivity are still dramatic even after taking into account the effects of realistic instrumental noise.

This section is organized as follows: In Section 2.1.1 we discuss the basic idea and make some simple estimates. Section III then adds several additional ingredients required to make connection with realistic experiments. We moreover provide here quantitative estimates for several representative

experiments. The results are discussed in Section 2.1.3. We discuss briefly particle-physics models the search may be relevant for and show, for example, that SPHEREx has potential to probe hitherto unexplored regions of the axion coupling for axion masses $\sim$ eV.

2.1.1 Calculation

Consider a Big Bang relic of mass m_χ that decays with a rate Γ to a final state with a photon of energy $E_\gamma = h\nu_0$. We assume here the particle to be long-lived compared with the age of the Universe (i.e., $\Gamma \lesssim H_0 \simeq 10^{-18}$ sec^{-1}) so that the density of the decaying particles is $\rho_\chi(t) = \rho_{\chi 0} a^{-3}$ with the scale factor $a(t)$ (normalized to $a(t_0) = 1$), given as a function of time t. Here $\rho_{\chi 0} = \rho_\chi(t_0)$, and t_0 is the time today. It is also conceivable that the Big Bang produced some other relic particle that decays with a lifetime $\tau = \Gamma^{-1} \lesssim H_0^{-1}$ and IM can be used to seek such short-lived particles as well, although we do not consider this possibility here.

2.1.1.1 Isotropic specific intensity

We now calculate the isotropic specific intensity of decay photons today. The specific luminosity density (energy density per unit time per unit frequency interval) due to decays is $\epsilon_\nu(t) = \zeta \Gamma \rho_\chi(t) \theta(\nu - \nu_0)$, where $\zeta = (h\nu_0/m_\chi c^2)$ is the fraction of energy transferred away to photons, and $\theta(\nu)$ is the line profile of

the signal.[1] We take $\theta(\nu)$ to be the Dirac delta function. The specific intensity observed at frequency ν and $z = 0$ is given by the solution [35,36],

$$I_\nu = \frac{1}{4\pi}\int_0^\infty dz \frac{c}{H(z)}\frac{\epsilon_{\nu(1+z)}(z)}{(1+z)^4}, \tag{2.1}$$

to the radiative-transfer equation, where $H(z)$ is the Hubble parameter at redshift z, and we have used z as a proxy for t. For dark-matter-decay photons, this expression evaluates to

$$I_\nu = \frac{c}{4\pi\nu_0}\frac{\Gamma}{H_0}\frac{\rho_\chi(z)}{E(z)(1+z)^4}\bigg|_{z=\frac{\nu_0}{\nu}-1}, \tag{2.2}$$

where $H(z) \equiv H_0 E(z)$, and for ΛCDM, $E(z) = [\Omega_m(1+z)^3 + (1-\Omega_m)]^{1/2}$, with Ω_m the matter-density parameter today. Using $\rho_{\chi 0} = f\Omega_c\rho_c$, where ρ_c is the critical energy density of the Universe, Ω_c the fraction of critical density in dark matter, and f the fraction of dark matter today in decaying particles, the specific intensity evaluates, using Planck 2015 parameters, to

$$\nu I_\nu = 2.4\times10^{-3}\,\mathrm{W\,m^{-2}\,sr^{-1}}\,\frac{\nu}{\nu_0}\frac{\Gamma}{H_0}\frac{f\zeta}{E(z)\,(1+z)}\bigg|_{z=\frac{\nu_0}{\nu}-1}. \tag{2.3}$$

The intensity is nonzero only for frequencies $\nu \le \nu_0$.

The specific fluence (number flux of photons, over all directions, per unit

[1] If the particle, like the axion, decays to two photons, this expression is multiplied by 2. Thus, two-photon decays can be accommodated in all subsequent expressions by replacing $\zeta \to 2\zeta$.

frequency interval) is $F_\nu = 4\pi I_\nu/(h\nu)$, and the total fluence (over all photon directions) is $F = \int F_\nu \, d\nu$. For example, for $f = 1$, $m_\chi c^2 = 1$ eV, $\zeta = 1/2$, and $\Gamma = H_0$, the total fluence evaluates to 2.9×10^{17} m^{-2} sec^{-1}.

2.1.1.2 Cross-correlation with mass distribution

Photons from dark-matter decay must be distinguished from a huge background of photons in the extragalactic background. We propose here to use the cross-correlation of these decay photons (which trace the dark-matter distribution) with some tracer of the large-scale mass distribution to distinguish decay photons from those in the extragalactic background.

We now calculate the smallest number of decay photons that need to be detected to establish their correlation with large-scale structure. To do so, we assume that we have sampled the distribution of mass over a cosmological volume V with a matter-tracer population (e.g., galaxies) that has a mean number density $\bar{n}_g$ and bias b. The fractional mass-density perturbation is $\delta(\vec{x})$ with Fourier transform $\tilde{\delta}(\vec{k}) = \int d^3x \, \delta(\vec{x}) e^{i\vec{k}\cdot\vec{x}}$, so that the matter power spectrum $P(k)$ is then obtained from $\tilde{\delta}(\vec{k})\delta^*(\vec{k}') = (2\pi)^3 \delta_D(\vec{k} - \vec{k}') P(k)$, with $\delta_D(\vec{k})$ the 3-dimensional Dirac delta function. The power spectrum for the tracer population is $b^2 P(k) + \bar{n}_g^{-1}$, where we have added a Poisson contribution due to the finite number density of the tracer population [36].

The same matter-density field is also sampled in the IM experiment by the

photons observed from dark-matter decay. We surmise that there are $N_\chi = \xi N_\gamma$ such photons that appear in the experiment, in addition to $N_b = (1-\xi)N_\gamma$ photons from the extragalactic background light (EBL), the integrated light from galaxies. Here N_γ is the total number of observed photons, and the EBL has a frequency spectrum described in Refs. [26, 37, 38]. The galaxies that give rise to this EBL are a biased tracer of the mass distribution and so will also be clustered. However, the light from a given galaxy is broadly distributed over frequencies and so the EBL-photon distribution in the IM angular-frequency space is smoothed. We therefore suppose that the background photons are uniformly distributed throughout the volume. We also add to the EBL, for measurements at frequencies $\nu \lesssim 100$ GHz, Galactic synchrotron radiation, which we model roughly in terms of a brightness temperature $T_B = 1000\,\mathrm{K}\,(\nu/100\,\mathrm{MHz})^{-2.5}$.

The fractional luminosity density perturbation in the *observed* photon population is then $\delta_\gamma = N_\chi/(N_\chi + N_b)\delta = \xi\tilde{\delta}$. It follows that the cross-correlation between the observed photons and tracers is

$$\tilde{\delta}_g(\vec{k})\tilde{\delta}^*_\gamma(\vec{k}') = (2\pi)^3\delta_D(\vec{k}-\vec{k}')\,\xi b P(k); \tag{2.4}$$

i.e., the photon-tracer cross-correlation has a power spectrum $P_{g\gamma}(k) = b\xi P(k)$.

To seek this cross-correlation, we take the Fourier amplitudes $\tilde{\delta}_g(\vec{k})$ (from

the tracer survey) and $\tilde{\delta}_\gamma(\vec{k})$ (from the IM experiment, for some nominal decay frequency ν_0) for each wavevector $\vec{k}$. Their product then provides an estimator for $P_{g\gamma}(k)$ with variance,

$$[P_{g\gamma}(k)]^2 + \left[P_{\gamma\gamma}(k) + \bar{n}_\gamma^{-1}\right]\left[P_{gg}(k) + \bar{n}_g^{-1}\right]. \tag{2.5}$$

Here, $\bar{n}_\gamma = N_\gamma/V$ is the number of photons collected divided by the volume surveyed, and $P_{\gamma\gamma}(k) = \xi^2 P(k)$. If we write $P(k) = Ak^{n_s}\left[T(k)\right]^2$, in terms of the scalar spectral index $n_s \simeq 0.96$, the ΛCDM transfer function $T(k)$, and amplitude A, then the estimator from this Fourier mode for $P_{g\gamma}(k)$ provides an estimator for the product ξb, and thus (if b is known) for ξ. The minimum-variance estimator for ξ is then obtained by adding the estimators from each $\vec{k}$ mode with inverse-variance weighting.

Since the signal for each Fourier mode is $\xi b P(k)$, the squared signal-to-noise with which the cross-correlation can be measured with the minimum-variance estimator is

$$\left(\frac{S}{N}\right)^2 = \sum_{\vec{k}} \frac{\left[\xi b P(k)\right]^2/2}{\left[\xi b P(k)\right]^2 + \left(\xi^2 P(k) + \bar{n}_\gamma^{-1}\right)\left(b^2 P(k) + \bar{n}_g^{-1}\right)}. \tag{2.6}$$

To distinguish a detection from the null hypothesis $\xi = 0$, we evaluate the noise under this null hypothesis and then estimate the sum by approximating $b^2P(k)/\left[b^2P(k) + \bar{n}_g^{-1}\right] = 1$ for $b^2P(k) > \bar{n}_g^{-1}$ and $b^2P(k)/\left[b^2P(k) + \bar{n}_g^{-1}\right] = 0$

for $b^2 P(k) < \bar{n}_g^{-1}$. Doing so, we find that the cross-correlation between decay photons and the tracer population can be measured with a signal to noise

$$(S/N) = \xi \sqrt{N_b \sigma_k^2 / 2}, \tag{2.7}$$

where $\sigma_k^2 \simeq (2\pi^2)^{-1} \int^{k_{\rm max}} k^2 P(k)\, dk$ is the variance of the mass distribution on a distance scale $k_{\rm max}^{-1}$ determined from $P(k_{\rm max}) = (b^2 \bar{n}_g)^{-1}$. Fig. 2.1 shows the dependence of σ_k on the tracer number density $\bar{n}_g$ and its bias b.

Since the scheme suggested here involves *cross*-correlation of a putative decay line with a tracer of the matter distribution, the measurement is limited *not* by the number of Fourier modes of the density field that can be well sampled, but only by the fidelity with which the density field can be sampled and by the number of photons observed. Moreover, the factor σ_k^2 in any measurement is really the variance of the density field, as determined by the tracer survey, in the volume surveyed.

The condition for a $\gtrsim 2\sigma$ detection of a decay-line signal is

$$\xi \gtrsim \xi_{\rm min} \simeq 2 (N_b \sigma_k^2 / 2)^{-1/2}. \tag{2.8}$$

Since the intensity I_ν from dark-matter decay and the EBL intensity $I_\nu^{\rm CB}$ both vary smoothly with frequency, we approximate $\xi = N_\chi / (N_\chi + N_b) \simeq N_\chi / N_b$ as $\xi \simeq I_\nu / I_\nu^{\rm CB}$. We then require, for detection of a signal, $I_{\nu_0} \gtrsim \xi_{\rm min} I_{\nu_0}^{\rm CB}$, with I_ν

taken from Eq. (2.3), and evaluated at the frequency ν_0 at which (for $\Gamma \lesssim H_0$) it peaks. A cross-correlation can then be detected if the decay lifetime is

$$\begin{aligned}\tau \equiv \Gamma^{-1} &\lesssim \frac{f\zeta H_0^{-1} c}{8\sqrt{2}\pi}\sqrt{N_b \sigma_k^2}\left[\frac{\Omega_c \rho_c}{\nu_0 I_{\nu_0}^{\rm CB}}\right] \\ &\simeq 7.5\times 10^{32}\frac{f\zeta\sigma_k (N_b/10^{20})^{1/2}}{(\nu_0 I_{\nu_0}^{\rm CB}/10^{-8}\,{\rm W\ m^{-2}\ sr^{-1}})}\,{\rm sec}. \end{aligned} \tag{2.9}$$

Here, N_b is the number of EBL photons from the fraction $f_{\rm sky}$ of the sky observed with frequencies $\nu_1 \le \nu \le \nu_2$ that cross a detector area A in time T; i.e.,

$$N_b = 4\pi f_{\rm sky} A T \int_{\nu_1}^{\nu_2} d\nu\, I_\nu^{\rm CB}/(h\nu). \tag{2.10}$$

2.1.1.3 Order-of-magnitude estimates and scalings

We now work out some order-of-magnitude estimates. Consider a tracer survey that samples galaxies in a volume to redshift $z \sim 1$, over $f_{\rm sky}$ of the sky. If the galaxy density is $\gtrsim 0.01$ Mpc^{-3}, then we will have, $k_{\rm max} \gtrsim 0.1$ Mpc^{-1}, for which $\sigma_k \gtrsim 1$ (and we take $b \sim 1$). We consider an intensity-mapping experiment with a frequency range broad enough to detect decay photons over the redshift range $0 \le z \le 1$, and at frequencies $\nu \sim 10^{14}$ Hz (roughly optical, probed by SPHEREx). From Fig. 9 in Ref. [38] we ballpark (conservatively) the EBL intensity as $\nu I_\nu^{\rm CB} \sim 10^{-8}$ W m^{-2} sr^{-1} and fluence (over all photon direc-

tions) as 10^{12} m^{-2} s^{-1}. We imagine a detector of area $A_{\rm m}$ m^2 and observation time $T_{\rm yr}$ yr. From Eq. (2.7), we then estimate the smallest detectable fraction of decay photons ξ to be $\xi_{\rm min} \sim 5 \times 10^{-10} (f_{\rm sky} A_{\rm m} T_{\rm yr})^{-1/2}$ (at 2σ). Comparing the EBL fluence with our prior result, $\sim 3 \times 10^{17}$ m^{-2} s^{-1}, for the fluence from dark-matter decay with $h\nu_0 \sim$ eV, $f\zeta = 1/2$, and $\Gamma = H_0$, we infer the largest detectable lifetime for such a measurement to be

$$\tau_{\rm max} \simeq 10^{33}\, f\zeta (f_{\rm sky} A_{\rm m} T_{\rm yr})^{1/2} {\rm sec}. \tag{2.11}$$

Note that this is $\xi_{\rm min}^{-1} \sim 10^9$ times better than the limit inferred by simply requiring the decay-line intensity to be smaller than the observed EBL intensity at ν_0 and $\sim 10^8$ times better than the strongest current bounds from null searches for decay lines from galaxy clusters [33].

As Eq. (2.11) indicates the sensitivity scales with the square root of the area on the sky, the area of the detector, and the duration of the experiment—i.e., with the square root of the the total number of background photons—as expected. There is also a dependence on σ_k, although this is weak. As Fig. 2.1 shows, the dependence of σ_k with $k_{\rm max}$ is roughly linear for values $k_{\rm max} \sim 0.1$ Mpc^{-1}, and $\tau_{\rm max}$ depends linearly on σ_k: a greater density contrast makes a cross-correlation more easily detectable.

The linear-theory calculation here may be seen as conservative, given that

nonlinear evolution enhances the power spectrum on smaller scales. On the other hand, as one goes to smaller scales, the fidelity with which a population traces the mass distribution decreases. The numerical estimate above, which used a value $\sigma_k \sim 1$, makes the conservative assumption that only information from the linear regime is used.

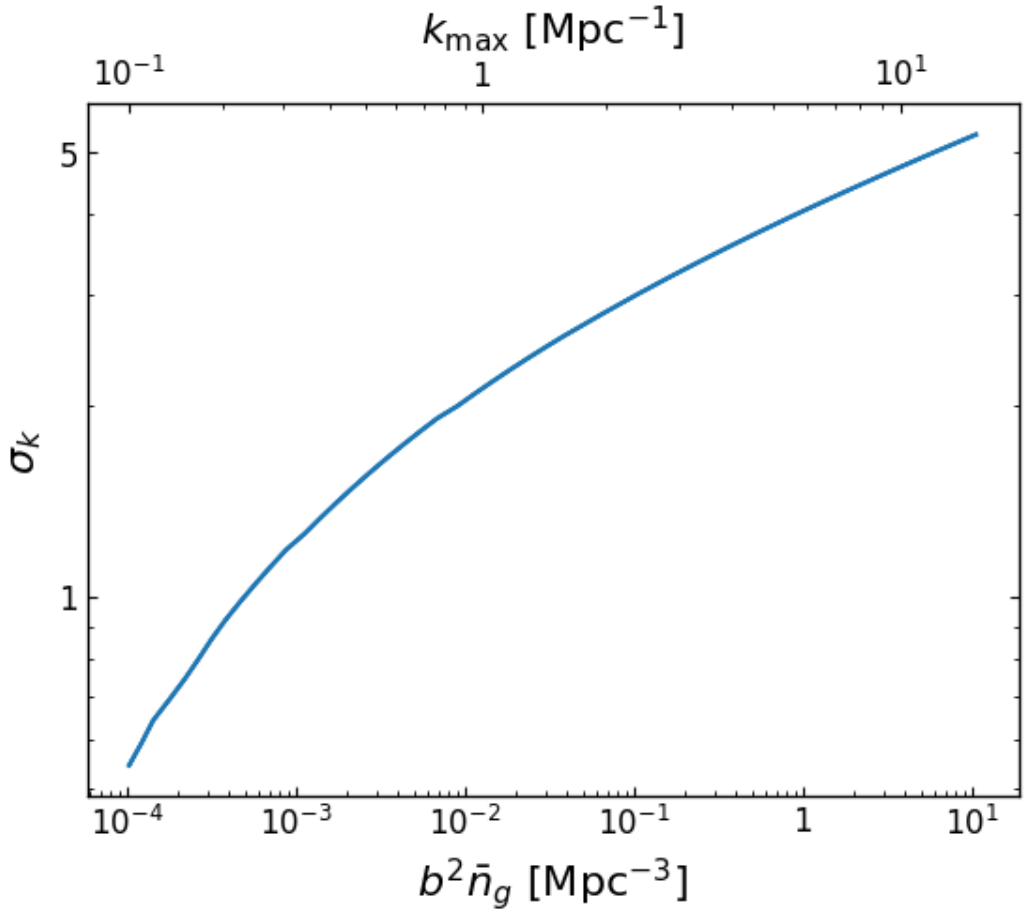

Figure 2.1: The dependence of the mass-density root-variance σ_k on the tracer-population spatial density $\bar{n}_g$ and its bias b.

2.1.2 Forecasts for experiments

To make the next step in connection to realistic experiments, we now consider the spatial resolution of the experiment and, moreover, the anisotropy in the spatial resolution of the cosmic volume probed. This anisotropy arises because the spatial resolution of the experiment in the radial direction is fixed by the frequency resolution; this most generally differs from the spatial resolution in directions transverse to the line of sight, which are fixed by the angular resolution. To account for these effects, we define wavenumbers $k_{\mathrm{max},||}$ and $k_{\mathrm{max},\perp}$ in the line-of-sight and transverse directions, respectively. These are fixed by the frequency and angular resolutions of the experiment. If these wavenumbers are larger than k_{max} from the finite tracer number density (discussed above), then the effective resolution is fixed by finite tracer number density. If they are smaller, then the resolution is fixed by the survey resolutions. That is, we replace the k_{max} we derived above by

$$\begin{aligned}\tilde{k}_{\mathrm{max},||} &\equiv \min\left[k_{\mathrm{max}}, k_{\mathrm{max},||}\sqrt{1-(k_\perp/k_{\mathrm{max},\perp})^2}\right], \\ \tilde{k}_{\mathrm{max},\perp} &\equiv \min\left[k_{\mathrm{max}}, k_{\mathrm{max},\perp}\right],\end{aligned} \tag{2.12}$$

and then model the Fourier-space volume as an ellipse with the corresponding principal semi-axes. Explicitly, this is

$$\sigma_k^2 = \frac{1}{2\pi^2} \int^{\tilde{k}_{\mathrm{max},\perp}} \int^{\tilde{k}_{\mathrm{max},||}} k_\perp P\left(\sqrt{k_{||}^2 + k_\perp^2}\right) dk_\perp dk_{||}. \tag{2.13}$$

The maximum parallel and perpendicular wavenumbers are most generally redshift-dependent, and if so, then we need an integration in Eq. (2.7) also over cocentric ellipsoidal shells with thickness given by the spectral resolution and parametrized by redshift. However, given the rough nature of our calculation, we approximate the wavenumbers as constant in redshift as

$$\begin{aligned} k_{\mathrm{max},||} &= RH(z)/[c(1+z)] \approx RH_0/c, \\ k_{\mathrm{max},\perp} &= [r_c(z)\theta_{\mathrm{res}}]^{-1} \approx [r_c(0)\theta_{\mathrm{res}}]^{-1}, \end{aligned} \tag{2.14}$$

where $r_c(z)$ is the comoving size of the Universe at redshift z, R the spectral resolution, and θ_{res} the pixel resolution of the experiment.

The last step is to estimate the effects of instrumental noise on the measurement. We do so by supposing that instrument noise distributes N_{n} photons, in addition to the N_b EBL photons, uniformly in the survey volume. The fraction ξ of decay photons from the sky now gets replaced by a fraction $\xi^{\mathrm{obs}} =$

$N_\chi/(N_\chi+N_b+N_{\rm n}) = \xi(N_\chi+N_b)/(N_\chi+N_b+N_{\rm n})$ of the observed (decay plus EBL plus instrumental-noise) photons that come from decays. Following the same reasoning as above, the smallest detectable $\xi^{\rm obs}$ is $\xi^{\rm obs}_{\rm min} = 2\sqrt{2}\sqrt{N_b+N_{\rm n}}/(N_b\sigma_k)$. The expression, Eq. (2.8), for the smallest detectable ξ, then becomes,

$$\xi_{\rm min} \simeq 2(N_b\sigma_k^2/2)^{-1/2}\sqrt{1+(N_{\rm n}/N_b)}, \tag{2.15}$$

after taking into account the $N_{\rm n}$ additional noise photons. We can estimate the ratio $(N_{\rm n}/N_b) \simeq (I^{\rm n}_\nu/I^{\rm CB}_\nu)$ in terms of an instrument-noise intensity $I^{\rm n}_\nu$ which can be parameterized in terms of the Planck function $B_\nu(T_{\rm eff})$ at a given effective system temperature $T_{\rm eff}$. As Eq. (2.15) indicates, if $I^{\rm n}_{\nu_0} \lesssim I^{\rm CB}_{\nu_0}$, then instrument noise does not degrade the sensitivity. If $I^{\rm n}_{\nu_0} \gtrsim I^{\rm CB}_{\nu_0}$, then instrument noise reduces the smallest detectable τ, given in Eq. (2.9), by a factor $(I^{\rm CB}_{\nu_0}/I^{\rm n}_{\nu_0})^{1/2}$.

We now use Eq. (2.9), the cosmic background photon distribution in Ref. [38], and the experimental parameters shown in Table 2.1 to forecast lifetime sensitivities for an array of intensity-mapping experiments that are being pursued or under consideration. The array of experiments is chosen to illustrate the different frequencies (and the principal target astrophysical emission lines) being targeted by current intensity-mapping efforts. The representative efforts are CHIME [30]; CCAT-prime [39]; COMAP [40]; STARFIRE [41]; and SPHEREx [31]. There are, however, a number of other projects, and several

other lines, in other frequency windows, that may be targets for IM efforts—see Ref. [29] for a more comprehensive list. We also caution that the planning for some experiments is not yet complete, and so the detailed parameters may change.

The results are shown in Fig. 2.2. The experimental parameters we use for these estimates are the survey exposure, the frequency ranges probed, the sky coverage, and the angular/frequency resolutions. We include the dependence of the redshift range probed via the emitted photon's energy and observed frequency range. We assume that that $\sigma_k = 2.3$ for some tracer population (corresponding to $k_{\rm max} = 1.2$ Mpc^{-1}), but take into account the (possibly direction-dependent) modification of $k_{\rm max}$ determined by the angular and frequency resolution of the experiment. For each experiment, we show two curves, one that includes the estimated effects of instrumental noise, and another, more optimistic, curve that indicates the limit, from the EBL, for an experiment with similar exposure and sky and frequency coverage, but with no instrumental noise. We also plot in Fig. 2.2 a current conservative lower bound to τ inferred simply by demanding that the decay-line intensity be less than the observed EBL intensity at ν_0.

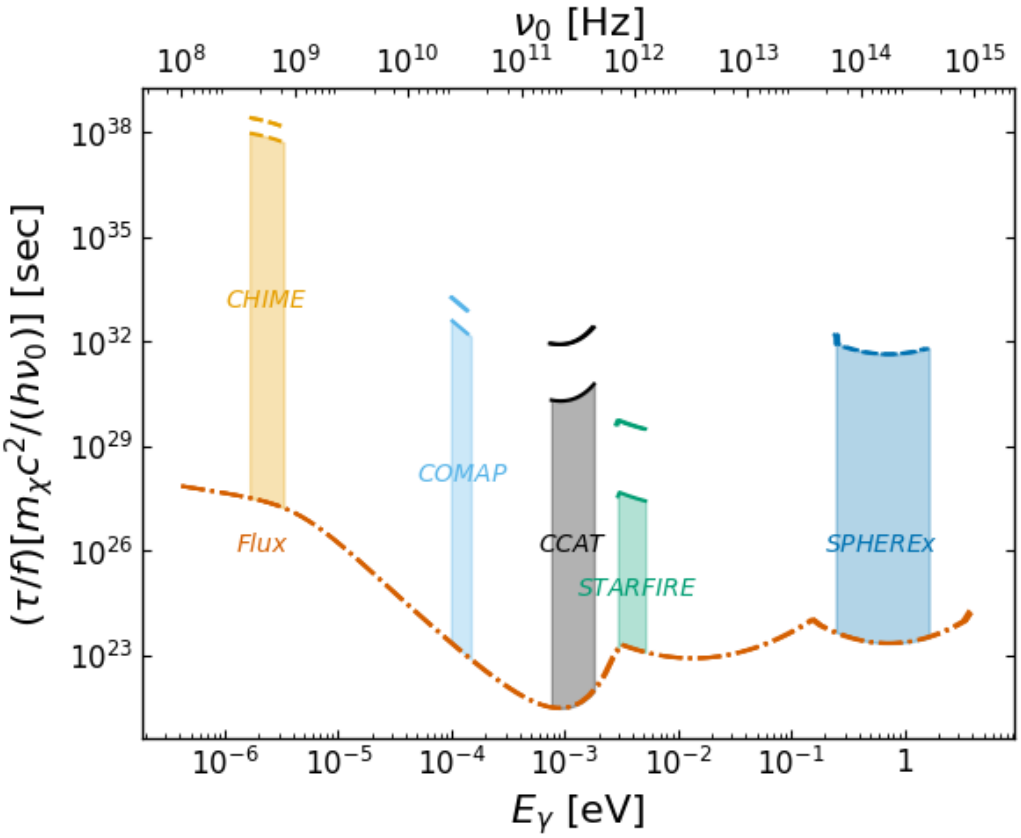

Figure 2.2: The largest lifetime τ for which a decay signal can be detected for the experiments shown. Here, f is the fraction of the dark matter composed of the particle that undergoes decays, m_χ the mass of the decaying particle, E_γ the decay-photon (rest-frame) energy, and ν_0 the decay-photon rest-frame frequency. The line labeled "Flux" is the largest lifetime consistent with the requirement that the intensity from particle decays does not exceed the extragalactic background light (EBL) intensity. The shaded regions are those not yet ruled out by current EBL measurements that will be accessible, given our estimates of the instrumental noise, with each experiment. The curves above each experiment (except for SPHEREx, which is limited by the EBL, not instrument noise) show the best sensitivity achievable with an experiment with similar specifications, but no instrumental noise, the sensitivity being limited in this case by the EBL. The experimental parameters assumed for each experiment are listed in Table 2.1.

Experiment	target	$[\nu_1, \nu_2]$ (GHz)	A (m^2)	$f_{\rm sky}$	R	$\theta_{\rm res}$	$T_{\rm eff}$ K
CCAT	[CII] (high z)	$[185, 440]$	28	3.9×10^{-4}	300	$1'$	148
CHIME	21-cm	$[400, 800] \times 10^{-3}$	8000	0.75	$\nu/(0.39\ \text{MHz})$	$20'$	100
COMAP	CO	$[26, 34]$	85	2.4×10^{-4}	800	$4'$	44
STARFIRE	[CII] (low z)	$[714, 1250]$	4.9	2.4×10^{-5}	250	1°	11
SPHEREx	Hα	$[60, 400] \times 10^3$	0.031	1	$41.4, 135^*$	$6.2''$	$0^\dagger$

Table 2.1: The experiment parameters used in Fig. 2.2. The survey duration in each case was chosen to be one year. *SPHEREx has two spectral resolutions, one for the low-frequency channels and another at high frequencies. †The noise in SPHEREx is limited by zodiacal light and turns out, for our purposes, to be negligible compared with that contributed by the EBL.

2.1.3 Discussion

As Fig. 2.2 indicates, IM experiments have the potential to dramatically increase our ability to seek radiatively-decaying dark matter in several photon energy windows, even with current-generation experiments. Our discussion above supposed that the cosmic mass distribution, against which the decay-line signal is to be cross-correlated, is obtained from a tracer survey of number density $\bar{n}_g$. However, the mass distribution is likely to be obtained, over the relevant cosmic volumes, by the intensity-mapping experiment itself. If so, then the relevant value of σ_k is that at which the contribution $P_{\rm n}(k)$ of the measurement noise (which may come from shot noise in the emitting sources and/or instrumental noise) to the power spectrum overtakes the tracer power spectrum $b^2 P(k)$; i.e., $P_{\rm n}(k_{\rm max}) = b^2 P(k_{\rm max})$. If the decay-line signal is sought by cross-correlation with a given galactic/IGM emission line, then our proposed search algorithm resembles that, proposed in Ref. [42], to seek a faint ^{13}CO line through cross-correlation with the brighter ^{12}CO line.

We neglected residual correlations in the EBL photons due to clustering of their sources, since the smoothing of the galaxy distribution along the line of sight, due to the broad galaxy spectrum, will suppress these. We believe that these residual correlations will be most generally be small, since the dynamic range of the frequency coverage for most IM mapping experiments is not too much greater than the width of the galaxy frequency spectrum. There may also be spectrum-mapping techniques, where emission from different frequencies of a characteristic galaxy spectrum are correlated, that can be used to mitigate the contamination from EBL clustering. The precise sensitivity is likely to be frequency dependent and weakened considerably if the decay-line frequencies coincides with that of a strong galactic emission line.

Let us now apply our results to the case of an axion that decays to two photons. To do so, we set $\zeta = 1/2$ and replace $\zeta \to 2\zeta$ due to there being two decay photons. For axions, there is a constraint $\tau \gtrsim 1.9 \times 10^{26}\,(m_a c^2/\mathrm{eV})^{-3}$ sec, from horizontal-branch stars, over the mass ranges considered here. While this is stronger than the sensitivities forecast here for $2E_\gamma = m_a c^2 \lesssim 0.1$ eV, it is considerably weaker than the sensitivity with SPHEREx we anticipate for $m_a c^2 \sim$ eV. The horizontal-branch constraint will not, however, necessarily apply more generally to other particles that undergo radiative decay. Scenarios where a heavier particle decays to a lighter state (e.g., as in exciting dark matter [23]) have appeared, motivated by a variety of problems, with a variety

of dark-matter masses, decay-photon energies, and detailed implementations; see, e.g., Refs. [43–49]. For example, suppose, following these references, that the dominant dark-matter component is a doublet (χ_1, χ_2) of mass m_χ that consists of two different mass states with a mass splitting $\Delta m \ll m_\chi$ which is then equal to the energy of the resulting decay photon. If, for example, we surmised $m_\chi c^2 \sim$ GeV and required that $\tau \gtrsim 10^{18}$ sec, then Fig. 2.2 indicates that the signal from $\sim 10^{-5}$ eV decay photons could be detected by CHIME even if the decay lifetime were as large as $\tau \sim 10^{24}$ sec. We leave the identification, exploration, and development of such models to future work.

We have assumed in our analysis that the particles undergo vacuum decay with a rate Γ. The entire discussion applies *mutatis mutandis*, however, for annihilations. In this case, Γ may have some slow redshift evolution which must be taken into account, and the annihilation-rate density fluctuation may be biased relative to the fluctuation in the dark-matter density. We leave further elaboration of these details, as well as investigation of detailed particle-physics models with such a signature to future work.

To close, we have suggested that lines from dark-matter decay and annihilation can be sought by cross-correlating a line signature in intensity-mapping experiments with some tracer of the mass distribution. We have sketched how such a cross-correlation can be performed and presented simple forecasts for the sensitivities that can, in principle, be achieved. Since intensity mapping is

only now getting underway, with long-term experimental capabilities yet to be specified in detail, our estimates are for hypothetical experiments limited only by the unavoidable noise presented by extragalactic background light. The potentially extraordinary improvements to the sensitivity to lines from dark-matter decay or annihilation we have shown motivates more careful feasibility studies and adds to the already strong scientific motivation, from more traditional astrophysics and cosmology [29,31], to pursue intensity mapping.

2.2 Direct millicharged DM and EDGES

The global 21-cm signal centered at 78 MHz was reported by the Experiment to Detect the Global Epoch of Reionization Signature (EDGES) [50] to be more than twice as deep than allowed by the standard cosmological model. This anomaly has been explained in terms of heat transfer between baryons and an interacting component of dark matter (DM) [51], as anticipated in Refs. [52,53]. This explanation requires, though, that such an interaction increase in strength at lower baryon-DM relative velocities to evade constraints from the cosmic microwave background (CMB) [54–57]. Currently, the only viable particle-physics models are those in which the interacting dark-matter component has a millicharge [58–62].

Millicharged dark matter is constrained by accelerator experiments [63],

big bang nucleosynthesis (BBN) [64, 65], stellar cooling [66], and SN1987A [67]. References [68–71] explored the implications of these constraints for EDGES, concluding that millicharged dark matter can explain EDGES if only a small component of the dark matter interacts with baryons. Refs. [57, 72] improved and updated the CMB constraints, carefully treated the strong-coupling regime at low DM fractions, and identified a minimum millicharged-DM fraction required to explain the EDGES signal. As a result, the current viable millicharged-dark-matter parameter space is limited to masses $0.1 \lesssim (m_\chi/\mathrm{MeV}) \lesssim 10$, charges $10^{-6} \lesssim (q_\chi/e) \lesssim 10^{-4}$, and fractions $(m_\chi/\mathrm{MeV})0.0115\% \lesssim f \lesssim 0.4\%$, with e the electron charge. Moreover, the millicharged particles must obtain their charge from the Standard Model photon, a scenario we call direct millicharged dark matter.

In this work, we first determine the millicharged-DM abundance by thermal freeze-out for a given mass and charge, and consider the implications for the parameter space of Ref. [72]. We moreover verify the chemical equilibrium assumption used in the recombination constraint to light millicharged-DM [65] and update it with current Planck 2018 data [73]. We find with these new results that if the millicharged-DM abundance is fixed by thermal processes, and no additional interactions (such as involving neutrinos) are present, then the millicharged-DM explanation of the EDGES signal is ruled out.

This work is organized as follows: In Sec. 2.2.1, we verify analytically and

numerically the validity of the assumption that the millicharged particles are in chemical equilibrium within the relevant parameter space. Then, in Sec. 2.2.2 we relate the fraction f of DM today to the mass and charge of the particle through freeze-out. Finally, in Sec. 2.2.3 we reproduce the calculations done in Ref. [65] with Planck 2018 data. We discuss and conclude these results in Sec. 3.1.4 and Sec. 3.1.3.

2.2.1 Thermalization

Consider a particle with mass m_χ and electromagnetic charge q_χ. For simplicity, we will take the particle to be a Dirac fermion, but discuss the scalar case in Appendix 2.2.6. We assume that the particle initially has zero occupation at a photon temperature higher than the particle mass. However, electromagnetic interactions with charged elementary particles increase the occupancy, which can be obtained from detailed balance of the pair-production cross section $\sigma^\alpha \equiv \sigma_{\chi\bar{\chi}\to\alpha\bar{\alpha}}$. At tree level, this cross section is given by

$$\frac{\sigma^\alpha}{(s+2m_\alpha^2)(s+2m_\chi^2)} = N_c^2 \frac{q_\alpha^2 q_\chi^2}{12\pi s^3}\sqrt{\frac{1-4(m_\alpha^2/s)}{1-4(m_\chi^2/s)}}, \tag{2.16}$$

where m_α and q_α are the mass and charge of another charged Dirac fermion α, s the center-of-mass energy squared, and N_c the number of colors (three for quarks, one for all others). We neglect photon annihilation as the cross

section is two orders higher in q_χ. The relevant quantity for the production of a population of millicharged particles however is the thermally-averaged cross section $\langle \sigma v \rangle = \sum_\alpha \langle \sigma^\alpha v \rangle$ [74],

$$\langle \sigma^\alpha v \rangle = \frac{1}{8 m_\chi^4 T K_2^2(m_\chi/T)} \int_{4\max(m_\chi, m_\alpha)}^{\infty} ds \sqrt{s}(s - 4m_\chi^2)\sigma^\alpha K_1(\sqrt{s}/T), \tag{2.17}$$

with T the photon temperature, and $K_i(x)$ the modified Bessel function of order i. We plot Eq. (2.17) in Fig. 2.3 after summing over all charged Dirac fermions in the Standard Model.

Millicharged particles are created by the annihilation of Dirac fermions and depleted by the inverse reaction. The abundance n_χ of millicharged particles is thus governed by the Boltzmann equation

$$\frac{dY_\chi}{dx} = -\lambda \left[Y_\chi^2 - (Y_\chi^{\rm eq})^2 \right], \tag{2.18}$$

written in terms of $Y_\chi = n_\chi/s$, and its equilibrium counterpart $Y_\chi^{\rm eq} = (n_\chi^{\rm eq})/s$. Here, $\lambda = s\langle \sigma v \rangle/(dx/dt)$ with $dx/dt = xs\sqrt{3\rho}/(M_{\rm pl}c)$ and $M_{\rm pl}$ is the reduced Planck mass. In addition, $\rho = (\pi^2/30) g_\rho(T) T^4$ is the energy density, $s = (2\pi^2/45)$ $g_s(T) T^3$ the entropy density, and $c = T(ds/dT) = (2\pi^2/15) g_c T^3$ the heat-capacity density [75]. We use the dimensionless inverse temperature $x = m_\chi/T$ to track

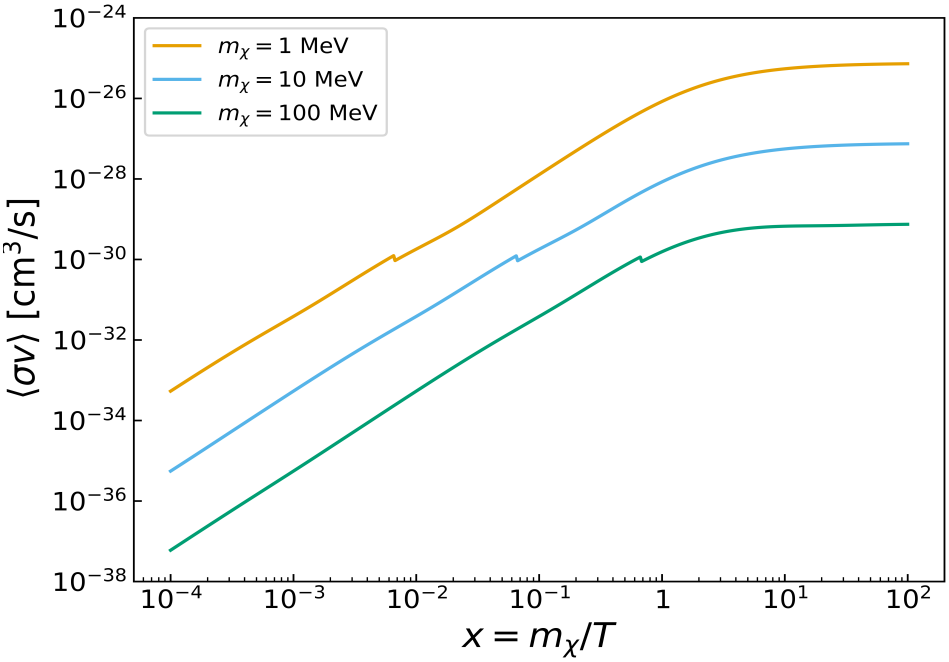

Figure 2.3: The sum of thermal cross sections between all charged Dirac fermions in the Standard Model and a millicharged particle with mass $m_\chi \in \{1\,\mathrm{MeV}, 10\,\mathrm{MeV}, 100\,\mathrm{MeV}\}$ and charge $q_\chi = 10^{-6}e$. For temperatures higher than the electron mass this expression follows the expected Coulombic scaling relation $x^2 \sim T^{-2}$, while exponentially cutting off at lower temperatures. There is a period, however, below the millicharge mass, where the thermal cross section is constant, though only when the millicharge mass is larger than the electron mass. The discrete jump is due to the change in particle content at the QCD crossover.

time, and the values from Ref. [76] for g_s, g_ρ, and g_c, where g_i is the relativistic degrees of freedom for the corresponding density i.

We now investigate if millicharged particles reach chemical equilibrium by determining when pair production is efficient. That is, if the number of millicharged particles dY_χ created in some fraction of a time dx/x is greater than

or equal to $Y_\chi^{\rm eq}$, the chemical equilibrium number, then this process is efficient and chemical equilibrium is reached instantaneously. Otherwise, chemical equilibrium is not reached. Since the last particle in the Standard Model to go nonrelativistic is the electron, the latest time (or lowest photon temperature) that chemical equilibrium could be obtained is at $T_{\rm min} \approx \max(m_\chi, m_e)$. At smaller temperatures, either the equilibrium abundance or the thermal cross section exponentially cuts off and production of millicharged particles is suppressed.

For millicharged particle masses $0.1 \lesssim (m_\chi/{\rm MeV}) \lesssim 100$, the minimum temperature is approximately the millicharged particle mass, $T_{\rm min} \approx m_\chi$, and the only relevant thermal cross section is with electrons, $\langle \sigma v \rangle \approx \langle \sigma^e v \rangle$. Therefore, as long as reheating, or any other particle-production mechanism, produces a thermal bath containing at least photons and electrons at temperature $T \geq T_{\rm min}$, it is possible to attain chemical equilibrium with this bath. Moreover, at such a temperature the thermal cross section simplifies as $\langle \sigma v \rangle \approx \langle \sigma^e v \rangle \approx q_\chi^2 e^2/(16\pi^2 T^2)$. We then evaluate and rearrange the aforementioned condition $(dY_\chi/d\log x)/Y_\chi^{\rm eq} \gtrsim 1$. Assuming we have not reached chemical equilibrium, $Y_\chi^2 \ll \left(Y_\chi^{\rm eq}\right)^2$, the temperature of equilibration has an upper bound,

$$T_{\rm eq} \lesssim 100\ {\rm GeV} \left(\frac{q_\chi}{10^{-6}e}\right)^2 \left(\frac{g_c(T_{\rm eq})}{g_s(T_{\rm eq})}\right) \left(\frac{10}{g_\rho(T_{\rm eq})}\right)^{\frac{1}{2}}. \tag{2.19}$$

Evaluating Eq. (2.19) at the minimum temperature $T_{\rm eq} = T_{\rm min}$ allows us to characterize equilibration only in terms of the millicharged particle's mass m_χ and charge q_χ,

$$\frac{q_\chi}{e} \gtrsim 10^{-8.5} \left(\frac{g_\rho(m_\chi)}{10}\right)^{\frac{1}{4}} \left(\frac{g_s(m_\chi)}{g_c(m_\chi)}\right)^{\frac{1}{2}} \left(\frac{m_\chi}{1\ \text{MeV}}\right)^{\frac{1}{2}}. \tag{2.20}$$

It follows that an initial millicharged abundance of zero will still reach chemical equilibrium within the allowed region of masses and charges. In order to verify the above conditions, we now perform a numerical check using Eq. (2.18), which involves all relevant Standard Model particles.

First, we check that the equilibration time specified by Eq. (2.19) is correct. Then, we check that the boundary between equilibration and nonequilibration in Eq. (2.20) is correct. Finally, we double check that in our region of parameter space chemical equilibrium is achieved. However, we only check that this equilibration occurs for a particle with the smallest permissible charge, as all other points have higher production efficiencies at $T_{\rm min}$. We demonstrate all three checks in Fig. 2.4 and find they all clear. Although it is not plotted, the same conclusion holds for millicharged particles that are complex scalars.

We conclude that in the relevant region, millicharged particles reach chemical equilibrium and undergo freeze-out.

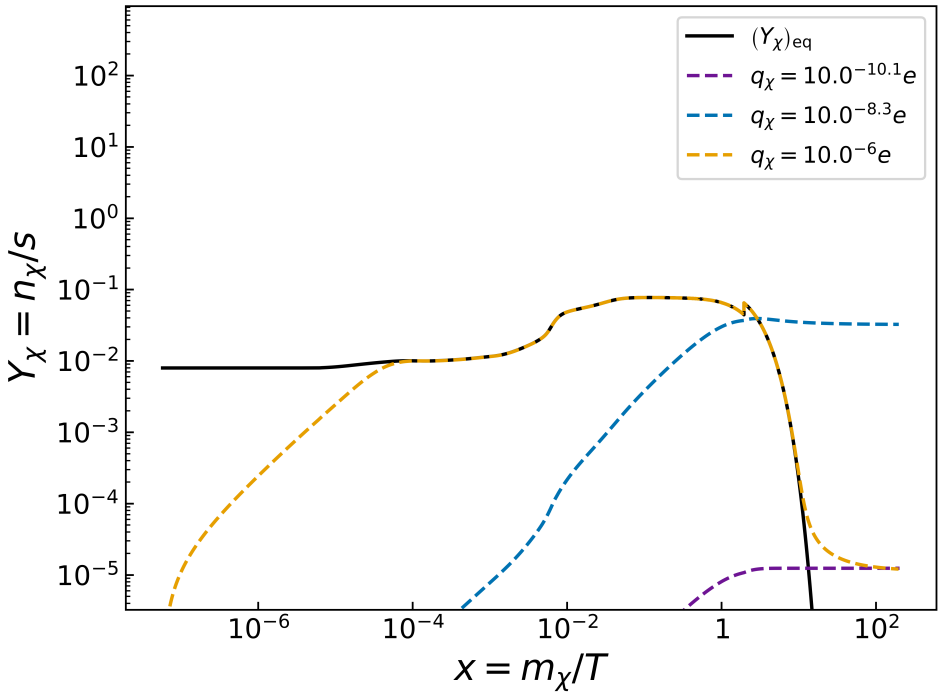

Figure 2.4: The abundance of a $m_\chi = 1$ MeV millicharged particle with charge $q_\chi \in \{10^{-6}e, 10^{-8.3}, 10^{-10.1}e\}$, evolved with Eq. (2.18). For the $q_\chi = 10^{-6}e$ case, the particle thermalizes at around 100 GeV. Otherwise, it never reaches chemical equilibrium, represented by $Y_\chi^{\rm eq}$. For the $q_\chi = 10^{-10.1}e$ scenario the abundance is set by freeze-*in*, and can achieve the same relic abundance as freeze-*out* with $q_\chi = 10^{-6}e$. However such charges are too small to produce the EDGES signal.

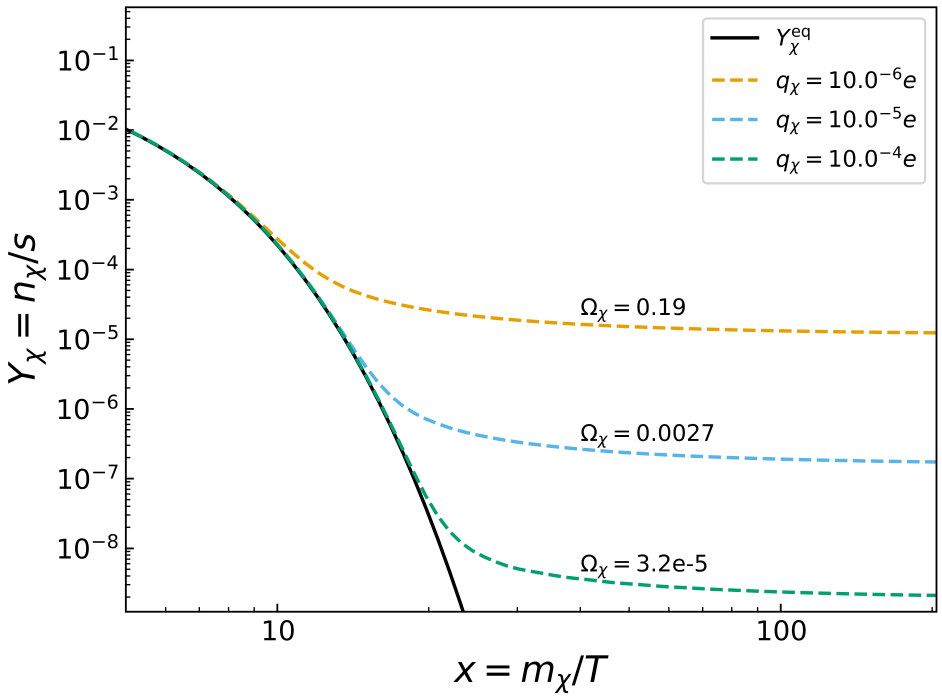

Figure 2.5: The numerically calculated freeze-out abundances Ω_χ of a Dirac fermion with mass $m_\chi = 1$ MeV and charge $q_\chi \in \{10^{-6}e, 10^{-5}e, 10^{-4}e\}$. Its equilibrium abundance $Y_\chi^{\rm eq}$ is plotted for reference.

2.2.2 Relic Abundance

If no depletion branches exist, the number of millicharged particles at freeze-out uniquely determines the amount today. More specifically, as the coupling with the thermal bath increases, the number of millicharged particles after freeze-out decreases; see Fig. 2.5, as the particles are in chemical equilibrium for a longer period of time. Neglecting the equilibrium term at freeze-out due to its exponential decrease, and treating the thermal cross section to be constant, we integrate Eq. (2.18) from the time x_f of freeze-out until today (which we take to be $x = \infty$). Note that the number of particles at the onset of freeze-out is much larger than the sum total today; see Fig. 2.4, and so its inverse can be neglected postintegration. The present photon temperature $T_{\rm cmb}$ is much smaller than the millicharged particle mass today, and so the population of millicharged particles is nonrelativistic. Therefore, we convert the relic number of millicharged particles $Y_\chi(x = \infty)$ into an energy density by multiplying both by its mass and the current entropy density. This multiplication leads us to express the energy density today in units of the critical energy density as

$$\Omega_\chi = \frac{\pi}{9}\frac{x_f}{\langle\sigma v\rangle}\left(\frac{g_\rho(m_\chi)}{10}\right)^{1/2}\frac{g_s(T_{\rm cmb})}{g_c(m_\chi)}\frac{T_{\rm cmb}^3}{M_{\rm pl}^3 H_0^2}, \tag{2.21}$$

with H_0 the Hubble constant today. This equation holds for both Dirac fermions and complex scalars. Reference [72] reported this abundance comprises a frac-

tion between $(m_\chi/\mathrm{MeV})\ 0.0115\% \lesssim f \lesssim 0.4\%$ of the entire DM content in order to both explain the EDGES 21-cm signal and evade the CMB constraints on the model.

In Fig. 2.6 we plot the millicharged fraction $f = \Omega_\chi/\Omega_c$, with Ω_c the cold dark matter energy density in units of the critical density. Overlaid on top are the aforementioned EDGES compatibility requirements. Since Eq. (2.21) is linear in the onset of freeze-out we do not worry about its exact timing and take $x_f = 10$.

Even after imposing the compatibility requirements, there remains a nonzero amount of parameter space that is still viable to explain the EDGES signal. In order to constrain this remaining amount, we calculate the effect of an additional particle on the effective number of relativistic degrees of freedom during recombination. To this end, we use our earlier result that this region is in chemical equilibrium. As a result, we can use the equations of Ref. [65] that detail such an effect for particles in chemical equilibrium, only updating their calculations using Planck 2018 parameters.

2.2.3 N_{eff} Bound

The addition of a new particle whose nongravitational interaction is solely electromagnetic and decoupling period is during or after neutrino decoupling T_{D} further enhances the photon temperature relative to the neutrino tem-

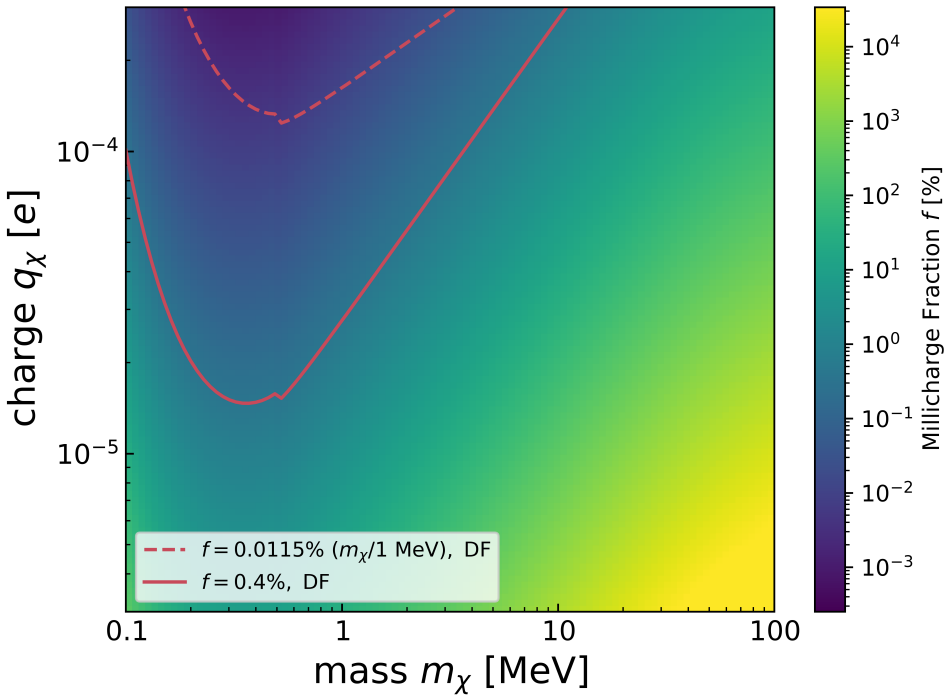

Figure 2.6: The DM fraction f of millicharged particles with mass m_χ and charge q_χ for Dirac fermions (DF). At fixed mass, the abundance decreases with increasing charge. At fixed charge the abundance minimizes at the electron mass due to a peak in the cross section with electrons and increases on either side otherwise. The sudden jump at the electron mass is due to an assumed discrete change in temperature after $e^{\pm}$ annihilation. The black region is unphysical due to DM overproduction.

perature T_ν due to entropy conservation. As a result, the measured effective number $N_{\rm eff}$ of relativistic degrees of freedom at recombination is shifted downward. In the context of n particles with masses and degrees of freedom $\{m_i, (g_\rho)_i\}, i \in \{1, ..., n\}$ and instantaneous neutrino decoupling, we use Eq. (10) of Ref. [65] to express $N_{\rm eff}$ as

$$N_{\rm eff} = N_\nu \left[1 + \frac{7}{22}\sum_{i=1}^{n} \frac{(g_\rho)_i}{2} F\left(\frac{m_i}{T_{\rm D}}\right)\right]^{-4/3},$$
$$F(x) \equiv \frac{30}{7\pi^4}\int_x^\infty dy \frac{(4y^2 - x^2)\sqrt{y^2 - x^2}}{e^y \pm 1}, \tag{2.22}$$

with N_ν the number of relativistic neutrinos at recombination, and the plus/minus for fermionic/bosonic statistics. Realistically, the additional particle not only imposes changes in $N_{\rm eff}$ but also in the helium mass fraction $Y_{\rm P}$, due to interactions during big bang nucleosynthesis (BBN). Although we do not calculate this mass fraction here, a proper treatment of constraining $N_{\rm eff}$ requires us to use the joint analysis on both $N_{\rm eff}$ and $Y_{\rm P}$ from Planck 2018, which allowed both variables to vary freely. In this analysis they inferred a conservative 95% confidence level constraint on the effective number of relativistic degrees of freedom $N_{\rm eff} = 2.97^{+0.58}_{-0.54}$ [73]. Since the effect of an additional particle is to lower $N_{\rm eff}$, we consider the Planck 2018 lower bound when inferring the CMB limit.

In order to derive constraints on our millicharged particle $[(g_\rho)_1 = 2 \text{ or } 4]$, we plot in Fig. 2.7 both this lower bound as well as Eq. (2.22), taking $T_{\rm D} = 2.3$

MeV and $N_\nu = 3.046$. In addition, we show via the same plot that it is possible to evade the Planck 2018 lower bound constraint if the Universe has two extra neutrinos at the time of recombination for a Dirac fermion (DF). Finally, for reference we show the Planck 2018 upper bound on $N_{\rm eff}$.

Since any value of $N_{\rm eff}$ below the Planck value is ruled out, we impose a lower bound on the millicharged particle mass at $m_\chi = 8.62$ MeV. We show this bound, along with the most recent upper bound on the charge of the millicharged particle from SLAC [63], in Fig. 2.8. Combined with our prior relic abundance constraints, and those of Ref. [72], the millicharged particle is completely ruled out.

2.2.4 Discussion

There are a few caveats when applying our bounds. First, if there exist at least two (but no more than three) extra neutrinos, it is possible to evade the aforementioned $N_{\rm eff}$ constraints for Dirac fermions.

One way to generate these extra degrees of freedom is by considering that the millicharged particle comes along with a kinetically mixed massless hidden photon. Reference [69] already claimed to rule out this model; however this was only for large dark couplings g' between the hidden photon and millicharged particle. This constraint [66] arises because large dark couplings overshoot the value of $N_{\rm eff}$ during BBN. If the dark coupling was identically

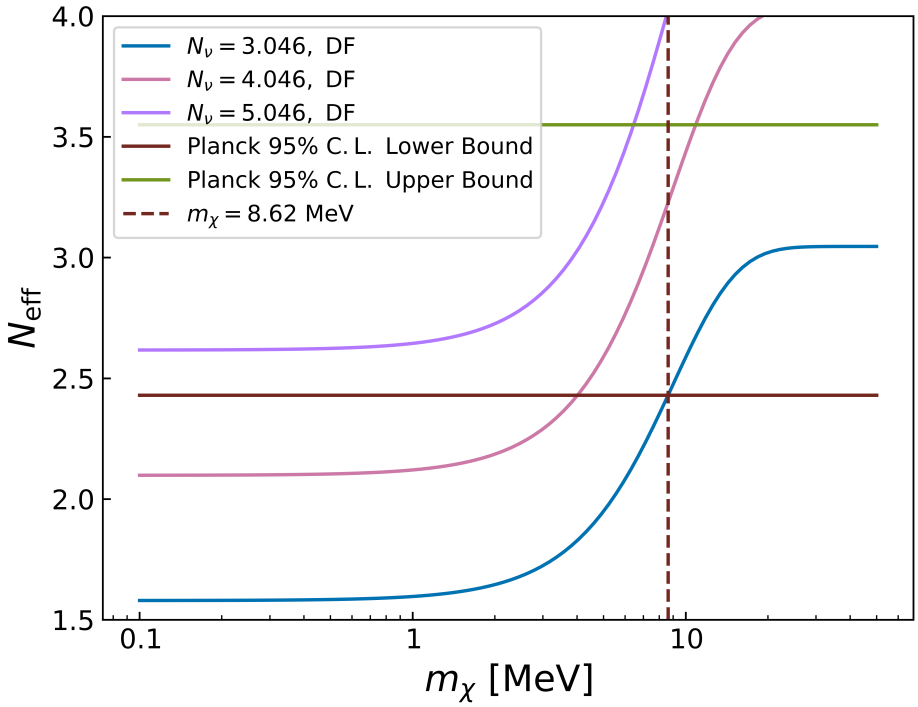

Figure 2.7: The effective number $N_{\rm eff}$ of relativistic degrees of freedom as a function of the millicharged particle mass m_χ, assuming N_ν relativistic neutrinos at recombination for a Dirac fermion (DF). The solid reddish brown line is the 95% confidence level lower bound from Planck 2018. The dashed counterpart is the resulting lower bound on the millicharged particle mass for $N_\nu = 3.046$.

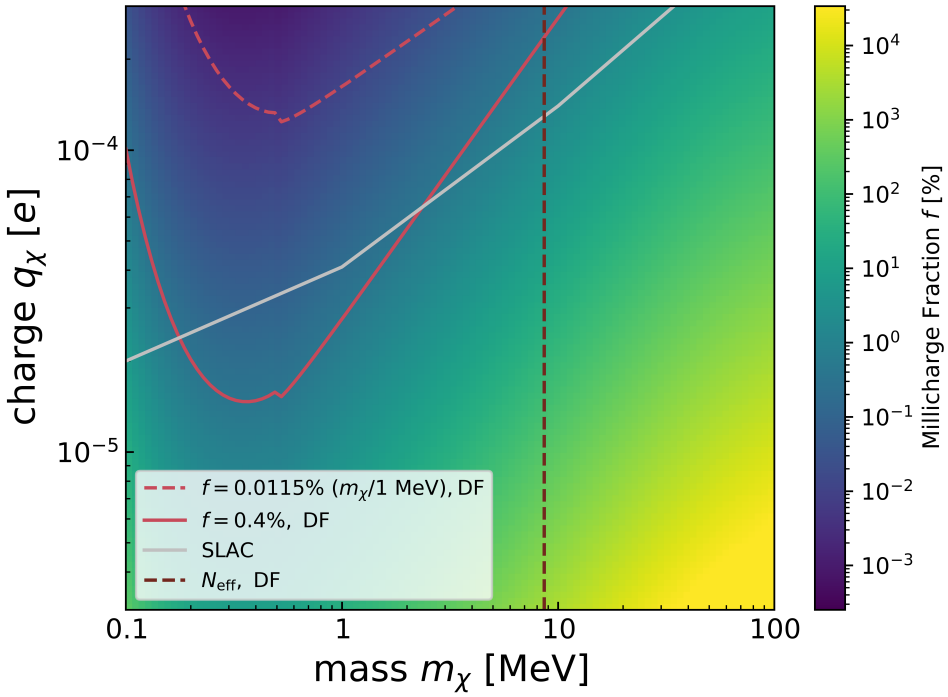

Figure 2.8: The dark matter fraction f of millicharged particles with mass m_χ and charge q_χ for Dirac fermions (DF). The region between the dashed and solid red line is the range of relic abundances that are compatible with CMB and EDGES constraints. The region above the solid grey line is ruled out due to SLAC measurements. Finally, the region to the left of the reddish brown vertical line is ruled out due to $N_{\rm eff}$ constraints. The viable regions between the SLAC and relic abundance regions have nonzero overlap, but this overlapped region does not intersect with the region permitted by $N_{\rm eff}$.

zero, however, only the millicharged particle would be thermalized and the value of $N_{\rm eff}$ would be undershot, see Fig. 2.7. Thus, we ask if the increase of $N_{\rm eff}$ by the hidden photon can be balanced by a corresponding decrease from the millicharged particle.

However, it is expected that the kinematic mixing parameter $\chi = q_\chi/g'$ is less than 10^{-2}. In addition, only charges $q_\chi \gtrsim 10^{-6}e$ are viable to explain EDGES. Taken together, this leads us to conclude that $g' \gtrsim 10^{-4}e$. For such values, Sec. 4.2 of Ref. [66] shows that their bounds on $N_{\rm eff}$, which exclude the parameter space of interest, still apply.

Secondly, atomic dark matter, a scenario where a residual free dark electron fraction follows a dark recombination, may still be viable [77–79]. The remaining ionized DM could provide the fractional millicharged DM component that is required to explain the EDGES signal[2].

Moreover, an additional interaction could exist between neutrinos and the millicharged particle that is efficient during millicharged particle annihilation. In this case, the heat from annihilation would not only go to photons, but also to neutrinos, producing no change in $N_{\rm eff}$. However, such a case would induce a coupling between charged particles and neutrinos through loop effects. As a result, it faces strong constraints from bounds on the electric charge of the neutrino [80].

[2]Curiously, the ionized fraction of the baryonic gas around cosmic dawn is of order 10^{-4}, similar to the values required to explain EDGES via millicharged DM (see Ref. [22]).

It could also be the case that millicharged particles receive an electronic charge not only through kinetic mixing, but also through the Standard Model photon by some higher-energy physics. If the Standard Model photon charge is larger than the charge generated through kinetic mixing, so that $q_\chi \neq g'\chi$, then the dark coupling g' evades the $q_\chi \gtrsim 10^{-4}e$ requirement. Thus, the $N_{\rm eff}$ change due to millicharged particles could be offset by this hidden photon.

At larger $N_{\rm eff}$ confidence intervals than 95%, the corresponding $N_{\rm eff}$ bound may decrease significantly from the current value of $m_\chi = 8.62\ \mathrm{MeV}$. As a result, there would remain an unconstrained region of parameter space. In this case, it is possible to use indirect detection of millicharged particles via keV and MeV gamma-ray observations to ipossibly rule out this remaining region [81–83]. However, such bounds would be dependent on the final states of the annihilation.

Finally, millicharged particles could have their abundance set not thermally, but through reheating that occurs at a temperature above BBN but below the millicharged mass [84–86]. As a result, not only are annihilations severely suppressed so that any change in $N_{\rm eff}$ is small, but also the relic abundance formula we wrote down does not hold.

2.2.5 Conclusion

We have considered the prospects of a millicharged particle directly charged under the Standard Model photon to explain the anomalous EDGES 21-cm signal. Specifically, we had three tasks in mind. First, we wished to verify that millicharged particles that have their abundances set thermally reach chemical equilibrium regardless of initial conditions. If so, we then wanted to calculate the millicharged-DM abundance set by thermal freeze-out for a given mass and charge in order to consider its implications for the parameter space of Ref. [72]. Lastly, we sought to improve on the Planck $N_{\rm eff}$ constraint from Ref. [65] with Planck 2018 data.

We found that regardless of the initial abundance, millicharged particles reach chemical equilibrium and then undergo freeze-out. This evolution occurs as long as there exists a thermal photon and electron bath at a temperature higher than the millicharged particle mass. Using the Boltzmann equation, we then calculated both numerically and analytically the millicharged relic abundance and found a reduced, but still viable, portion of parameter space remaining to explain the EDGES signal.

In order to cut down on this space further, we considered the effect of entropy dumping on the effective number $N_{\rm eff}$ of relativistic degrees of freedom. We found that this number decreases due to the increase in photon temperature after the millicharged particle decouples postneutrino decoupling. This de-

crease was severe enough such that the remaining amount of parameter space was completely ruled out.

Barring the caveats mentioned in the Sec. 3.1.3, we therefore conclude that a millicharged particle cannot produce the 21-cm signal observed at EDGES.

2.2.6 Complex Scalars

In this additional section, we consider the millicharged particle creating the anomalous EDGES 21-cm signal to be a complex scalar (CS). Its pair-production cross section $\sigma^{\alpha}_{\rm CS} \equiv \sigma^{\rm CS}_{\chi\bar{\chi}\to\alpha\bar{\alpha}}$ with a Dirac fermion α is then

$$\frac{\sigma^{\alpha}_{\rm CS}}{(s+2m_{\alpha}^2)(s-4m_{\chi}^2)} = N_c^2 \frac{q_{\alpha}^2 q_{\chi}^2}{48\pi s^3}\sqrt{\frac{1-4(m_{\alpha}^2/s)}{1-4(m_{\chi}^2/s)}}. \tag{2.23}$$

As we remarked in Sec. 2.2.1, the complex scalar also reaches thermalization with the thermal bath of Standard Model particles. Thus, we can use Eq. (2.21) in conjunction with Eq. (2.23) to calculate the freeze-out relic abundance of these particles today, plotted in Fig. 2.9. We find that the largest allowable relic abundance by the CMB, $f \simeq 0.4$ [57], corresponds to masses m_{χ} and charges q_{χ} already ruled out by SLAC. Therefore, we conclude that a complex scalar millicharged particle cannot create the anomalous EDGES 21-cm signal.

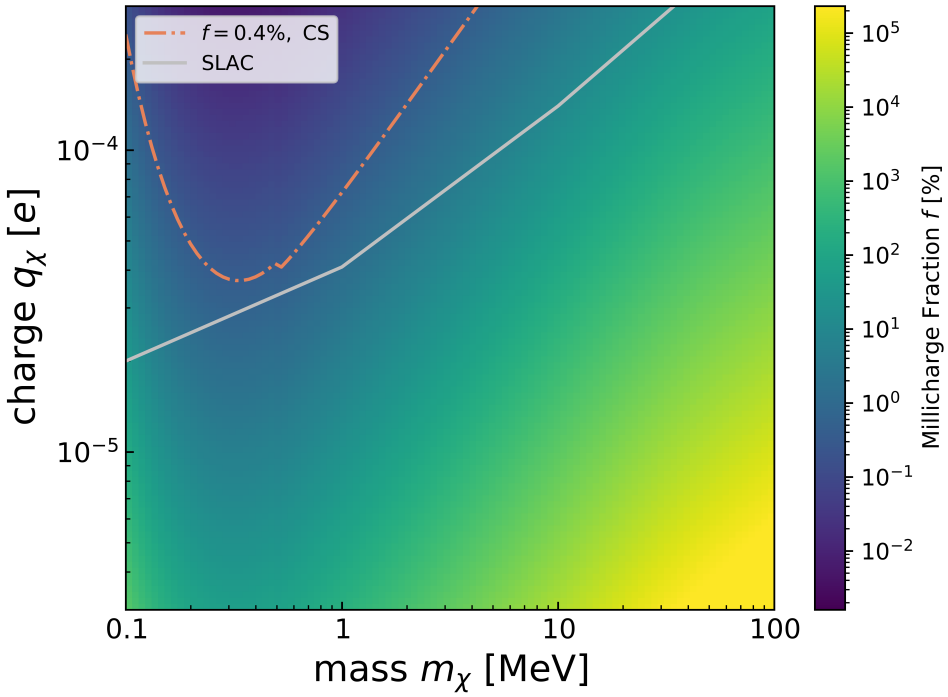

Figure 2.9: The dark-matter fraction f of millicharged particles with mass m_χ and charge q_χ for complex scalars (CS).

Chapter 3

Active Galactic Nuclei (AGN)

3.1 AGN variability in the age of Rubin

The intensity of most active galactic nuclei (AGN) is observed to vary on timescales from minutes to decades and in frequency bands ranging from radio to gamma ray [87–90]. X/Gamma-ray variability is thought to arise from the innermost part of the AGN [91–93], while optical/UV variability from the outer accretion disk as the result of instabilities or X-ray reprocessing [94–96]. However, there can be additional contributions in the optical/UV band from the broad-line region and dust torus either due to intrinsic variability [97,98] or X-ray reprocessing [99, 100]. In addition, radio variability can also be intrinsic, and if so comes from the inner core of the AGN [101]. The variability from higher frequency light can occur on timescales between minutes and

years [102–104], while lower frequency light tends to occur on the scales of months to years [105]. At the higher end of the variability timescale are changing-look AGN, whose intensity can fluctuate over time periods of decades [106–108]. Despite their prevalence in AGN physics, the relationship between AGN type and variability timescale, or even the causes of variability have still not been fully characterized. With the advent of the Vera C. Rubin Observatory (Rubin), the flux measurements of over 10 million AGN will be made over the course of 10 years, with first light slated for the end of 2022 [109]. The huge number of sources, coupled with a vast increase in the number of regular high frequency observation epochs, Rubin will allow for unparalleled precision in variability analyses.

The rich and ubiquitous property of AGN variability has been exploited not only to classify [110, 111] but also to identify AGN [112–116]. However, attempts to connect variability measurements to physical mechanisms have lacked sufficient data, leaving such connections mostly tenuous [117, 118]. More success has been found in modelling the stochastic nature of these processes [119]. Such modelling has seen that most AGN exhibit variability that is well described by a damped random walk (DRW), as shown by analyses involving structure functions, autocorrelation functions, and power spectra [120–124], although, some examples of non-DRW AGN have been found [125–127]. The DRW model has been used to extract the variability timescale through the

use of the structure function [128]. In addition, numerical investigations have been used to model AGN variability across multiple timescales [129, 130]. Recently,the variabilities of 67 AGN were characterized to follow a power law with an index measured to one part in ten [131].

In this work, we explore the prospects for studying AGN variability with Rubin. Previous analyses of AGN variability have been limited due to small AGN sample size or infrequent visit times, both of which will be remedied with the dawn of Rubin. For a single AGN, we forecast that Rubin will measure both the variability amplitude and timescale up to $10^3\sigma$. With such precise measurements, we then model a power law relationship between an AGN's bolometric luminosity and its variability with index β_b in Rubin frequency band b. We find that this index will be measured possibly to one part in a million. Therefore, these results suggest that the next decade of observations will lead to a wealth of knowledge in AGN variability.

This work is structured as follows. In Sec. 4.2.1 we present the formalism for measuring the variability amplitude and timescale in the context of a single AGN and a population of AGN. We then follow up this formalism in Sec. 4.2.3 and present estimators in order to quantify variability. Moreover, using these estimators we make an expected information forecast to Rubin's sensitivity in measuring both variability parameters for a single AGN, along with their covariance. Then, we present the analogous calculation for the theoretical best

sensitivity to measuring a power law relationship between AGN bolometric luminosity and variability. We discuss these results and conclude in Secs. 3.1.3 and 3.1.4, respectively.

3.1.1 Formalism

Assume the intensities from a population of AGN have been measured over time. We pursue a description of the variability of these intensities through the use of the two-point correlation of their intensities. In this vein, we first present the autocorrelation function for a single AGN. Then, for a population of AGN, we extend the presentation of a single AGN and model a relationship between the bolometric luminosity of an AGN with both its variability parameters through a power law.

3.1.1.1 Single AGN

Let $I_b^j(t)$ be the observed intensity of AGN j in frequency band b and $\bar{I}_b^j$ be its time average . With these two quantities, define $\delta_b^j(t) = I_b^j(t)/\bar{I}_b^j - 1$ to be the observed variability of AGN j in frequency band b. We describe the statistical properties of the observed variability of AGN j in frequency band b in terms of the observed two-point variability correlation function $\langle \delta_b^j(t_1)\delta_b^j(t_2)\rangle$. If the underlying mechanism creating the observed signals is independent of time for the duration of observation, then the two-point correlation function is

homogeneous in time (i.e. stationary) and thus only a function of the time lag $t = |t_2 - t_1|$, $\langle \delta_b^j(t_1)\delta_b^j(t_2)\rangle = \langle \delta_b^j(t'+t)\delta_b^j(t')\rangle$.

With this assumption, we model the observed two-point variability correlation function for a single AGN as

$$\left\langle \delta_b^j(t'+t)\delta_b^j(t')\right\rangle = \xi_{bb}^j(t) + \Delta t_b \sigma_{jb}^2 \delta(t), \tag{3.1}$$

$$\xi_{bb}^j(t) \equiv A_{jb}^2 e^{-|t|/\bar{t}_{jb}^o}, \tag{3.2}$$

with $\xi_{bb}^j(t)$ the two-point variability correlation function taking the form of a damped random walk [120, 122, 132], A_{jb} the variability amplitude and $\bar{t}_{jb}^o$ the variability timescale of AGN j in the observer's frame, Δt_b the temporal resolution of the experiment, and $\delta(t)$ the Dirac delta function. Moreover, σ_{jb}^2 is the variance of a white noise process representing photometric error in an AGN's intensity measurements. We assume this noise does not correlate with any AGN's variability. Note that the observed two-point variability correlation function contains instrumental noise, while the two-point variability correlation function does not. Due to either AGN physics or instrument properties, all quantities mentioned depend on the observing frequency band b. Furthermore, due to cosmic redshifting, the variability timescale $\bar{t}_{jb}^r$ of an AGN located at redshift z as measured in its rest frame is related to the observer frame analog through the expression $\bar{t}_{jb}^o = (1+z)\bar{t}_{jb}^r$.

With this expression of the observed correlation function, its Fourier transform is

$$\frac{1}{2\pi}\int d\omega' \left\langle \tilde{\delta}_b^j(\omega)\tilde{\delta}_b^{j*}(\omega')\right\rangle = P_{bb}^j(\omega) + \Delta t_b \sigma_{jb}^2, \tag{3.3}$$

$$P_{bb}^j(\omega) \equiv \frac{2A_{jb}^2 \bar{t}_{jb}}{1+(\omega \bar{t}_{jb})^2}, \tag{3.4}$$

with $P_{bb}^j(\omega)$ the variability power spectrum for AGN j in frequency band b. Here and in what follows, we use Fourier convention $f(t) = (2\pi)^{-1}\int d\omega e^{-i\omega t}\tilde{f}(k)$ and $\tilde{f}(\omega) = \int dt e^{i\omega t} f(t)$. We plot an example variability power spectrum for a single AGN in Fig. 3.1.

3.1.1.2 AGN Population

In addition to modelling each AGN individually, we also model the two-point variability correlation function of a single AGN from a set of population parameters. Define $\xi_{bb}(t, z, L)$ to be the variability correlation function for an AGN located at redshift z with bolometric luminosity L,

$$\xi_{bb}(t, z, L) = A_b^2(L)\exp\left[-|t|/\bar{t}_b^o(z, L)\right]. \tag{3.5}$$

In writing this expression, we implicitly assume that AGN variability is only characterized by two parameters: its redshift and bolometric luminosity. In

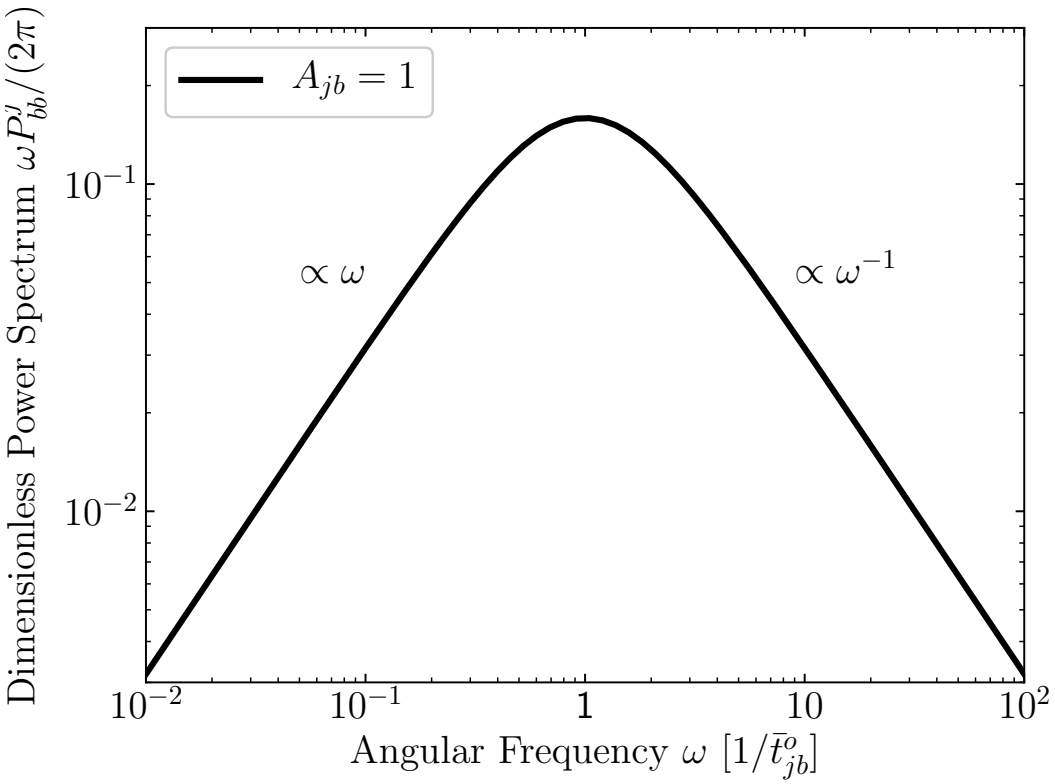

Figure 3.1: The dimensionless variability power spectrum $\omega P^{j}_{bb}/(2\pi)$ for an AGN with variability amplitude $A_{jb} = 1$ using Eq. (3.4). The peak of this power spectrum occurs at $\omega = \bar{t}^{-1}_{jb}$, with amplitude $A^{2}_{jb}/(2\pi)$. For frequencies smaller than this peak it rises as ω, and for frequencies larger it falls as ω^{-1}. Since we plot the angular frequency in units of $\bar{t}^{-1}_{jb}$, its value is arbitrary.

addition to this correlation function, we define the power spectrum $P_{bb}(\omega, z, L)$ analogously.

Typically, AGN with higher bolometric luminosities are more massive. Since variability on timescales smaller than the light crossing time of the emitted object is suppressed, the larger an AGN, the larger its expected variability timescale. Thus, we model the relationship between AGN variability and bolometric luminosity as

$$A_b(L) = A_b, \tag{3.6}$$

$$\bar{t}_b^o(z, L) = \bar{t}_b^r(1+z)\left(\frac{L}{L_b}\right)^{\beta_b}, \tag{3.7}$$

with $L_b = L_{\rm bol}(m_{\rm lim}^b, z_{\rm min})$ a normalization constant chosen to be the dimmest expected observed AGN. In this expression, we assumed all AGN to have the same variability amplitude for simplicity. Thus, a population of AGN is described by the three parameters $A_b, \bar{t}_b^r$, and β_b. Recently, 67 AGN were found to follow a similar variability timescale relation, with the mass of the AGN as the the only dependent parameter, and the index $\beta \sim 0.23$ [131].

Let $dN_{\rm AGN}/dzdL$ be the redshift and bolometric luminosity distribution of this population of AGN. Then these AGN are distributed throughout the Uni-

verse according to

$$\frac{dN_{\rm AGN}(z,L)}{dzdL} = \frac{dV(z)}{dz}\frac{dn(z,L)}{dL}, \tag{3.8}$$

with $dn(z,L)/dL$ the AGN luminosity function, $dV(z)/dz = 4\pi f_{\rm sky} r(z)^2 dr(z)/dz$ the comoving volume observed over a fraction $f_{\rm sky}$ of the sky, $r(z) = \int_0^z |dr/dz|dz$ the comoving radial distance to a redshift z, $dr/dz = -c/(1+z)H(z)$ its redshift derivative, c the speed of light, and $H^2(z) = H_0^2\left[\Omega_m(1+z)^3 + (1-\Omega_m)\right]^{-1/2}$ the Hubble parameter. We use Planck 2018 ΛCDM parameters $H_0 = 2.18\times10^{-18}{\rm s}^{-1}$ and $\Omega_m = 0.315$ [73], along with the "Full AGN" luminosity function in Table 3 from [133].

Given a cosmological distribution of AGN, only those that appear bright enough will be observed. More specifically, given a limiting apparent magnitude $m_b^{\rm lim}$ in a band b, the distribution of observed AGN in that band is

$$\frac{dN^b_{\rm AGN}}{dzdm_b} = \Theta(m_b^{\rm lim} - m_b)\frac{dL_{\rm bol}}{dm_b}\frac{dN_{\rm AGN}[z, L_{\rm bol}(z,m_b)]}{dzdL_{\rm bol}}, \tag{3.9}$$

with $\Theta(x)$ the Heaviside theta function, $L_{\rm bol}(z,m_b) = K_b(m_b)4\pi d_L(z)^2\delta\nu_b F_{\rm AB}10^{-(2/5)m_b}$ the bolometric luminosity for an AGN with apparent magnitude m_b in frequency band b located at redshift z, and $dL_{\rm bol}/dm_b = -(2/5)\log(10)L_{\rm bol}(m_b,z)$ its apparent magnitude derivative. Moreover, $K_b(m_b)$ is the bolometric correction function to convert from the emitted luminosity in band b to bolometric

luminosity of the source, $d_L(z) = (1+z)r(z)$ the luminosity distance, $\delta\nu_b$ the frequency bandwidth of band b, and $F_{\rm AB} = 3.631 \times 10^{-23}\ \mathrm{WHz^{-1}m^{-2}}$. Note that in this expression for the bolometric intensity, we assume the observed intensity is roughly constant across the entire bandwidth, and that the redshifted frequency does not alter the intensity in each band significantly. In general, the bolometric correction within the optical range is a function of the bolometric luminosity of the source. However, across all bolometric luminosities the correction changes only up to 20%, and inversion of this expression can only be done numerically. Thus, for simplicity, we adopt that $K_b(m_b) = 10$ for all magnitudes and bands [133]. We plot the observed AGN distribution, without the theta function, in Fig. 3.2.

3.1.2 Forecasts

One may measure both the variability amplitude and timescale of an AGN from measuring only its variability correlation function at different lag times. However, the relation between the observed correlation function at any lag time and the true underlying stochastic process becomes increasingly inaccurate for variability timescales smaller than the cadence and larger than the observational period. On the other hand, the observed power spectrum is accurate for all Fourier modes well within these limits.

In this section, we use the expected information from the power spectrum

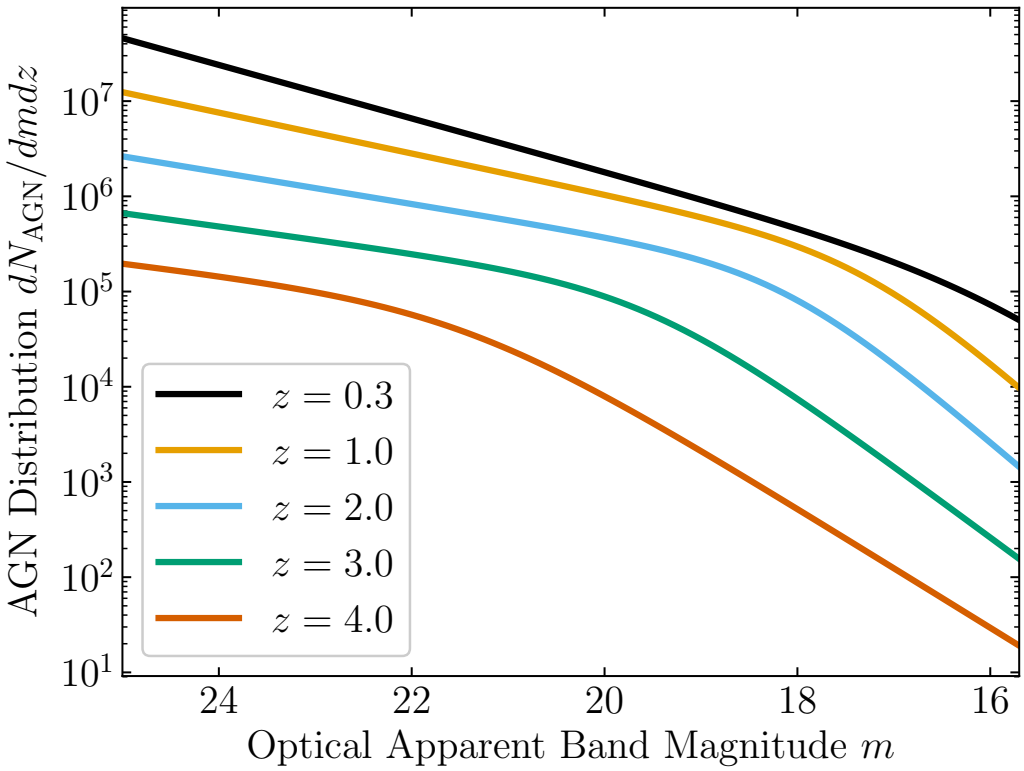

Figure 3.2: The distribution $dN^b_{\mathrm{AGN}}/dm_b dz$ of AGN as a function of the apparent magnitude in a band b at redshifts $z \in \{0.3, 1.0, 2.0, 3.0, 4.0\}$ as given by Eq. (3.9). In order to show the full range of this distribution, we do not include the theta function factor.

estimators for a single AGN and a population of AGN to forecast Rubin's ability to measure various variability parameters. The analysis, discussed below, leads to the signal-to-noise results for the variability amplitude in Fig. 3.4. Furthermore, we show the covariance between the variability amplitude and timescale in Fig. 3.5 and the variability index and timescale in Fig. 3.6. All figures are done for a representative sample of Rubin's frequency bands.

We model the individual band errors as a sum of Poissonian shot noise from source, Poissonian shot noise from the sky, Gaussian instrumental noise, and systematic error. More specifically, for Rubin we use the fit given by 0912.0201 and propagate the error from apparent magnitude to variability,

$$\sigma_{jb}^2 = \frac{2}{5}\log(10)\left[\sigma_{\rm sys}^2 + \left(\sigma_{jb}^{\rm rand}\right)^2\right], \tag{3.10}$$

$$\left(\sigma_{jb}^{\rm rand}\right)^2 = (0.04-\gamma_b)x_{jb} + \gamma_b x_{jb}^2, \tag{3.11}$$

with $x_{jb} = 10.0^{(2/5)(m_{jb}-m_5^b)}$, m_{jb} the apparent magnitude of AGN j, and m_5^b the 5σ depth for point sources, both defined in frequency band b. The fitted parameter γ_b depends on sky brightness, readout noise, and other factors. We show the relevant experimental parameters for each band in Table. 3.1 and plot the photometric error in Fig. 3.3. For all bands we take the limiting apparent magnitude to be the 5σ point source depth, $m_{\rm lim}^b = m_5^b$. Moreover, define $n_{\rm vis}^b = T/\Delta t_b + 1$ to be the number of visits to AGN j in frequency band b and

$n_{\rm vis} = \sum_b n^b_{\rm vis}$ the total number of visits. Note that we assume that all AGN are visited an equal number of times across all frequency bands.

b	u	g	r	i	z	y
γ_b	0.038	0.039	0.039	0.039	0.039	0.039
m^b_5	23.78	24.81	24.35	23.92	23.34	22.45
$n^b_{\rm vis}$	70	100	230	230	200	200
Δt_b [days]	52.90	36.87	15.94	15.94	18.34	18.34

Table 3.1: The experimental parameters for Rubin.

3.1.2.1 Single AGN

For notational simplicity, we assume all AGN are observed for the same duration $T_j = T$ and sampled at the same times. However, we allow for different sampling between different frequency bands b. Under the null hypothesis, AGN undergo no variability and thus the noise for the power spectrum estimator of AGN j in band b is

$$\left[\sigma^{jb}_{\rm null}(\omega)\right]^2 = 2\left[\Delta t_b \sigma^2_{jb}\right]^2. \tag{3.12}$$

We also combine the information of all bands through the use of bolometric corrections. First we calculate the bolometric correlation function as given by a particular band. Since the bolometric intensity is approximately linear in the band intensity, their fractional errors are the same. Then, we inverse-variance weigh each band to obtain an estimate of the actual bolometric correlation func-

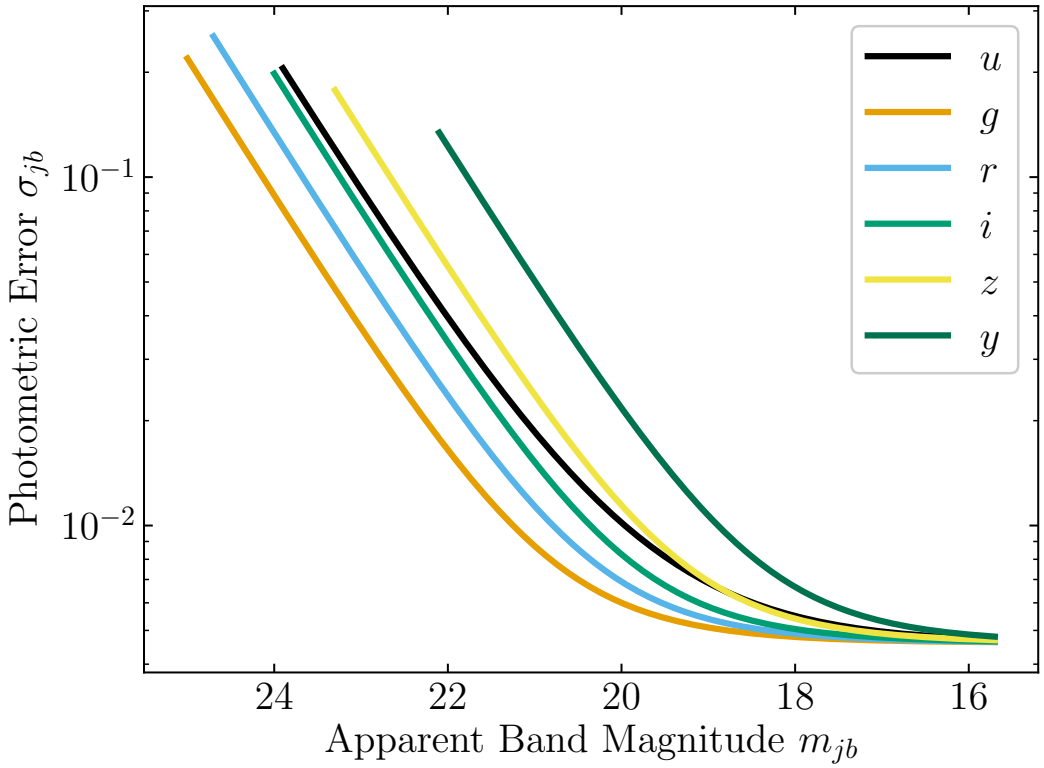

Figure 3.3: The Rubin photometric error for an AGN's variability in each Rubin frequency band $b \in \{u, g, r, i, z, y\}$, as well as for the bolometric variability error, as given by Eq.(3.10) and Eq. (3.13). The magnitudes plotted ranges from the 5σ apparent magnitude limit in the corresponding band, shown in Table. 3.1, to the theoretical value for the brightest AGN that will be observed $m^b_{\rm cut} = 15.7$.

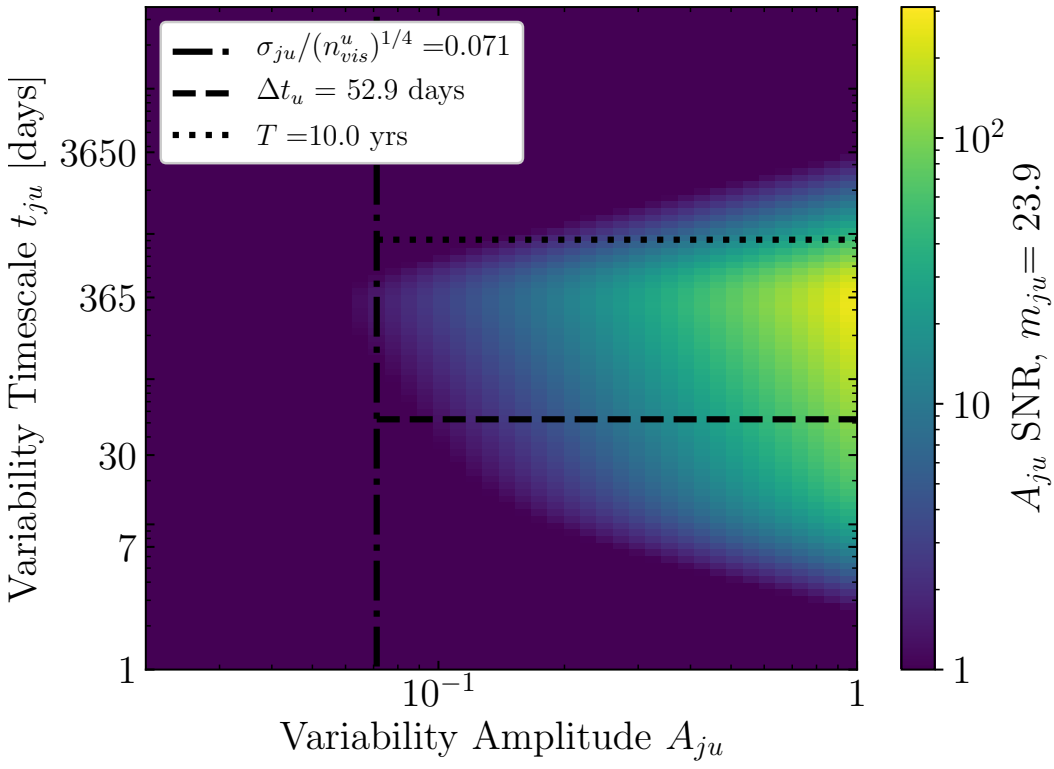
$\sigma_{ju}/(n^u_{vis})^{1/4}$ =0.071
Δt_u = 52.9 days
T =10.0 yrs
Variability Timescale t_{ju} [days]
3650
365
30
7
1
10^{-1}
1
Variability Amplitude A_{ju}
10^2
10
1
A_{ju} SNR, m_{ju}= 23.9

(a)

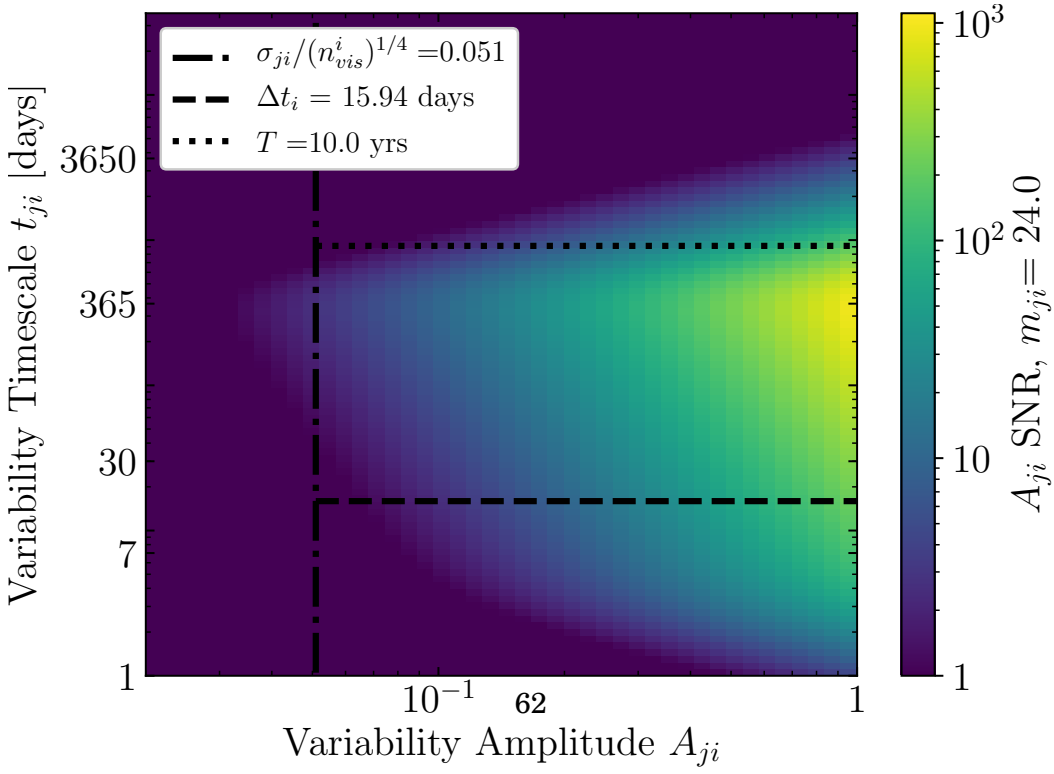
$\sigma_{ji}/(n^i_{vis})^{1/4}$ =0.051
Δt_i = 15.94 days
T =10.0 yrs
Variability Timescale t_{ji} [days]
3650
365
30
7
1
10^{-1}
1
Variability Amplitude A_{ji}
10^3
10^2
10
1
A_{ji} SNR, m_{ji}= 24.0

(b)

tion. Therefore, the error $\sigma_{\rm null}^{j\rm bol}$ in measuring this correlation function is

$$\left[\sigma_{\rm null}^{j\rm bol}(\omega)\right]^{-2} = \sum_b \left[\sigma_{\rm null}^{jb}(\omega)\right]^{-2}. \tag{3.13}$$

Since the bolometric band is a combination of measurements done in different bands with different temporal resolutions - the bolometric band has unequal, but periodic, temporal spacing in measurements. Moreover, not every temporal spacing has an equal number of measurements. Rather than model this spacing, we take an equal-time temporal resolution $\Delta t_{\rm bol} = T/(n_{\rm vis} - 1)$, with the condition that null-hypothesis forecasts using this resolution are upper bounds.

Moreover, we note that given the bolometric correlation function, we can invert the bolometric corrections in order to translate the bolometric error into the error in any particular band b. Thus, through inverse variance weighing, the bolometric band represents the optimal sensitivity for any particular band.

With the null-hypothesis power spectrum noise in hand, we use the expected information matrix to infer the covariance matrix for our AGN parameters. We plot the signal-to-noise of measurements for the variability amplitude for a single AGN under the null hypothesis in Fig. 3.4.

To calculate the covariance between the variability amplitude A_{jb} timescale $\bar{t}_{jb}$ once a signal is detected, we must include the correlations from the signal.

Therefore, the noise for the power spectrum $P^j_{bb}(\omega)$ estimator is now

$$\left[\sigma^{jb}_P(\omega)\right]^2 = 2\left[P^j_{bb}(\omega) + \Delta t_b \sigma^2_{jb}\right]^2. \tag{3.14}$$

Under the non-null hypothesis, there is a covariance induced in the Fourier amplitudes inferred between different bands. Therefore, in order to asses the ability of Rubin to synthesize information from different bands, we assume that all measurements are now done with a cadence $\Delta t_b = T/(n_{\rm vis} - 1)$ and a single intensity error. Using this resolution, we plot the covariance between the variability amplitude and timescale in Fig. 3.5. In practice, the AGN shown in Fig. 3.5 are not affected by these assumptions given that we assume that only AGN that are detected at high signal to noise are included in the analysis.

3.1.2.2 AGN Population

Given a set of individual AGN measurements comprising an AGN population, we also infer the precision with which we can measure the variability-timescale relation in Eq (3.7). Thus, we again carry out an expected information analysis using the power spectrum, but now parametrized by population parameters $A_b, \bar{t^r_b}$, and β_b and present the results in Fig. 3.6. Since we assume each AGN in this population is described by the same population parameters, the expected information is now the integral over the expected information

gained from each of these AGN.

3.1.3 Discussion

Five assumptions are worth clarifying. First, we assumed that the AGN variability correlation function between two temporal measurements at t_1 and t_2 is only a function of the time lag $t = |t_2 - t_1|$, i.e. variability is a stationary process. While this is often the case, non-stationarity has been found to exist under certain circumstances. If non-stationarity is a property of a particular class of AGN, then statistics such as the structure function or Wigner function may be utilized instead of the correlation function.

Second, we modeled the correlation function using a damped random walk model, which as we stated previously, is not accurate for all AGN classes. However, for any two parameter model the forecasts presented should be accurate to within orders of unity. Models that include a third parameter, such as a damped random walk with an additional break in the corresponding power spectrum between the white and red noise regimes, will only reduce the fidelity of measurements of the variability amplitude and timescale and are outside the scope of this work.

Third, we assume that the relationship between an AGN and its observed variability timescale can be described by two parameters: its redshift and bolometric luminosity. In reality, we expect other AGN parameters, such as its

color, to also play an important role in determining the timescale within a class of AGN. Such a description of an AGN's variability timescale, while important and necessary for a complete description, is outside the scope of this work.

Fourth, we assumed that the observed frequency of light in a given band is the result of emitted light in the same frequency band. In reality, it is possible that light emitted in a higher frequency band will redshift across lower bands - leading to the final signal be a sum over different frequency bands. As a result, the autocorrelation of a single observed band will be the result of a cross correlation of emitted bands. Moreover, while we focused on variability two-point functions within a given band, the cross correlation between bands of Rubin, as well as between Rubin and other experiments will yield even more information about the structure of the AGN. Time lag measurements between UV/optical light and X-rays have already been used to measure the size regions such as the dust torus and broad-line region. We leave all such calculations for future work.

Lastly, we assumed that the true power spectrum can be recovered through measurements of the power spectrum in a finite box with finite resolution perfectly. For an actual experiment, we expect that measurements of the true power spectrum at Fourier modes close to either limit to be degraded. This degradement can be added in our expected information analysis through the introduction of an additional source of error. However, such error only has an

effect on our final result when the variability timescale of an AGN becomes close to either limit. For a population of AGN, a bulk of them will most likely have variability timescales greater than a few days and less than a few years. As a result, we expect such degrading to not have a drastic impact on our results.

3.1.4 Conclusion

In this work we presented a general framework for measuring the variability amplitude and timescale of any AGN. First, we measured the variability for each AGN and from there construct estimators for the variability correlation function.

Since each timescale estimator was created using the power spectrum at two distinct modes, this introduced covariance between each timescale estimator. However, despite this covariance matrix being non-diagonal, we were able to calculate its inverse. Then, with each timescale estimator and the corresponding covariance matrix, we created a single estimator for the variability timescale using inverse covariance weighting. With an estimator for the variability amplitude and timescale, we then used linear error propagation to calculate the covariance matrix between these two parameters from the initial variability two-point functions. Using this covariance matrix, we forecasted the sensitivity of a Rubin to measuring these parameters. We found that both

the variability amplitude and timescale will be able to be measured up to 10σ across all bands.

Finally, we calculated the theoretical best sensitivity to a Rubin-like experiment measuring a relationship between the luminosity of an AGN and its variability amplitude and timescale. Namely, we used a logarithmic power law model between the luminosity of the AGN and its variability parameters. We found its index to be measured with at least $10^4\sigma$ fidelity.

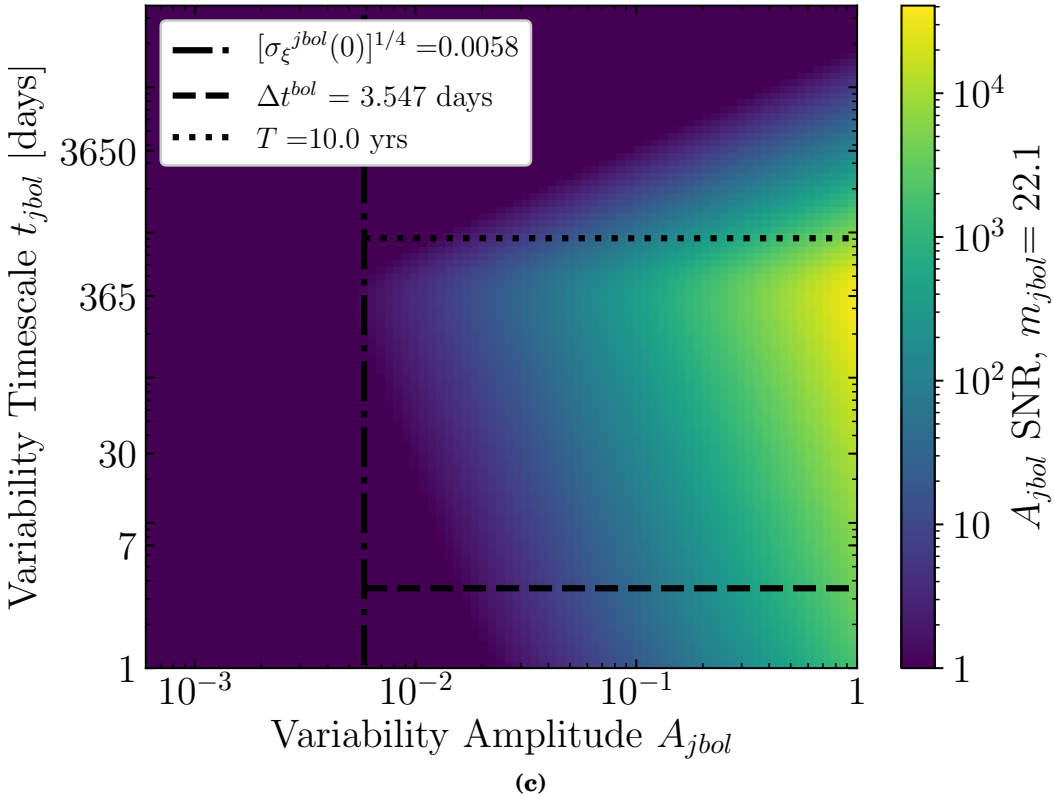

(c)

Figure 3.4: The signal-to-noise-ratio (SNR) in measuring the variability amplitude A_{jb} of AGN j in Rubin frequency band b as a function of the measured variability amplitude and timescale. This forecast is made using the dimmest AGN to be observed $\bar{I}_b^j = I_{\rm bol}(m_{\rm lim}^b, z)$ with noise σ_{jb}, temporal resolution Δt_b, and observation run $T = 10$ years. The three bands presented are Rubin's (a) u (b) i and (c) inferred bolometric bands. When the variability amplitude drops below the noise threshold, as indicated by the dot-dash line, the error becomes too large and the measurement fidelity significantly drops. If the variability timescale is larger than the observation time, as indicated by the dotted line, then all intensity measurements are maximally correlated and the SNR saturates to a constant signal. On the other hand, if the variability timescale is smaller than the temporal resolution, as shown by the dashed line, then each measurement is maximally independent and thus the SNR saturates once more.

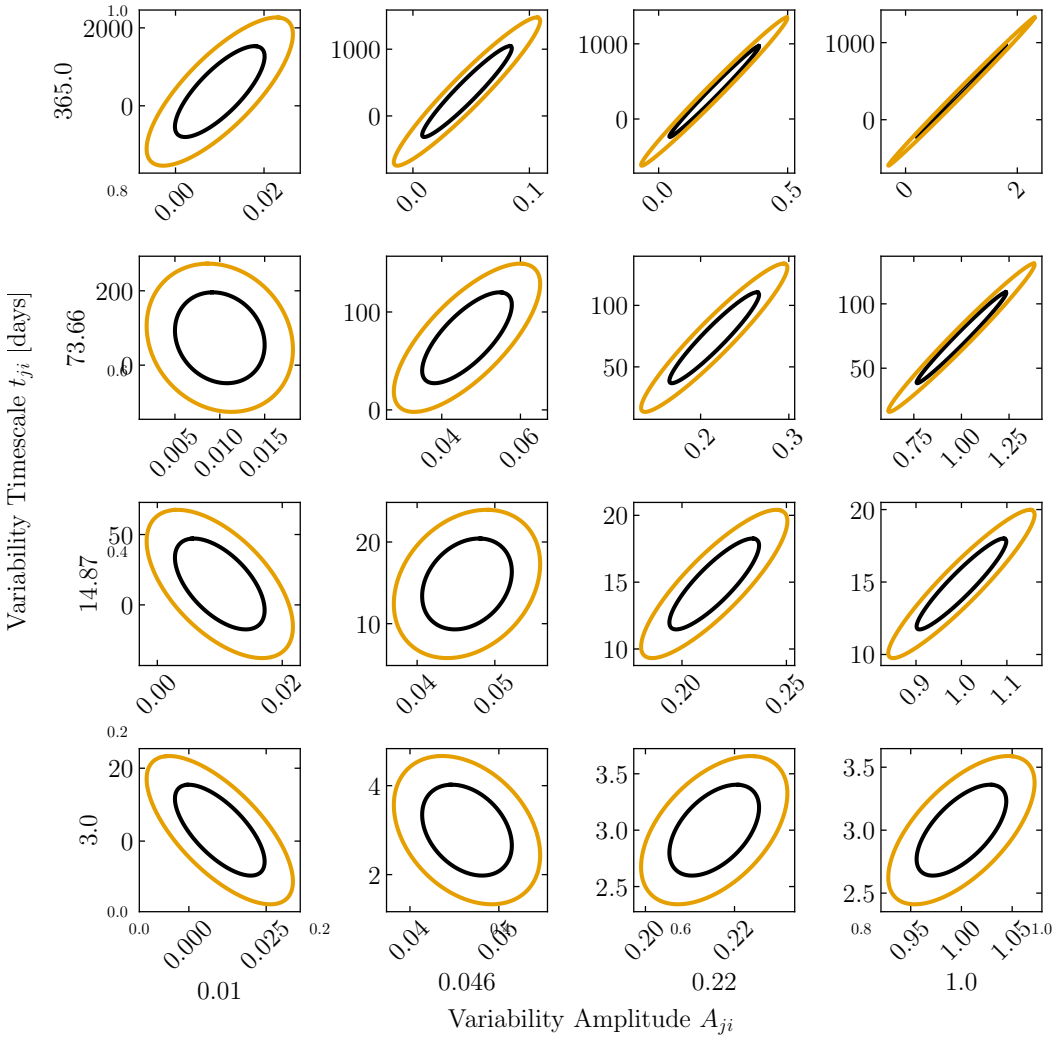

Figure 3.5: The covariance between the variability amplitude A_{ji} and observed timescale $\bar{t}^o_{ji}$ in Rubin's i band for an AGN with apparent magnitude $m_i = 22.3$, corresponding to the average AGN apparent magnitude in the i band. We show the covariance assuming fiducial parameters $A_{ji} \in \{10^{-2}, 4.6 \times 10^{-2}, 2.2 \times 10^{-1}, 1\}$ and $\bar{t}^o_{ji} = \{3 \text{ days}, 14.87 \text{ days}, 73.66 \text{ days}, 365 \text{ days}\}$. The black circles indicates 1σ (68%) confidence, and the yellow 2σ (95%). We note that these results hold for most AGN magnitudes and Rubin frequency bands, as the AGN included in this analysis are all assumed to be detected at high signal to noise. For low amplitude and variability timescale, only modes in the white noise regime, $P \propto (A^2\bar{t})\omega^0$, of the power spectrum are probed, and so there is negative correlation between the two parameters. As the two parameters increase, the red noise regime , $P \propto (A^2/\bar{t})\omega^{-2}$, leads to a positive correlation.

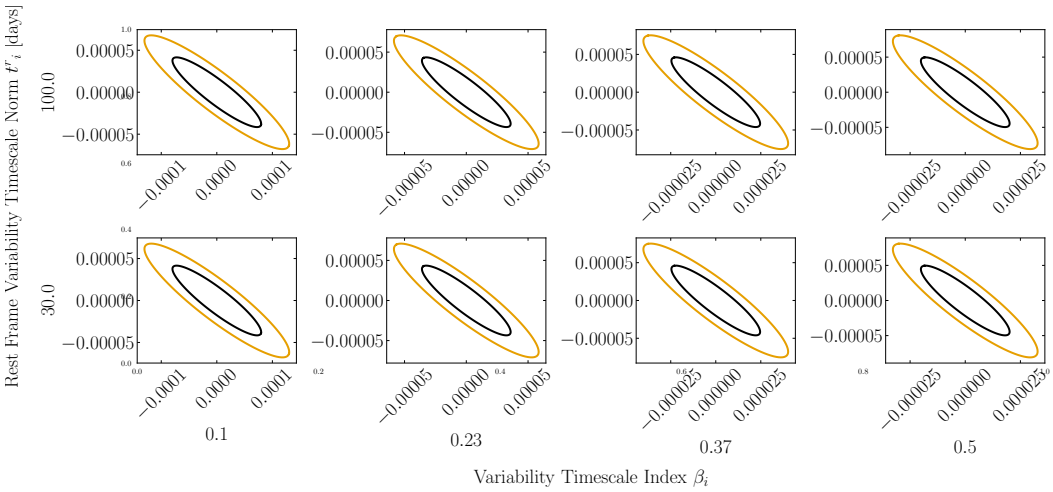

Figure 3.6: The covariance between the variability timescale index and norm in Rubin's i band in terms of the fractional differences $(\beta - \beta_{\rm fid})/\beta_{\rm fid}$ and $(\bar{t}^r - \bar{t}^r_{\rm fid})/\bar{t}^r_{\rm fid}$. We take fiducial parameters $\beta_i \in \{0.1, 0.23, 0.37, 0.5\}$ and $\bar{t}^r_i = \{30 \text{ days}, 100 \text{ days}\}$. The black circles indicate 1σ (68%) confidence, and the yellow 2σ (95%). We note that these results hold for all Rubin frequency bands, as Rubin is limited not by instrumental noise. We take $A_i = 1$. Since increases in both the index β and the norm $\bar{t}_r$ increase the observed variability timescale, they are anti-correlated.

Chapter 4

Neutrinos

4.1 Neutrino Self-Interactions

While the interactions between neutrinos is extraordinarily feeble in the Standard Model, there are a number of reasons to entertain the possibility that new physics may introduce stronger neutrino self-interactions [134–137]. Astrophysical neutrinos may provide a powerful probe in the search for such self-interactions (νSI) [138]. Strong features, such as dips and enhancements, can be imprinted on astrophysical-neutrino spectra, which when analyzed can yield νSI parameter values. In particular, there is the diffuse supernova neutrino background (DSNB) and a collection of high-energy astrophysical neutrino (HEAN) sources. The DSNB is the isotropic time-independent flux of neutrinos and antineutrinos around tens of MeV emitted by distant core-collapse

supernovae [139]. These diffuse sources come from distances around 10 Mpc [140, 141] up to a redshift of 5 with a peak around a redshift of 1 [142]. Moreover, the DSNB has a thermal energy spectrum. In comparison, although HEAN sources have no identified production mechanism, the neutrino's energy spectrum is observed by IceCube to follow a power law [1].

If there are neutrino self-interactions, then interactions of DSNB and/or HEAN neutrinos with low-energy (approximately 0.001 eV) cosmic-background neutrinos can appear in the observed DSNB and/or HEAN spectra as absorption features or enhancements at lower energies. The calculation of the observed flux is straightforward but, most generally, involves solving a series of coupled integro-differential equations that evolve the energy and flavor distribution of neutrinos. These equations describe the injection of neutrinos from sources, the redshifting of neutrinos, the absorption from self-interactions, and the reinjection of lower-energy neutrinos after such interactions. The solutions to these equations require either a Monte Carlo simulation or a straightforward, but computationally intensive, numerical integration of the equations. This thus limits the regions of νSI parameter space that can be investigated. For example, previous work assumed a universal self-coupling matrix [143–147], a diagonal [148] self-coupling matrix, no flavor dynamics [149, 150], or particular values for the mediator mass, coupling constant, and neutrino mass [151–153].

In this work, we present an analytic approach to resonant astrophysical-cosmic-neutrino scattering for arbitrary self-coupling matrix and neutrino number. Here and onward, cosmic neutrinos will refer to cosmic-background neutrinos. This solution is built on the observation that most of observable effects explored in DSNB/HEAN studies arise from resonant neutrino self-interactions. To illustrate the utility of the approach, we then use this solution to explore the discovery space for a model of τ self-interactions (relevant for the DSNB) and another for sterile-neutrino self-interactions (relevant for the HEAN).

This work is organized as follows. In Sec. 4.1.1, we review the general formalism of neutrino mixing and transport. In doing so, we present three formal solutions: first in the case of no interactions, second in the case of only absorption interactions, and third in the case of both absorption and reinjection. We formulate explicit solutions in Sec. 4.1.2 where we specify the nature of neutrino self-interaction. We begin by considering only a single species of neutrino. Then, we generalize this result and present a solution for arbitrary neutrino number and self-coupling matrix. Finally, in Sec. 4.1.3, we use our new solution to identify regions of parameter space that can be accessed. Specifically, we consider DSNB probes of self-interactions with Super-Kamiokande and HEAN probes with IceCube. We discuss and conclude these results in Secs. 4.1.4 and 4.1.5.

4.1.1 General Formalism

4.1.1.1 Neutrino mixing

Neutrinos can be represented in either the mass basis or the flavor basis. In what follows, greek indices are reserved for flavor states, and latin indices are reserved for mass states. In order to switch between the two bases, the neutrino mixing matrix U must be used according to

$$\nu_\alpha = \sum_i U_{\alpha i} \nu_i, \tag{4.1}$$

where the sum is over all mass states and with U unitary. Unitarity implies that for any flavor state α, $\sum_i |U_{i\alpha}|^2 = 1$, and so $|U_{\alpha i}|^2$ is interpreted as the probability that flavor α is observed as mass state i, or *vice versa*.

4.1.1.2 Neutrino transport

The specific flux $\Phi_i(t, E)$ of astrophysical neutrinos ν_i (number of astrophysical neutrinos per unit conformal time per unit comoving area per unit energy) at cosmic time t and observed energy E obeys the Boltzmann equation

$$\begin{aligned} \frac{\partial \Phi_i}{\partial t} &= H\Phi_i + HE\frac{\partial \Phi_i}{\partial E} + S_i(t, E) \\ &\quad - \Gamma_i(t, E)\Phi_i + S_{\mathrm{tert},i}(t, E), \end{aligned} \tag{4.2}$$

where $H(z) = H_0\widetilde{E}(z)$ is the Hubble parameter at redshift z, with z as a proxy for t, and for a Lambda cold dark matter (ΛCDM) cosmology, $\widetilde{E}(z) = [\Omega_m(1+z)^3 + (1-\Omega_m)]^{1/2}$, with Ω_m the matter-density parameter today. When an explicit change of variable is necessary, $t(z) = \int_z^\infty dz'|dt/dz'|$ with $dt/dz = -1/[H(z)(1+z)]$. In addition, S_i is the production rate of astrophysical neutrinos ν_i, Γ_i is the absorption rate of astrophysical neutrinos due to neutrino scatterings, and $S_{\mathrm{tert},i}$ is the tertiary source term accounting for the possible reinjection of astrophysical neutrinos postscattering. Note that by this definition of the specific flux, the comoving number density of astrophysical neutrinos is $(1/c)\int dE\ \Phi_i(t,E)$, different from Refs. [154, 155] where they considered Φ_i to be defined to reproduce the physical number density. Since neutrino decoherence time scales are smaller than any other relevant timescale, the transformation $\Phi_\alpha(t,E) = \sum_i |U_{\alpha i}|^2\Phi_i(t,E)$ can be performed to switch back to the flavor basis at any point. Moreover, if the source terms are given in the flavor basis S_α, then the mass basis source term is $S_i = \sum_\alpha |U_{\alpha i}|^2 S_\alpha$.

In the absence of interactions, $S_{\mathrm{tert},i} = \Gamma_i = 0$, the solution of Eq. (4.2) is obtained by identifying the total time derivative as $d/dt = \partial/\partial t + (dE/dt)\partial/\partial E$, with $dE/dt = -HE$, leading to

$$\Phi_i(t,E) = \int_{-\infty}^{t} dt'[a(t)/a(t')]S_i\{t',[a(t)/a(t')]E\}, \tag{4.3}$$

with $a(t)$ the scale factor at time t. The factor of $[a(t)/a(t')]$ inside the source term accounts for the redshifting of the energy from t' to t, while outside the source term it accounts for the redshifting of the differential energy from t' to t. The addition of a nonzero sink term while neglecting any reinjection, $\Gamma_i \neq 0,\ S_{\mathrm{tert},i} = 0$, does not complicate things much further as then

$$\begin{aligned}\Phi_i(t,E) &= \int_{-\infty}^{t} dt'[a(t)/a(t')]e^{-\tau_i(t',t,E)}S_i\{t',[a(t)/a(t')]E\},\\ \tau_i(t',t,E) &= \int_{t'}^{t} dt''\Gamma_i\{t'',[a(t)/a(t'')]E\},\end{aligned} \tag{4.4}$$

with $\tau_i(t',t,E)$ the optical depth of a neutrino ν_i of energy E between times t' and t. As a result, astrophysical neutrinos at time t' not only go through the previous redshifting, but now travel through a medium of optical depth τ_i from the emission time t' to the observed time t.

Formally, if neutrino reinjection is taken into account, $S_{\mathrm{tert}} \neq 0$, a solution is easily written down,

$$\begin{aligned}\Phi_i(t,E) &= \int_{-\infty}^{t} dt'[a(t)/a(t')]e^{-\tau_i(t',t,E)}\widetilde{S}_i\{t',[a(t)/a(t')]E\},\\ \tau_i(t',t,E) &= \int_{t'}^{t} dt''\Gamma_i\{t'',[a(t)/a(t'')]E\},\\ \widetilde{S}_i(t,E) &= S_i(t,E) + S_{\mathrm{tert},i}(t,E).\end{aligned} \tag{4.5}$$

However, since the tertiary source is a function of the specific flux itself, the

solution is in general not closed. Therefore, if we are to move forward, a particular model must be specified.

4.1.2 Analytical Results

4.1.2.1 Single neutrino species

The particular neutrino model we consider at first is that of a single species of self-interacting neutrinos ν of mass m_ν whose self-interactions are mediated by a scalar particle ϕ with mass m_ϕ and coupling strength g. We ignore the existence of other neutrino species, and as such we suppress any indices present in relevant equations. That is, we initially consider the interacting Lagrangian,

$$\mathcal{L}_{\text{int}}^{1-\nu} = g\phi\nu\nu. \tag{4.6}$$

If this is the case, then astrophysical neutrinos will scatter with cosmic neutrinos, causing depletion of astrophysical neutrinos at a resonant energy $E_R = [m_\phi^2/(2m_\nu)]c^2$ at a rate $\Gamma(t, E) = n_\nu(t)\sigma(E)c$. We define $n_\nu(t)$ to be the physical number density of our single cosmic neutrino species, $\sigma(E)$ to be the scattering cross subsection of the process $\nu\nu \rightarrow \nu\nu$, and c to be the speed of light. After depletion, neutrinos are then reinjected at energies $E < E_R$. We take the

scattering cross subsection to have a Breit-Wigner form,

$$\frac{\sigma(E)}{(\hbar c)^2} = \frac{g^4}{4\pi} \frac{s}{[s-(m_\phi c)^2]^2 + (m_\phi c^2)^2 \Gamma_\phi^2}, \tag{4.7}$$

where $\hbar$ is Planck's constant, $s = 2Em_\nu c^2$, and $\Gamma_\phi = g^2 m_\phi c^2/(4\pi)$ is the decay width. If the width of the resonance is small enough, resonant scattering can be approximated by a Dirac delta function. We now quantify when this occurs. The width of the resonance is where $[s-(m_\phi c^2)^2]^2 < (m_\phi c^2)^2\Gamma_\phi^2$, or stated in terms of energies when $|E - E_R[1 \pm \Gamma_\phi/(m_\phi c^2)]| < 0$, so that the width is $2E_R\Gamma_\phi/(m_\phi c^2)$. For a detector with resolution ΔE, a width cannot be resolved and thus is a delta function if $2E_R\Gamma_\phi/(m_\phi c^2) \lesssim \Delta E$. Therefore, the coupling must satisfy

$$\begin{aligned} g &\lesssim \sqrt{2\pi}(\Delta E/E_R)^{1/2} \\ &\lesssim 0.5 \left[\frac{\Delta E/(1\text{ MeV})}{E_R/(25\text{ MeV})}\right]^{1/2}, \end{aligned} \tag{4.8}$$

where $\Delta E \approx 1$ MeV for a detector such as Super-K [156], and $E_R \approx 25$ MeV for masses $m_\phi c^2 = 1$ keV, $m_\nu c^2 = 2 \times 10^{-2}$ eV. We conclude that, unless the coupling is of order unity, which is most of the available parameter space [149], a detector will not be able to resolve the resonance, and we approximate the cross subsection as a delta function. A nascent delta function in the Breit-Wigner

form is $\delta(x) = \lim_{\epsilon\to 0}(1/\pi)\epsilon/(\epsilon^2 + x^2)$, so that the resulting cross subsection is

$$\sigma(E) = \sigma_R E\delta\left(E - E_R\right), \tag{4.9}$$

with $\sigma_R = (\hbar c)^2\pi g^2/(m_\phi c^2)^2$. Note that Eqs. (4.7) and (4.9) will only yield exactly the same expression once integrated. Resonant scattering is isotropic when the mediator is a scalar field, and therefore the differential cross subsection $d\sigma(E_1, E_3)/dE_3$, where an incoming neutrino with energy E_1 scatters to an outgoing neutrino of energy E_3, has a flat distribution $d\sigma(E_1, E_3)/dE_3 = \sigma(E_1)/E_1$. With this form, we now evaluate the tertiary source for neutrino production in Eq. (4.2).

In our case of cosmic neutrino upscattering, two neutrinos are reinjected after an initial neutrino is taken from the sink term, and cosmic neutrinos have energies much smaller than supernova neutrinos, so their relative velocity is the speed of light. Thus, the tertiary term takes the following expression, converting our initial differential equation into an integro-differential equation:

$$\begin{aligned} S_{\rm tert}(t, E) = n_\nu(t)c \int_E^\infty dE_1 \Phi(t, E_1) \\ \times \left[\frac{d\sigma(E_1, E)}{dE} + \frac{d\sigma(E_1, E_1 - E)}{dE}\right]. \end{aligned} \tag{4.10}$$

With our delta-function approximation, this term is now evaluated as

$$S_{\rm tert}(t,E) = 2\Gamma_R(t)\Phi(t,E_R)\Theta(E_R - E), \tag{4.11}$$

with $\Gamma_R(t) = n_\nu(t)\sigma_R c$ and $\Theta(x)$ the Heaviside function with $\Theta(0) = 0$. Moreover, we simplify the optical depth as

$$\tau(t',t,E) = \tau_R(t,E)\Theta[z_R(t,E) - z]\Theta[z' - z_R(t,E)], \tag{4.12}$$

with z' a proxy for t', $\tau_R(t,E) = [\Gamma_R(z_R)/H(z_R)][(1+z)/(1+z_R)]$, and $z_R = (1+z)E_R/E - 1$ the absorption redshift of a neutrino with energy E. Plugging these expressions into Eq. (4.5) leads to

$$\begin{aligned}\Phi(t,E) &= \int_{-\infty}^{t} dt'\ [a(t)/a(t')]e^{-\tau(t',t,E)}\widetilde{S}\{t',[a(t)/a(t')]E\},\\ \widetilde{S}(t,E) &= S(t,E) + 2\Gamma_R(t)\Phi(t,E_R)\Theta(E_R - E).\end{aligned} \tag{4.13}$$

Thus, for $E \geq E_R$ the spectrum is the same as a no-interaction Boltzmann equation, and so is solved in the same manner. However, when $E < E_R$, neutrinos are reinjected at twice the rate of their depletion at the resonant energy. As such, the expression for neutrino reinjection still requires solving for the specific flux at $E = E_R$ and plugging it back in for evaluation at lower energies, which at first makes Eq. (4.13) seem not closed. However, Eq. (4.2) has a delta

function via the absorption term $\Gamma(t,E)\Phi = n_\nu(t)\sigma(E)c\Phi$ at the resonant energy, and so we must obey the boundary condition at this point. In order to satisfy this condition, we integrate Eq. (4.2) around the resonant energy from below the resonance $E_R^- \equiv E_R - \epsilon/2$ to above the resonance $E_R^+ \equiv E_R + \epsilon/2$ and take the line width $E_R^+ - E_R^- = \epsilon$ to zero. Explicitly, this results in

$$H(t)\left[\Phi(t,E_R^+) - \Phi(t,E_R^-)\right] = \Gamma_R(t)\Phi(t,E_R). \tag{4.14}$$

Again, above the resonant line the optical depth of free-streaming with no interactions is zero, while below, it is $\tau(t',t,E_R^-)$, so that the resulting expression for $\Phi(t,E_R)$ is

$$\Phi(t,E_R) = \frac{H(t)}{\Gamma_R(t)}\int_{-\infty}^{t} dt'[a(t)/a(t')]\left[1-e^{-\tau_R(t,E)}\right] \times S\{t',[a(t)/a(t')]E_R\}. \tag{4.15}$$

As a result, Eq. (4.13) has a closed form expression. Since cosmic neutrinos are low energy, astrophysical-cosmic neutrino scattering does not add nor remove energy from the astrophysical neutrino spectra but only redistributes it. We have checked both analytically and numerically that Eq. (4.13) obeys this condition.

There are two differences in the expression for Φ between Eqs. (4.13) and (4.15).

First is the presence of the factor $1 - e^{-\tau}$ rather than $e^{-\tau}$. This factor can be understood as follows: after an astrophysical neutrino redshifts through a resonance over a short period of time, the specific flux at the resonant energy only has a fraction $e^{-\tau}$ remaining of the original flux. It follows then that the amount that is injected at lower energies must be the complementary fraction, $1-e^{-\tau}$. The second difference is the factor of $H(t)/\Gamma_R(t)$, which changes the rate of injection from $\Gamma_R(t)$ in Eq. (4.5) to $H(t)$. This change in the rate of injection is due the resonance line redshifting in time. If the scattering rate is faster than Hubble, then the flux of neutrinos at the resonant energy is suppressed. Conversely, if the rate is slower, then the scatterings have little effect.

4.1.2.2 Multiple neutrino species

In the presence of multiple neutrino species, the previous equations do not hold. Here we present the analogous calculation with additional neutrinos, taking the mass of each neutrino species to be m_j with corresponding cosmic physical number density n_j. The interaction Lagrangian term for the most general mass-basis interaction with a scalar mediator ϕ of mass m_ϕ is given by

$$\mathcal{L}_{\text{int}}^{\text{mass}} = \phi \sum_{ij} g_{ij} \nu_i \nu_j, \tag{4.16}$$

with g_{ij} the self-coupling matrix. In this model, astrophysical neutrinos scatter off of one of any of the cosmic neutrino species, causing depletion of astrophysical neutrinos at corresponding resonant energies $E_j = [m_\phi^2/(2m_j)]c^2$ at a rate $\Gamma_i \equiv \sum_j n_j \sigma_{ij} c$. The cross subsection $\sigma_{ij} \equiv \sum_{kl} \sigma_{ijkl}$ is the sum of scattering cross subsections for the processes $\nu_i \nu_j \to \nu_k \nu_l$. We take σ_{ijkl} to have the Briet-Wigner form

$$\frac{\sigma_{ijkl}(E)}{(\hbar c)^2} = \frac{|g_{ij}|^2 |g_{kl}|^2}{4\pi} \frac{s_j}{[s_j - (m_\phi c)^2]^2 + (m_\phi c^2)^2 \Gamma_\phi^2} \tag{4.17}$$

with $s_j = 2E m_j c^2$ and $\Gamma_\phi = \left(\sum_{ij} |g_{ij}|^2\right) m_\phi c^2/(4\pi)$ the decay width. Note that the decay width has changed since there now exists multiple decay branches for ϕ. After depletion, the neutrinos are reinjected at a rate according to

$$\begin{aligned} S_{\mathrm{tert},i}(t, E) = \sum_{jkl} n_k(t) c \int_E^\infty dE_1 \Phi_j(t, E_1) \\ \times \left[\frac{d\sigma_{jkil}(E_1, E)}{dE} + \delta_{il} \frac{d\sigma_{jkil}(E_1, E_1 - E)}{dE} \right], \end{aligned} \tag{4.18}$$

with δ_{il} the Kronecker delta function that accounts for the possibility of upscattering into two astrophysical neutrinos of the same state rather than just one. That is, compared to the single neutrino species case, this expression accounts for production of neutrinos of type i from an astrophysical flux Φ_j hitting a cosmic neutrino density n_k, with i, j, k not necessarily all being the

same. Once again, the differential cross subsection takes a flat distribution $d\sigma_{ijkl}(E_1, E_3)/dE_3 = \sigma_{ijkl}(E_1)/E_1$. Moreover, using our delta function limit, the cross subsection takes the form $\sigma_{ijkl}(E) = \sigma_R^{ijkl} E\delta(E - E_j)$ with $\sigma_R^{ijkl} = (\hbar c)^2 |g_{ij}|^2 |g_{kl}|^2/[4(m_\phi c^2)\Gamma_\phi]$. As a result, the tertiary source term is

$$S_{\text{tert},i}(t, E) = \sum_{jkl} (1 + \delta_{il})\, \Gamma_R^{jkil}(t) \Phi_j(t, E_k) \Theta(E_k - E),$$

with $\Gamma_R^{jkil}(t) = n_k(t)\sigma_R^{jkil} c$. In addition, the optical depth is

$$\tau_i(t', t, E) = \sum_j \tau_R^{ij}(t, E) \Theta[z_j(t, E) - z] \Theta[z' - z_j(t, E)], \tag{4.19}$$

with $\tau_R^{ij}(t, E) = [\Gamma_R^{ij}(z_j)/H(z_j)][(1 + z)/(1 + z_j)]$, $\Gamma^{ij} = \sum_{kl} \Gamma_R^{ijkl}$, and $z_j = (1 + z)E_j/E - 1$. Analogous to before, we satisfy the boundary condition around each resonance by the conditions

$$H(t)[\Phi_i(t, E_j^+) - \Phi_i(E_j^-)] = \Gamma_R^{ij}(t) \Phi_i(t, E_j). \tag{4.20}$$

Now, it is true that only above the highest resonant line, the optical depth is zero. Thus, the general solution is

$$\begin{aligned}
\Phi_i(t,E) &= \int_{-\infty}^{t} dt'[a(t)/a(t')]e^{-\tau_i(t',t,E)}\widetilde{S}_i\{t',[a(t)/a(t')E]\},\\
\widetilde{S}_i(t,E) &= S_i(t,E) + \sum_{jkl}(1+\delta_{il})\,\Gamma_R^{jkil}(t)\Phi_j(t,E_k)\Theta(E_k-E),\\
\Phi_i(t,E_j) &= \frac{H(t)}{\Gamma_R^{ij}(t)}\int_{-\infty}^{t} dt'\frac{a(t)}{a(t')}e^{-\tau_i(t',t,E)}\left[1-e^{-\tau_R^{ij}(t,E)}\right]\\
&\qquad\qquad \times \widetilde{S}_i\{t',[a(t)/a(t')]E_j\}. \qquad (4.21)
\end{aligned}$$

Then, when we want to convert back to the flavor basis we use the neutrino mixing matrix once again. Equation. (4.21) is our main result that describes the propagation of multiple astrophysical neutrinos species that self-interact arbitrarily with cosmic neutrinos. If a flavor self-coupling matrix is given instead, the identification $g_{ij} = \sum_{\alpha\beta} U_{i\alpha}U_{j\beta}g_{\alpha\beta}$ leads to an easy substitution. We present the analogous equations with this substitution in Appendix 4.1.6.

Note, however, that in order to solve Eq. (4.21) in a closed manner, the highest resonant boundary condition must be solved for first, as it is a function of only the source S_i and scattering rate Γ_i. This is to be contrasted with the boundary conditions for lower resonant energies, which depend not only on these quantities but also the flux at higher resonances. This dependence arises because a neutrino can be absorbed at a resonance E_j, downscattered to an en-

ergy $E > E_k$, with $E_k < E_j$ some other resonance, and then be redshifted down to E_k. In this way, astrophysical neutrinos may cascade down the resonance pipeline until they reach energies below the lowest resonant energy.

4.1.3 Numerical Results

Given these analytic results, a wealth of neutrino self-interactions can be explored and constrained. However, due to the large dimensionality of the general problem, we narrow our scope to two specific models. Moreover, many factors aside from neutrino self-interactions can affect the resulting spectrum, such as detector backgrounds and energy thresholds. Such a detailed analysis, however, is outside the scope of this work. That is, we consider only a single source of neutrinos with shot-noise error. Specifically, first we consider the standard three-neutrino model, adjoined with a τ self-interaction coupling constant $g_{\tau\tau}$. Interactions of this form have been proposed to resolve the Hubble tension [157, 158], although our analysis does not rely on this explanation.

Second, we add a sterile neutrino to the three-neutrino model, along with a sterile s self-interaction coupling constant g_{ss}. This case is motivated by the LSND, MiniBooNE and reactor anomalies which suggest mixing with eV-scale sterile neutrinos [159–167]. While such mixing would be in tension with Planck, self-interactions of the sterile neutrino by a mediator of mass $m_\phi \lesssim \mathrm{MeV}$ would bring results back into harmony [168, 169]. In both models, we

consider all other neutrino self-coupling constants are taken to be zero.

In order to apply Eq. (4.21) to the four-neutrino case, we need to choose definite values for the mixing matrix elements. We use a standard parametrization [170],

$$U = R^1(3,4)R^0(2,4)R^1(1,4)R^0(2,3)R^1(1,3)R^0(1,2), \tag{4.22}$$

with $R^c(a,b)$ a 4×4 rotation matrix with matrix elements $R^c(a,b)_{ij}$ and a mixing angle θ_{ab}. The matrix elements are those of the 4×4 identity except for the following submatrix,

$$\begin{pmatrix} R^c(a,b)_{aa} & R^c(a,b)_{ab} \\ R^c(a,b)_{ba} & R^c(a,b)_{bb} \end{pmatrix} = \begin{pmatrix} c_{ab} & s_{ab}e^{-ic\delta_{ab}^{\mathrm{CP}}} \\ -s_{ab}e^{ic\delta_{ab}^{\mathrm{CP}}} & c_{ab} \end{pmatrix}, \tag{4.23}$$

where $s_{ab} = \sin(\theta_{ab})$ and $c_{ab} = \cos(\theta_{ab})$, and $\delta_{ab}^{\mathrm{CP}}$ is a complex CP violating phase. In general, there are also Majorana phases associated with the mixing matrix, but since we are considering lepton-conserving processes, we neglect them [171].

In the limiting case of no mixing between active and sterile neutrino states, $\theta_{14} = \theta_{24} = \theta_{34} = 0$, each of $R^1(3,4)$, $R^0(2,4)$, and $R^1(1,4)$ is the identity, and we obtain the standard three-neutrino mixing matrix [172] plus a decoupled sterile state. Note that in this model, we consider self-interactions only among

sterile neutrinos, so in this no-mixing limit, our astrophysical spectra will return to the standard expectation, regardless of the value of g_{ss}. Motivated by the short-baseline anomalies, we take $\theta_{14} = \theta_{34} = 0$ and $\sin^2(\theta_{24}) = 0.1$, so $\theta_{24} = 0.161$.

In addition to the mixing matrix, the neutrino mass spectrum $\vec{m}$ is also constrained. We first review the constraints on the lightest three neutrinos. Oscillation experiments give the value of two mass-squared differences [173]. As a result, it is unclear whether the neutrino mass spectrum follows a normal hierarchy (NH) $m_1 < m_2 < m_3$ or inverted hierarchy (IH) $m_3 < m_1 < m_2$. However, a lower bound on the neutrino masses is obtained by setting $m_1 = 0$ in the NH and $m_3 = 0$ in the IH. In addition, an upper bound is obtained from Planck [73], as it constrains the sum of neutrino masses to be such that $\sum_j m_j c^2 < 0.12\ \mathrm{eV}$. As a result, the following table of neutrino mass constraints can be made:

	m_1c^2 (eV)	m_2c^2 (eV)	m_3c^2 (eV)
NH	$[0, 0.030]$	$[0.0087, 0.031]$	$[0.050, 0.059]$
IH	$[0.050, 0.052]$	$[0.051, 0.053]$	$[0, 0.015]$

. This table implies that, no matter the hierarchy, we know there exists a neutrino with mass $mc^2 \in [0.050, 0.059]\ \mathrm{eV}$. Thus, there is at least one cosmic neutrino that is cold today. As an exemplar case of multiple resonances, we choose

our three-neutrino mass spectrum to be the heaviest normal hierarchy allowed $\vec{m}_{\rm HNH}c^2 = [0.030, 0.031, 0.059]$ eV. When considering sterile self-interactions, we add to the heaviest normal hierarchy an eV-mass neutrino, leading to a sterile normal hierarchy $\vec{m}_{\rm SNH}c^2 = [0.03, 0.031, 0.059, 1.0]$ eV.

The mass of the mediator is chosen to correspond to the energy ranges dictated by the sources we choose. That is, for an experiment that measures spectra between neutrino energy ranges $[E_{\rm min}, E_{\rm max}]$, the range of mediators that can be be probed is $E_{\rm min} \leq [m_\phi^2/(2m_j)]c^2 \leq E_{\rm max}$ for each neutrino mass $m_j \in \vec{m}$. In order to simplify our analysis, we only compare the null hypothesis with our model at the resonant energies, and not the entire spectrum. Finally, we choose a fixed bin size for each constraint.

We denote the event count under the null hypothesis $g_{ij} = 0$ by $N_{\rm null}$. Thus, assuming only Poisson shot noise error, we find that the number of events $N_{\rm events}$ in each bin can be measured away from the null hypothesis with a signal to noise

$$\left(\frac{S}{N}\right)^2 = \frac{(N_{\rm events} - N_{\rm null})^2}{N_{\rm events} + N_{\rm null}}. \tag{4.24}$$

Therefore, the number of events needed to distinguish from the null hypothesis

$N_{\text{events}} = N_{\text{null}}$ is

$$N_{\pm} = N_{\text{null}} + (S/N)^2/2 + (S/N)_{\pm}\sqrt{2N_{\text{null}} + (S/N)^2/4}, \tag{4.25}$$

with $(S/N)_{\pm} = \pm|(S/N)|$. $N_{\pm}$ is also known as the (S/N)-σ uncertainty in the measurement of N_{null}, with N_{+} the upper and N_{-} the lower uncertainty. Again, for our analysis, we only use N_{-} when looking for depletions.

4.1.3.1 DSNB

The production rate of neutrinos per comoving area per unit time per unit energy from core-collapse supernovae (CCSN) is $S_i(t, E) = cR_{\text{CCSN}}(z)dN_i(E)/dE$ [174], with R_{CCSN} the CCSN rate per comoving volume and dN_i/dE the number spectrum of neutrinos of type i emitted by one supernova explosion. For R_{CCSN}, we use the parametrization of Ref. [142] with the lower bound of the Salpeter initial mass function. Moreover, we assume equipartition of energy among neutrino species and thus approximate the spectrum of one neutrino species by a Fermi-Dirac distribution with zero chemical potential [175],

$$\frac{dN_i}{dE} = \frac{120}{7\pi^4}\frac{E_{\text{tot}}}{6}\frac{E^2}{(k_B T_{\text{SN}})^4}\frac{1}{1 + e^{E/(k_B T_{\text{SN}})}}, \tag{4.26}$$

with $E_{\text{tot}} = 3\times10^{46}$ J the total energy in neutrinos emitted by the supernova and $4\ \text{MeV} \leq k_B T_{\text{SN}} \leq 8\ \text{MeV}$ the supernova temperature [139]. We plot two possible

flux spectra Φ_e of electron antineutrinos from the DSNB in Fig. 4.1 for T. While a supernova temperature $k_B T_{\rm SN} = 8$ MeV is disfavored, it does not heavily alter our conclusions. For the heaviest normal neutrino mass hierarchy, three resonances are potentially observable when flavor self-interactions are considered. While not observed yet, the addition of gadolinium sulfate to large water Cerenkov detectors would allow for the discrimination, and thus detection, of DSNB events from spallation and atmospheric neutrino events [176, 177].

Electron antineutrinos in the DSNB are in the correct energy regime to be detected through inverse beta decay scattering at Super-Kamiokande [156]. Specifically, through the process $\bar{\nu}_e p \to e^+ n$, DSNB antineutrinos collide with water molecules in Super-Kamiokande, producing a positron that emits Cherenkov radiation that is detectable. As a result, the colliding antineutrino must have minimum energy $E_\nu^{\rm min} = m_e c^2 + \Delta = 1.806$ MeV, with $\Delta = (m_n - m_p)c^2$. In the following, we use Eq. (25) of Ref. [178] for the inverse beta decay cross subsection $\sigma_{\rm IBD}$. The number $N_{\rm events}$ of events detected in a positron energy bin $[E_{e^+}, E_{e^+} + \delta E]$ is then

$$N_{\rm events} = T N_p \int_{E_{e^+}}^{E_{e^+}+\delta E} dE \Phi_e(E + \Delta) \sigma_{\rm IBD}(E), \tag{4.27}$$

with T the time of observation and N_p the number of scattering targets. Note that in this expression, $E + \Delta$ is the neutrino energy, while E is the positron

energy.

We show the event counts and uncertainties corresponding to Fig. 4.1 in Fig. 4.2. Comparing our null hypothesis to our model at the resonant energies, we obtain the forecasted 1σ constraints in Fig. 4.3.

4.1.3.2 High-energy astrophysical neutrinos

The production rate of high-energy astrophysical neutrinos per comoving area per unit time per unit energy is $\mathcal{L}(z, E) = \mathcal{W}(z)\mathcal{L}_0(E)$, with $\mathcal{L}_0$ the differential number luminosity for each source and $\mathcal{W}$ the redshift evolution of the source density. We take the redshift evolution to follow the star-formation rate, $\mathcal{W}(z) = R_{\rm CCSN}(z)$. Moreover, following IceCube's 6 year data analysis [1], we take the differential number luminosity to be a power law $\mathcal{L}_0 \propto (E/E_0)^{-\gamma}$. We plot two possible flux spectra Φ_e of electron antineutrinos in Fig. 4.4. The number of events observed by IceCube is [179]

$$N_{\rm events} = T \int_{E_{\rm casc}}^{E_{\rm casc}+\delta E} dE \Phi_e(E) A_{\rm eff}(E), \tag{4.28}$$

with T the time of observation, $E_{\rm casc}$ the cascade energy, and $A_{\rm eff}(E)$ the IceCube effective area, which we take from Ref. [180]. When a neutrino hits a nucleon in IceCube, the relevant process is via charged current interactions whereby a hadronic cascade and an electron or positron are produced. The pro-

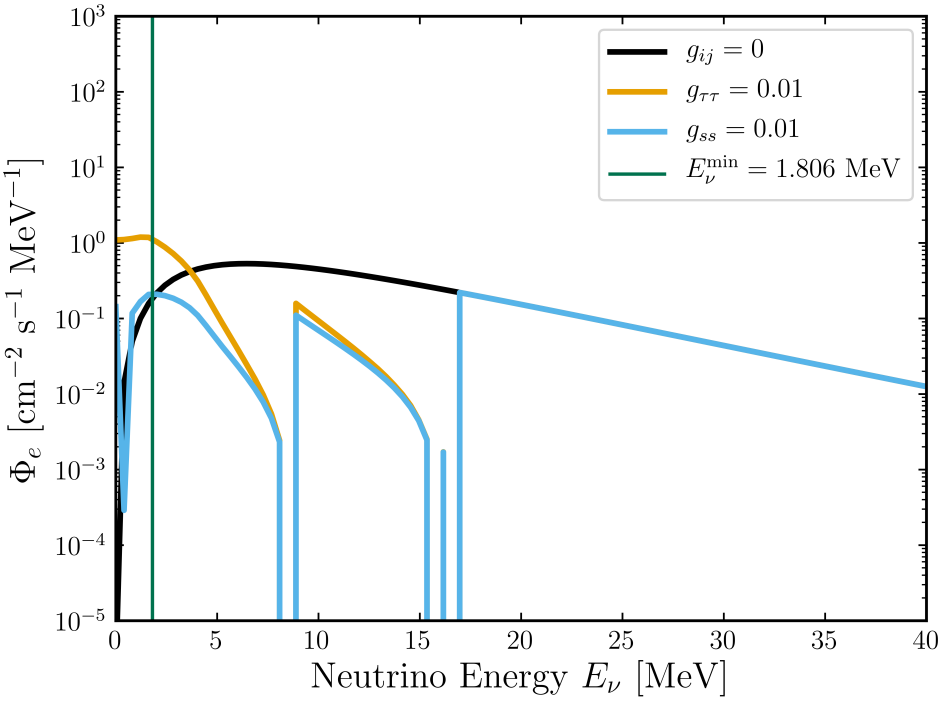

Figure 4.1: The DSNB specific flux of electron antineutrinos Φ_e. The forest green line indicates the minimum energy $E_\nu^{\min} = 1.806$ MeV needed for neutrinos to undergo inverse beta decay. The black line $g_{ij} = 0$ has no self-interactions. For τ self-interactions $g_{\tau\tau}$ three resonances are visible, while for s self-interactions g_{ss} four are visible. In both cases, there is a nearly degenerate pair of resonances. In addition to the dips, an enhancement is present for energies $E_\nu \lesssim 4$ MeV for $g_{\tau\tau} = 0.01$, as there is no dip from a fourth neutrino. The mass spectrum is $\vec{m}_{\rm HNH}$ ($\vec{m}_{\rm SNH}$) for the three-(four-)neutrino model. The mediator mass is $m_\phi c^2 = 1$ keV, and the supernova temperature is $k_B T_{\rm SN} = 8$ MeV.

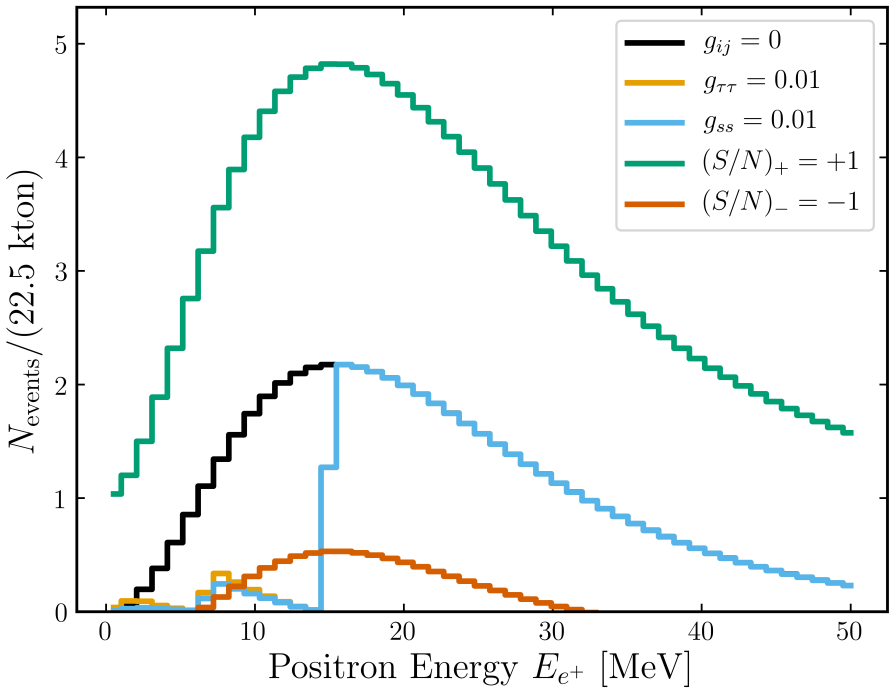

Figure 4.2: DSNB event counts N_{events} vs positron energy E_{e^+} at Super-K with gadolinium after $T = 10$ years with $\delta E = 1$ MeV energy bins. The upper and lower uncertainties on the $g_{ij} = 0$ event count are shown for $(S/N)_\pm = \pm 1$. In both alternative models, self-interactions are ruled out as the resonant energy count is below the 1σ uncertainty. However, they cannot be distinguished from one another due to their similar profiles. The model parameters are the same as in Fig. 4.1.

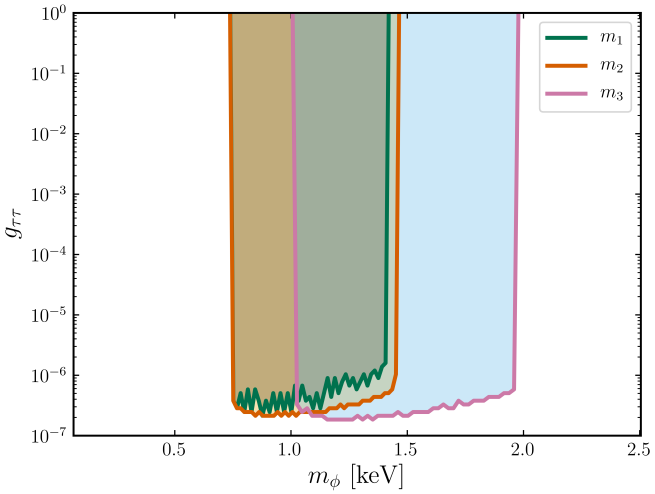

(a)

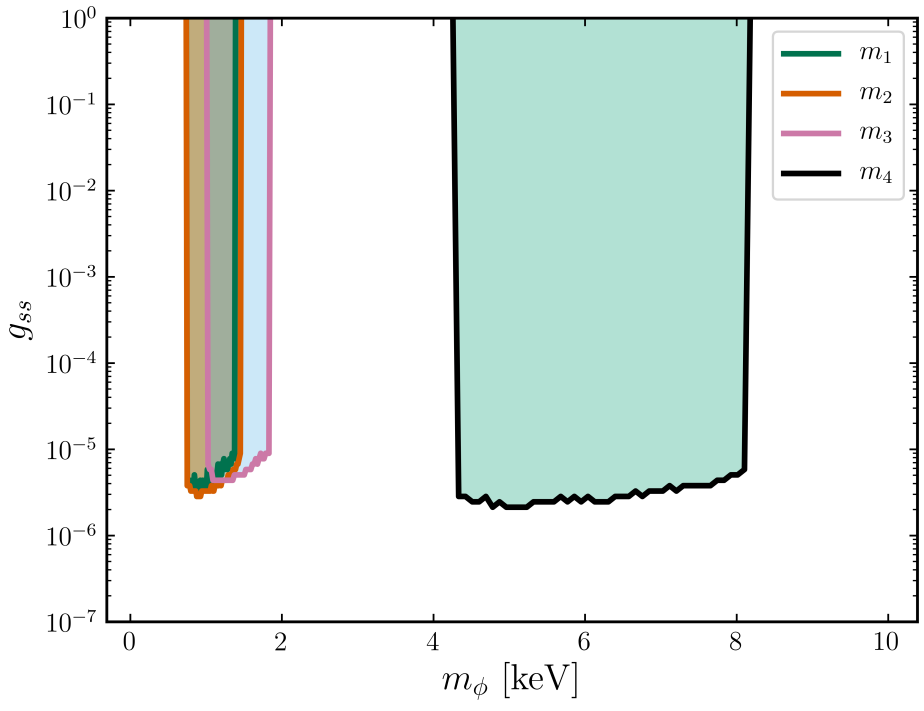

0.7

(b)

Figure 4.3: Forecasted 1σ constraints on flavor self-interactions from a cosmic neutrino mass spectrum (a) $\vec{m}_{\rm HNH}c^2 = [0.030, 0.031, 0.059]$ eV and (b) $\vec{m}_{\rm SNH}c^2 = [0.031, 0.031, 0.059, 1.0]$ eV interacting with the DSNB observed at Super-K with gadolinium for $T = 10$ years. Each neutrino mass m_j corresponds to a different constraint region, denoted by the filled in regions. The jagged edges are due to numerical error.

duced lepton then leads to an electromagnetic cascade. Both of these cascades approximately have a spherical distribution and are detected by phototubes in IceCube. IceCube can then recover the initial neutrino energy with high accuracy. Therefore, we approximate the cascade energy to be the neutrino energy.

We show the event counts and uncertainties corresponding to Fig. 4.4 in Fig. 4.5.

Comparing our null hypothesis to our model at the resonant energies, we obtain the forecasted 1σ constraints in Fig. 4.6.

4.1.4 Discussion

Several points are worth examining in further depth. First, Eq. (4.21) only holds when each cosmic neutrino species is cold. However, we know there exists at least one cold neutrino species. Therefore, in the case where one or more cosmic neutrino species are not cold, this equation is modified so that any sum over neutrino scattering cross subsections is only over all cold species. Moreover, interactions with the lower-mass neutrinos should be suppressed relative to that of the heavier cold species due to thermal broadening.

Second, the spectra shown all have three resonances, and this not need be the case. The heaviest allowed normal neutrino mass hierarchy is special in this case, since the nearly degenerate pair have masses much larger than any neutrino mass splitting. In the inverted scenario, this cannot be the case,

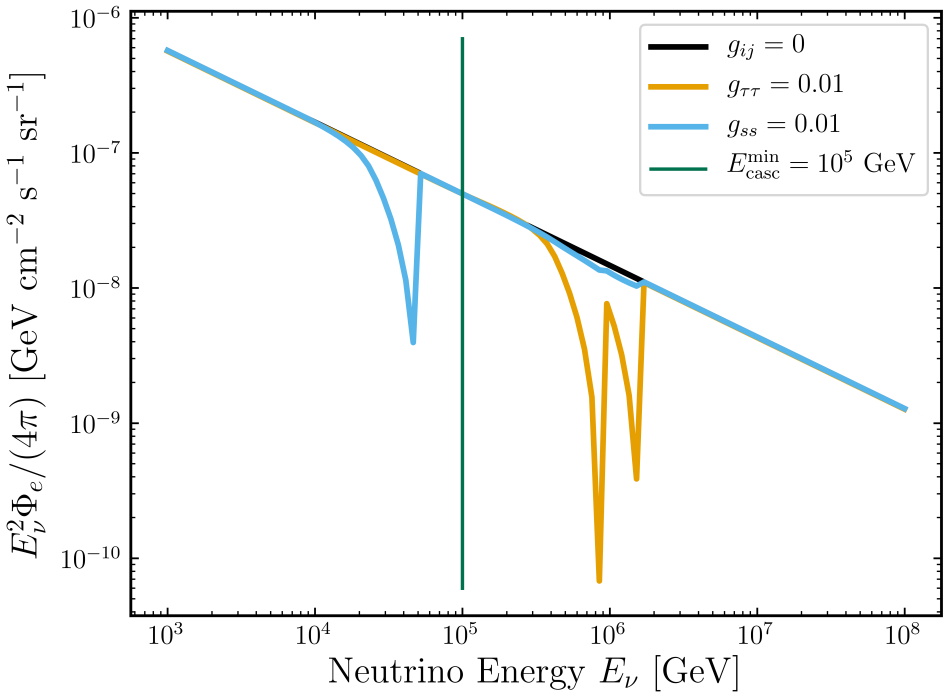

Figure 4.4: The specific flux per steradian $\Phi_e/(4\pi)$ of high-energy astrophysical electron antineutrinos. The forest green line indicates the minimum energy $E_{\rm casc}^{\rm min} = 10^5$ GeV needed to be above the atmospheric neutrino background. The black line $g_{ij} = 0$ has no self-interactions. For the τ self-interactions $g_{\tau\tau}$, two resonances are visible, while for s self-interactions g_{ss}, one is visible. In the $g_{\tau\tau}$ case, there is a degenerate pair of resonances that cannot be resolved. For $g_{ss} = 0.01$, three resonances are below the threshold for strong absorption. No enhancement is present for low energies as the spectrum monotonically decays. The mass spectrum is $\vec{m}_{\rm HNH}$ ($\vec{m}_{\rm SNH}$) for the three-(four-)neutrino model. The mediator mass is $m_\phi c^2 = 10$ MeV. We take the power law index to be $\gamma = 2.53$ and $E_0 = 100$ TeV. In addition, we normalize the final flux at energy E_0 so that $E_0^2 \Phi_e(E_0)/(4\pi) = C_0 \Phi_0$, with $C_0 = 3 \times 10^{-18}$ GeV^{-1}cm^{-2}s^{-1}sr^{-1} and $\Phi_0 = 1.66$ in accordance with IceCube [1].

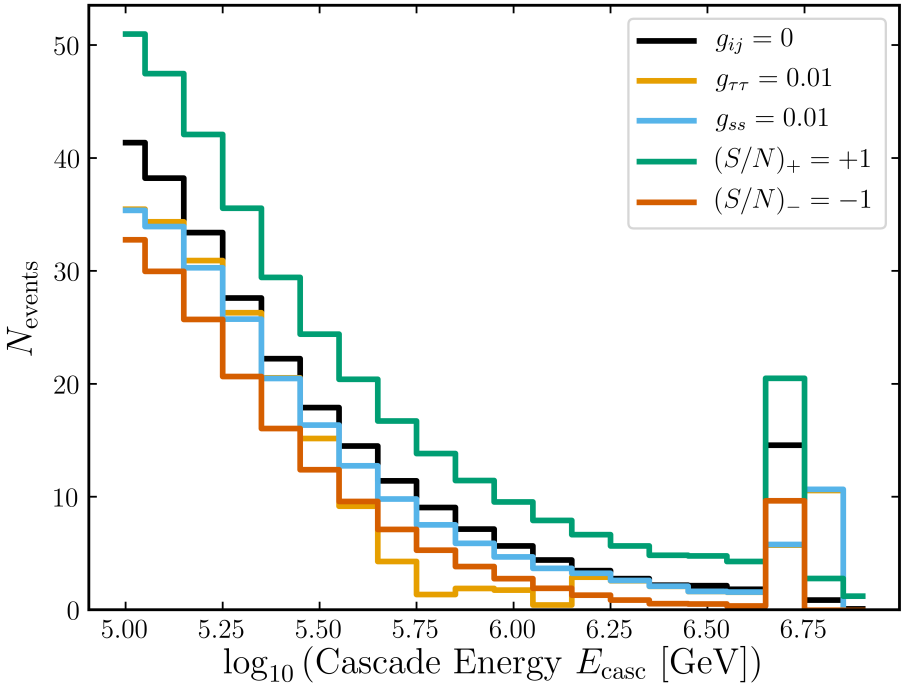

Figure 4.5: High-energy astrophysical neutrino event counts N_{events} vs cascade energy E_{casc} at IceCube after $T = 988$ days with $\delta \log_{10}[E/(1\text{ GeV})] = 0.1$ log-energy bins. The upper and lower uncertainties on the $g_{ij} = 0$ event count are shown for $(S/N)_\pm = \pm 1$. The $g_{\tau\tau} = 0.01$ self-interaction model is ruled out as the resonant energy count is below the 1σ uncertainty. The model parameters are the same as in Fig. 4.4.

and so at most, two resonances could be seen in any spectrum that does not have a large energy range. If a single resonance is seen, it is unclear how to disentangle the two scenarios, but such distinction is outside the scope of this work.

Third, while we made our constraints by looking for absorption features, one in principle could also look for enhancements in spectra. In experiments, it

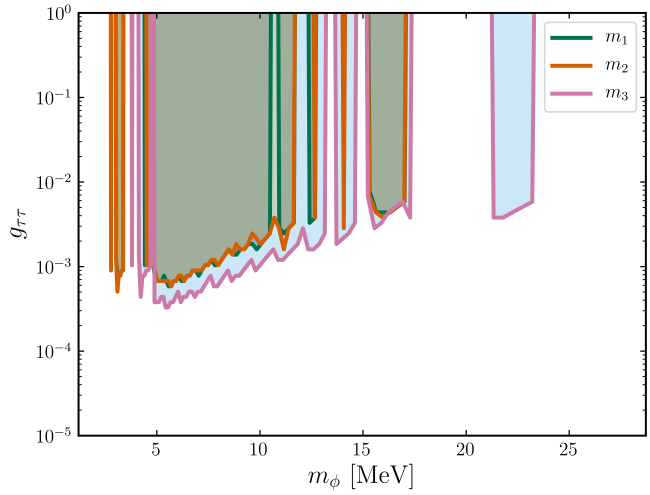

(a)

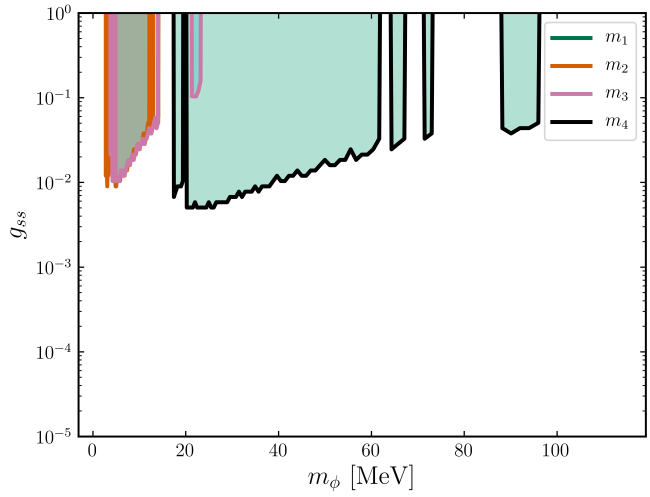

(b)

Figure 4.6: Forecasted 1σ constraints on flavor self-interactions from a cosmic neutrino mass spectrum (a) $\vec{m}c^2 = [0.030, 0.031, 0.059]$ eV and (b) $\vec{m}c^2 = [0.031, 0.031, 0.059, 1.0]$ eV interacting with HEAN observed at IceCube for $T = 988$ days. Each neutrino mass m_j corresponds to a different constraint region, denoted by the filled in regions. The jagged edges are due to numerical error.

is simple as one needs to look for when the signal surpasses some threshold for statistical significance, $N_{\rm events} > N_+$. However, it is less obvious theoretically what bins or how many bins one should look at in order to create a forecasted constraint from enhancements in a time-efficient manner. It depends on the number of resonances, the shape of the null hypothesis spectrum, and the detection method. For example, in the DSNB, the enhancements are much more pronounced at low energy compared to HEAN sources, since at low energies the DSNB spectrum falls off while the HEAN source spectrum grows.

Fourth, we wrote down our formulas assuming a single scalar ϕ; however, it is straightforward to generalize to multiple scalars ϕ_k with self-coupling matrices g^k_{ij}. The only possible subtlety is if degeneracies in the resonances occur, in which case the resonant condition needs to be altered accordingly by a sum over degenerate resonances.

Fifth, while this work is focused on neutrino self-interactions, it is also straightforward to incorporate arbitrary resonant scattering between any species. The most obvious other cold species to generalize to would be cold dark matter.

Sixth, when constraining self-interactions, we only took information about the shape of the flux of one neutrino flavor at a time. Combining multiple flavors will lead to stronger constraints if the detection of them is feasible.

Finally, we took the noise to be only Poissonian and assumed fiducial astrophysical parameters. In a realistic experiment, other backgrounds must be

taken into account as well as degeneracies with their parameters. However, such a proper treatment, similar to Refs. [150, 181, 182], is outside the scope of this work.

4.1.5 Conclusion

In this work, we have have considered the consequence of beyond the Standard Model neutrino self-interactions on various astrophysical neutrino spectra. We began by presenting the necessary formalism for neutrino mixing and transport. We did this not only to establish notation but also in order to demonstrate that neutrino reinjection is a problem that is generally not closed.

In order to overcome this hurdle, we then took the limit where the scattering cross subsection goes to a delta function and found that the former partial integro-differential equations turn into a standard partial differential equation with simple boundary conditions. As a result, we then presented the solution for astrophysical neutrino spectra for a single neutrino species, following with one for an arbitrary number of neutrino species. These solutions were specified in either the mass basis or the flavor basis.

From this, we then demonstrated the utility of the analytic solution by considering our astrophysical sources to be either the diffuse supernovae background or high-energy astrophysical neutrinos. From there, we established forecasts and constraints on a normal three-neutrino hierarchy with τ self-

interactions, as well as a four-neutrino hierarchy with sterile self-interactions. None of these calculations took a significant amount of time, and they were routine in their implementation.

It will be interesting to implement this calculation in future work to explore the effects of neutrino self-interactions on DSNB and HEAN spectra for a wider range of models that involve new neutrino interactions.

4.1.6 Flavor basis interactions

We consider the most general flavor interaction for a single scalar mediator ϕ of mass m_ϕ,

$$\begin{aligned}\mathcal{L}_{\text{int}}^{\text{flavor}} &= \phi \sum_{\alpha\beta} g_{\alpha\beta}\nu_\alpha\nu_\beta \\ &= \phi \sum_{\alpha\beta ij} g_{\alpha\beta}U_{\alpha i}U_{\beta j}\nu_i\nu_j. \end{aligned} \tag{4.29}$$

The identification of $g_{ij} = \sum_{\alpha\beta} U_{i\alpha}U_{j\beta}g_{\alpha\beta}$ allows us to use Eq. (4.21). We reparametrize the scattering rate

$$\Gamma_R^{jkil} = \sum_{\alpha\beta\gamma\delta} |U_{\gamma i}|^2|U_{\alpha j}|^2|U_{\delta l}|^2\Gamma_R^{k,\alpha\beta\gamma\delta}, \tag{4.30}$$

with $\Gamma_R^{k,\alpha\beta\gamma\delta} = |U_{\beta k}|^2 n_k(t)\sigma_R^{\alpha\beta\gamma\delta}c$ and $\sigma_R^{\alpha\beta\gamma\delta} = |g_{\alpha\beta}|^2|g_{\gamma\delta}|^2/[4(m_\phi c^2)\Gamma_\phi]$. We choose such a reparametrization in order to separate the neutrino conversion probabil-

ities from the scattering cross subsections. In doing so, and invoking unitarity, we obtain the result

$$\begin{aligned}
\Phi_i(t,E) &= \int_{-\infty}^{t} dt' [a(t)/a(t')] e^{-\tau_i(t',t,E)} \widetilde{S}_i\{t', [a(t)/a(t')E]\}, \\
\widetilde{S}_i(t,E) &= S_i(t,E) + \sum_{\gamma\delta} |U_{\gamma i}|^2 \left(1 + |U_{\delta i}|^2\right) \\
&\qquad \times \sum_{\alpha\beta k} \Gamma_R^{k,\alpha\beta\gamma\delta}(t) \Phi_\alpha(t, E_k) \Theta(E_k - E), \\
\Phi_i(t,E_j) &= \frac{H(t)}{\Gamma_R^{ij}(t)} \int_{-\infty}^{t} dt' \frac{a(t)}{a(t')} \left[e^{-\tau_i(t',t,E_j^+)} - e^{-\tau_i(t',t,E_j^-)} \right] \\
&\qquad \times \widetilde{S}_i\{t', [a(t)/a(t')]E_j\},
\end{aligned} \tag{4.31}$$

with $\Gamma_R^{ij}(t) = \sum_\alpha |U_{\alpha i}|^2 \left(\sum_{\beta\gamma\delta} \Gamma_R^{j,\alpha\beta\gamma\delta} \right)$. While we have presented here these equations in the flavor basis for analytic insight, we note that in general it is easier numerically to use Eq. (4.21) with the appropriate substitution, as it contains fewer summations.

However, for a single-flavor α interaction, where the flavor self-coupling

matrix is $g_{\mu\nu} = g\delta_{\mu\alpha}\delta_{\nu\alpha}$, there is a decidedly simpler form in the flavor basis,

$$\begin{aligned}
\Phi_i(t,E) &= \int_{-\infty}^{t} dt'[a(t)/a(t')]e^{-\tau_i(t',t,E)}\widetilde{S}_i\{t',[a(t)/a(t')E]\},\\
\widetilde{S}_i(t,E) &= S_i(t,E) + |U_{\alpha i}|^2\left(1+|U_{\alpha i}|^2\right)\\
&\qquad\qquad \times\sum_k \Gamma_R^{k,\alpha}(t)\Phi_\alpha(t,E_k)\Theta(E_k-E),\\
\Phi_\alpha(t,E_j) &= \frac{H(t)}{\Gamma_R^{j,\alpha}(t)}\int_{-\infty}^{t} dt'\frac{a(t)}{a(t')}\left[e^{-\tau_i(t',t,E_j^+)} - e^{-\tau_i(t',t,E_j^-)}\right]\\
&\qquad\qquad \times\widetilde{S}_i\{t',[a(t)/a(t')]E_j\},
\end{aligned} \tag{4.32}$$

with $\Gamma_R^{j,\alpha}(t) = |U_{\alpha k}|^2 n_k(t)\sigma_R c$ and $\sigma_R = (\hbar c)^2\pi g^2/(m_\phi c^2)^2$.

4.2 Neutrinos and AGN

High-energy astrophysical neutrinos (HEANs) comprise a diffuse isotropic extragalactic background of neutrinos observed with energies between a few TeV to a few PeV [1, 183–185]. There is some evidence of an association of some these neutrinos with the blazar TXS 0506+056 [186, 187], but the source of the vast majority of the HEAN background remains a mystery. Various classes of bright AGN population have been constrained to contribute no more than a fraction of the total observed HEAN flux [188–193], but there is little known about the possible contribution of the many lower-luminosity AGN. With the advent of the Vera Rubin Observatory in 2024, at least 10 million AGN will be

observed in the southern sky with high cadence for the following 10 years [109]. In addition, neutrino telescopes KM3NeT and Baikal-GVD will soon be completed in the northern hemisphere with comparable volume and better angular resolution than IceCube [194, 195]. Due to their locations, these telescopes will detect HEAN from upgoing tracks originating from the southern sky without contamination from the atmospheric neutrino background. Thus, over the next decade of AGN and neutrino observations, we expect a large increase in sensitivity in the determination of AGN as HEAN emitters.

AGN are hypothesized to emit high-energy neutrinos through either hadronuclear [196,197] or photohadronic [198,199] processes. Therefore, one avenue of examination is the modelling of these processes under various AGN environments. High-energy neutrinos can be produced from radio-quiet AGN [200–202], radio-loud AGN jets [203–205], blazar inner cores and jets [190, 206], and AGN coronae [207–210]. They may also have nothing to do with AGN—e.g., they may be associated with choked supernova jets [211], tidal disruption events [212–215] and even cosmic strings [2,216]. Even without theoretical modeling, information about the source of neutrinos may be sought with the coincidence of neutrino events with various source events through data alone [192, 193, 217–226].

In this work we present a statistical framework to determine whether HEANs are produced by AGN and assess its potential in the context of Rubin, IceCube,

KM3NeT, and Baikal-GVD. More specifically, we propose to cross-correlate temporal and spatial data from AGN variability and neutrino events. To evaluate the prospects to detect such a cross-correlation, we make the simplest assumption that the neutrino flux from any given AGN at any given time is proportional to the electromagnetic flux at that given time. We then use state-of-the-art information on the AGN redshift/luminosity distribution and variability parameters to forecast the detectability of this cross-correlation. We find, with the AGN population assumed, that a correlation can be established even if the AGN in Rubin contribute as little as a few percent to the HEAN flux. Most of the sensitivity comes from angular information; the temporal information contributes approximately 10% of the signal to noise. Our estimates suggest that the better angular resolution ($\sim 0.2^\circ$) expected for Baikal-GVD and KM3NeT, relative to the $\sim 0.5^\circ$ for IceCube, will give them roughly twice the sensitivity to an AGN-neutrino cross-correlation for equal exposure.

This work is organized as follows. In Sec. 4.2.1 we present the formalism of the AGN/neutrino cross-correlation. We discuss our model for the AGN redshift/luminosity distribution and the variability properties of AGN in Sec. 4.2.2. We provide and discuss numerical results in Sec. 4.2.3. We discuss these results and conclude in Secs. 4.2.4 and 4.2.5, respectively.

4.2.1 Formalism

Our aim will be to determine the fraction f of neutrinos that come from AGN in the sample under the hypothesis that the neutrino flux from any given AGN at any given time is proportional to the electromagnetic flux from that AGN at that given time. To begin, we will simplify by neglecting AGN variability and then generalize later.

4.2.1.1 Angular information only

The optimal estimator to determine the fraction f of neutrinos that come from AGN in the sample will be the unbinned maximum-likelihood estimator [193, 227–230],

$$\mathcal{L}(f;\mathrm{data}) = \Pi_i \left[f S_i + (1-f) B_i \right], \tag{4.33}$$

where the product is over all neutrino events. Here, $S_i = S(\vec{\theta}_i) d^2\vec{\theta}$ is the probability that a given source neutrino will be found in a differential area $d^2\theta$ centered at the position θ_i of the ith neutrino, and $B_i = B(\vec{\theta}_i) d^2\theta_i$ the analogous quantity for a background neutrino. We normalize both distributions such that their integral over the area $4\pi f_{\mathrm{sky}}$ of the survey (where f_{sky} is the fraction of the sky surveyed) is equal to 1. We assume that background events follow a uniform sky distribution, i.e., $B_i = (4\pi f_{\mathrm{sky}})^{-1}$, which we justify in Sec. 4.2.6.

Finally, we take the signal probability to be

$$S_i = \sum_\alpha w_\alpha \frac{1}{2\pi\sigma^2} \exp\left(-\frac{(\vec{\theta}_i - \vec{\theta}_\alpha)^2}{2\sigma^2}\right). \tag{4.34}$$

The sum on α is over all AGN in the sample; $\vec{\theta}_\alpha$ is the position of the αth AGN; and σ is the error in the neutrino angular position. Here, w_α is the probability that a given signal neutrino comes from the αth AGN, and so $\sum_\alpha w_\alpha = 1$.

Even if there is no signal, the likelihood will most generally be maximized at a value of f selected from a distribution with a variance σ_f^2 determined from

$$\frac{1}{\sigma_f^2} = \left\langle \left(\frac{\partial \ln \mathcal{L}(f;\mathrm{data})}{\partial f}\right)^2 \right\rangle, \tag{4.35}$$

where the derivative is evaluated at $f = 0$, and the average is taken over all realizations of the data under the null hypothesis. We use

$$\left(\frac{\partial \ln \mathcal{L}}{\partial f}\right)_{f=0} = \sum_i \left(\frac{S_i}{B} - 1\right). \tag{4.36}$$

We then evaluate the expectation value

$$\left\langle \left(\frac{S}{B} - 1\right)^2 \right\rangle = \frac{4\, f_{\mathrm{sky}}}{\sigma^2\, N_{\mathrm{AGN}}} \frac{\langle w_\alpha^2 \rangle}{\langle w_\alpha \rangle^2} \tag{4.37}$$

from the zero-lag correlation function for a collection of N_{AGN} randomly dis-

tributed AGN. Here, the angle brackets denote an average over all AGN in the sample. Our hypothesis here is that the neutrino flux from AGN α is proportional to its electromagnetic F_α, and so the correlation of N_ν neutrinos with AGN can be established with a signal-to-noise,

$$\frac{S}{N} \simeq 2\frac{f}{\sigma}\sqrt{\frac{N_\nu}{N_{\rm AGN}}\frac{\langle F_\alpha^2\rangle}{\langle F_\alpha\rangle^2}f_{\rm sky}}. \tag{4.38}$$

The result has the expected scalings with $f_{\rm sky}$, σ, N_ν, and $N_{\rm AGN}$. That is, Eq. (4.38) depends on the ratio of the number of neutrinos to the number of AGN in a neutrino's angular resolution bin $N_{\rm AGN}[(\pi\sigma^2)/(4\pi f_{\rm sky})]$. If this ratio is small, one neutrino spatially overlaps with so many AGN that it is hard to detect a signal even when all neutrinos are taken into account. The signal to noise is also weighted by the ratio $\langle F_\alpha^2\rangle$ / $\langle F_\alpha\rangle^2$ of the second moment of the AGN flux distribution to the square of the first moment (i.e., average flux).

4.2.1.2 Including AGN variability

The derivation above can be easily generalized to include the additional information provided by cross-correlating the neutrino arrival times with AGN luminosity at any given time. If the neutrino luminosity at any given time is correlated with the AGN luminosity at that same time, then the probability to detect a neutrino when a given AGN is, say, twice as bright, should be twice as

large, as illustrated in Fig. 4.10.

To incorporate this correlation into the likelihood analysis above, we simply assume that the flux F_α for any given AGN in the likelihood function is the apparent flux *at the neutrino arrival time*. The signal-to-noise contributed by each AGN is then enhanced by a factor,

$$\left[\frac{\langle F^2(t)\rangle}{\langle F(t)\rangle^2}\right]^{1/2}, \tag{4.39}$$

where here $\langle F(t)\rangle$ is the time-averaged flux and $\langle F^2(t)\rangle$ the time-averaged squared flux. Thus, for example, if an AGN has a sinusoidal flux variation, $F(t) = F_0 + F_1\cos\omega t$, the contribution of this AGN to the total signal-to-noise is enhanced by a factor $[1 + (F_1/F_0)/2]^{1/2}$.

Of course, AGN variability is complicated and poorly understood. Below we describe a model for AGN variability but here note that the signal-to-noise with which f can be inferred will be enhanced by a factor $[1+\langle\sigma^2_{\rm var}\rangle\,/2]^{1/2}$, where $\langle\sigma^2_{\rm var}\rangle$ is an appropriately weight rms fractional flux variation.

4.2.2 The AGN Population

4.2.2.1 The flux distribution

Here we model the flux distribution we expect for AGN in Rubin. Let $dN_{\rm AGN}/dzdL$ be the redshift and bolometric luminosity distribution of AGN. Then AGN are distributed throughout the Universe according to

$$\frac{dN_{\rm AGN}(z,L)}{dzdL} = \frac{dV(z)}{dz}\frac{dn(z,L)}{dL}, \tag{4.40}$$

with $dn(z,L)/dL$ the AGN luminosity function, $dV(z)/dz = 4\pi f_{\rm sky} r(z)^2 dr(z)/dz$ the comoving volume observed over a fraction $f_{\rm sky}$ of the sky, $r(z) = \int_0^z |dr/dz| dz$ the comoving radial distance to a redshift z, $dr/dz = -c/(1+z)H(z)$ its redshift derivative, c the speed of light, and $H^2(z) = H_0^2\left[\Omega_m(1+z)^3 + (1-\Omega_m)\right]^{-1/2}$ the Hubble parameter. We use Planck 2018 ΛCDM parameters $H_0 = 2.18\times10^{-18}{\rm s}^{-1}$ and $\Omega_m = 0.315$ [73], along with the Full AGN luminosity function in Table 3 from Ref. [133].

However, given a cosmological distribution of AGN, only those that appear bright enough will be observed. More specifically, given a limiting apparent magnitude $m_{\rm lim}$, the distribution of observed AGN in that band is

$$\frac{dN_{\rm AGN}}{dzdm} = \Theta(m_{\rm lim} - m)\frac{dL_{\rm bol}}{dm}\frac{dN_{\rm AGN}[z, L_{\rm bol}(z,m_b)]}{dzdL_{\rm bol}}, \tag{4.41}$$

with $\Theta(x)$ the Heaviside theta function, $L_{\rm bol}(z,m) = K_o(m) 4\pi d_L(z)^2 \langle \delta\nu_b \rangle F_{\rm AB} 10^{-(2/5)m_b}$ the bolometric luminosity for an AGN with apparent magnitude m averaged over frequency bands b located at redshift z, and $dL_{\rm bol}/dm = -(2/5)\log(10) L_{\rm bol}(m,z)$ its apparent magnitude derivative. Furthermore, $K_o(m)$ is the bolometric correction function to convert from the emitted luminosity in the optical band to the bolometric luminosity of the source, $d_L(z) = (1+z)r(z)$ the luminosity distance, $\delta\nu_b$ the frequency bandwidth of band b, and $F_{\rm AB} = 3.631 \times 10^{-23}$ W Hz^{-1} m^{-2}. Moreover, we assume that the observed intensity is roughly constant across the entire frequency bandwidth, and that any redshifting effects on the frequency do not alter the intensity in each band significantly. While the bolometric correction is typically a function of the apparent magnitude, it only varies up to 20% within the optical band across the magnitudes considered. Thus, for simplicity, we adopt that $K_o(m) = 10$ for all magnitudes and bands [133].

We define $dF_{\rm AGN}/dzdL$ to be the AGN flux luminosity distribution, and $dF^b_{\rm AGN}/dzdm \equiv FdN^b_{\rm AGN}/dzdm$ its magnitude counterpart. We plot the flux luminosity distribution in Fig. 4.7 and the magnitude distribution in Fig. 4.8.

In Fig 4.9 we plot the bolometric-luminosity distribution of AGN in the forecast Rubin sample and also the bolometric-luminosity weighted by the luminosity—this latter quantity is then proportional to the probability, under our assumptions, that a given neutrino comes from an AGN of some given luminosity.

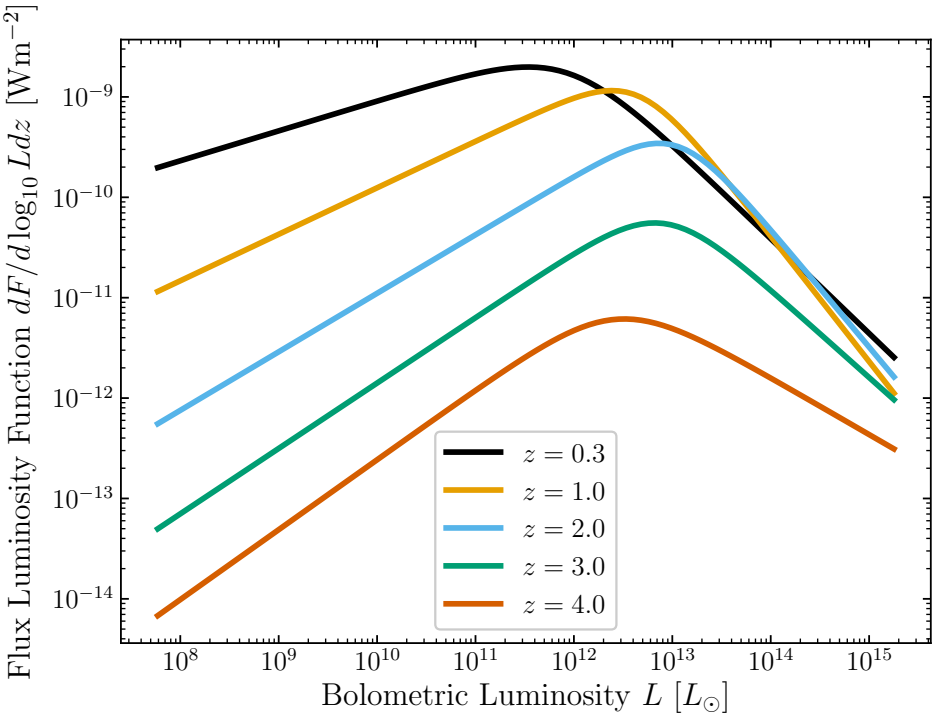

Figure 4.7: The flux distribution of AGN as a function of an AGN's bolometric luminosity at redshifts $z \in \{0.3, 1.0, 2.0, 3.0, 4.0\}$, as given by Eq. (4.40).

.

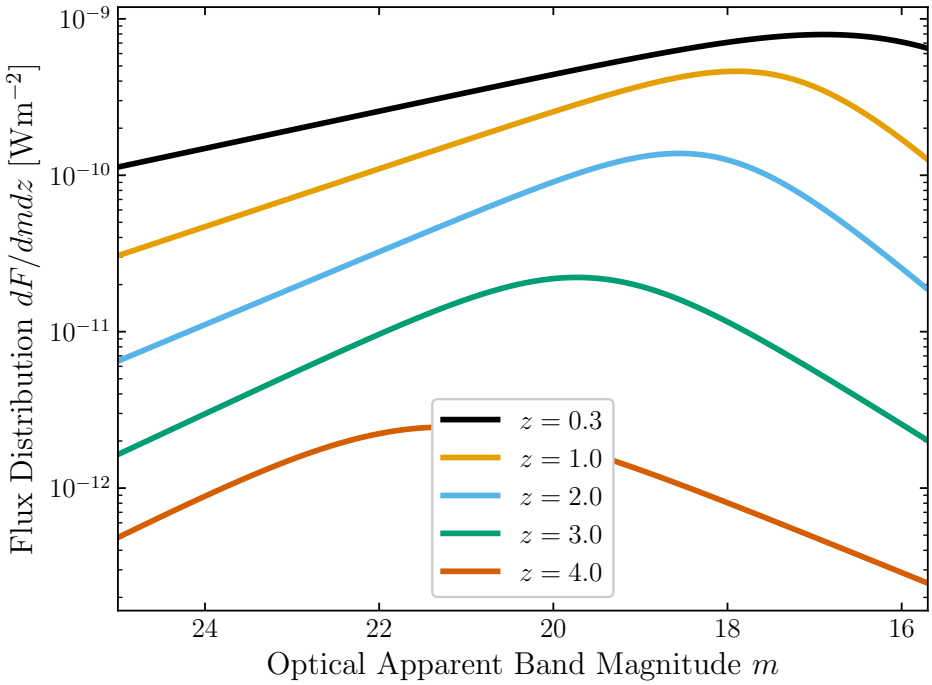

Figure 4.8: The flux distribution of AGN as a function of an AGN's apparent magnitude in an optical band b at redshifts $z \in \{0.3, 1.0, 2.0, 3.0, 4.0\}$, as given by Eq. (4.41). In order to show the full range of this distribution, we do not include the theta function factor.

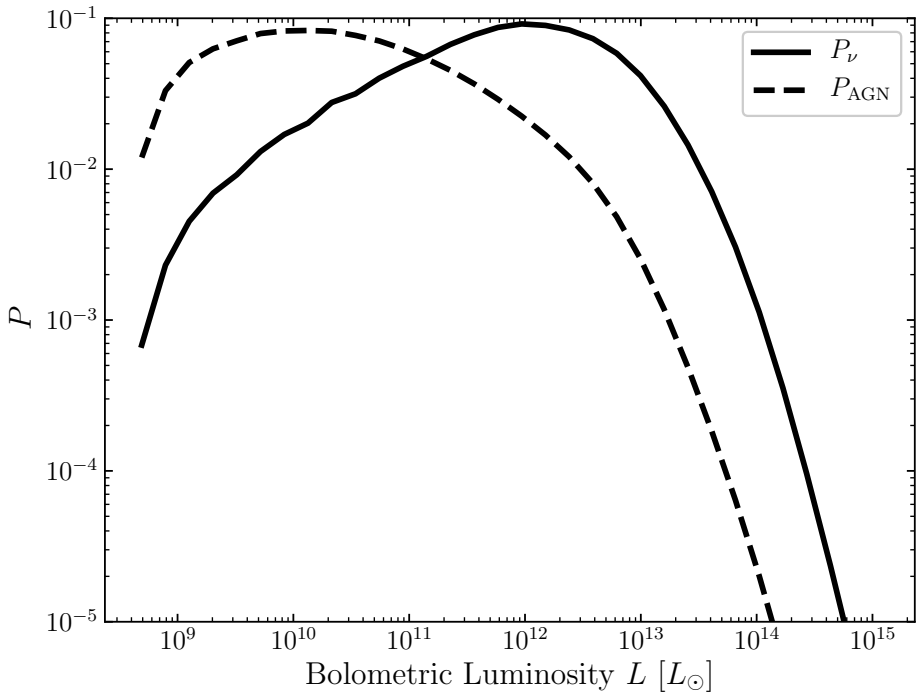

Figure 4.9: The observation probability P associated with neutrinos and AGN in each bolometric luminosity bin between redshifts $0.3 \leq z \leq 6.7$. Over the range of luminosities presented, 33 base-10 logarithmic bins are taken. The solid black line is the probability that an AGN emitting neutrinos has bolometric luminosity L, while the dashed black line is the probability of that an observed AGN has bolometric luminosity L. Both curves are normalized by the set of observed AGN and are computed assuming a limiting magnitude of $m_{\rm lim} = 24.0$. At large luminosities both curves follow the expected flux distribution curve of Fig. 4.7, however at small L the limiting magnitude restricts the total number of AGN observed.

4.2.2.2 AGN Variability

The study of AGN variability is in its infancy when compared to how it will appear in the Rubin era [231]. We thus have far less in the way of precise current knowledge to make forecasts for the possibility to detect the cross-correlation between AGN variability and neutrino arrival times. To do so, though, we assume AGN light curves undergo a damped random walk [120–124, 128–131], a model that provides a reasonable description of most light curves. In this case, the intensity $I_\alpha(t)$ of AGN α undergoes fluctuations described by a stationary random process with two-point correlation function, $\langle I_\alpha(t+t')I_\alpha(t)\rangle = A_\alpha^2 e^{-t/\bar{t}_\alpha}$, or equivalently, a power spectrum $P_\alpha(\omega) = 2A_\alpha^2\bar{t}_\alpha/[1+(\omega\bar{t}_\alpha)^2]$. We assume that AGN all have the same variability amplitude $A_\alpha = 1$ and an observer-frame variability timescale $\bar{t}_\alpha = \bar{t}_0(1+z)(L/L_b)^\beta$ for an AGN of luminosity L at redshift z, as suggested by recent measurements [131]. We take $\bar{t}_0 = 1$ month, $L_b = 2\times10^{35}$ W, and $\beta = 0.23$. Our calculation then discards Fourier modes with periods longer or shorter than those accessed by Rubin.

Given this population of AGN, we can write the fractional flux variation as

$$\sigma^2_{\rm var} = \frac{1}{\pi}\frac{1}{\langle F_\alpha^2\rangle}\int_{\omega_{\rm min}}^{\omega_{\rm max}} d\omega\,\left\langle F_\alpha^2 P_\alpha(\omega)\right\rangle, \tag{4.42}$$

where only modes between $\omega_{\rm min} = 2\pi/T$ and $\omega_{\rm max} = 2\pi/\Delta t$ are included, with $\Delta t = 3.5$ days the temporal resolution of the experiment and $T = 10$ years the

duration of the observation.

4.2.3 Forecasts

We now forecast the ability of the neutrino telescopes IceCube, KM3NeT, and Baikal-GVD, along with optical telescope Rubin, to determine the fraction f of neutrinos that come from AGN in the survey.

4.2.3.1 Angular information only

With our model for the AGN luminosity/redshift distribution and Rubin's apparent-magnitude cutoff, we forecast $N_{\rm AGN} \simeq 2.8 \times 10^7$ AGN in the survey and $\langle F_\alpha^2 \rangle \,/\, \langle F_\alpha \rangle^2 \simeq 15$. We then find from Eq. (4.38),

$$\frac{S}{N} \simeq 5.7\, f \left(\frac{(N_\nu/10^4)}{(\sigma/0.5^\circ)(N_{\rm AGN}/2.8\times 10^7)} \right)^{1/2} \times \left(\frac{\langle F_\alpha^2 \rangle \,/\, \langle F_\alpha \rangle^2}{15} \right)^{1/2} \left(\frac{f_{\rm sky}}{0.5} \right)^{1/2} . \tag{4.43}$$

4.2.3.2 Angular information and timing

With our models for AGN variability and the AGN luminosity/redshift distribution, we infer an rms fractional flux variation of $\langle \sigma_{\rm var}^2 \rangle \simeq 0.54$. The estimate in Eq. (4.43) is thus enhanced by approximately 12%.

This calculation can also be understood in a different way. It suggests that

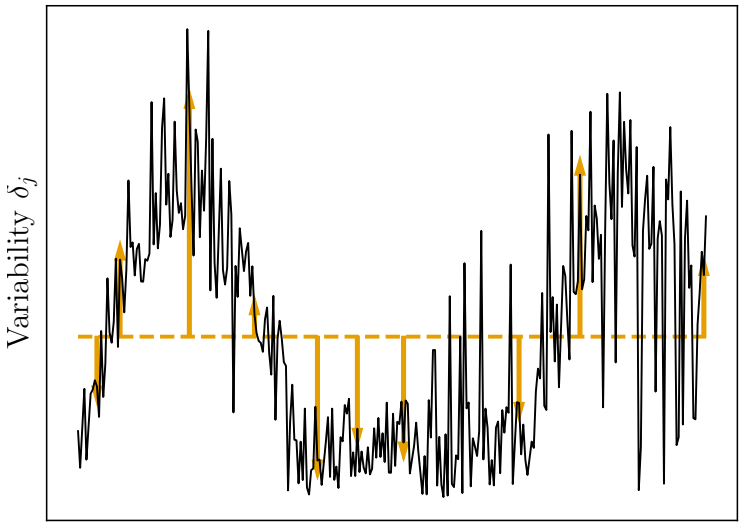

(a)

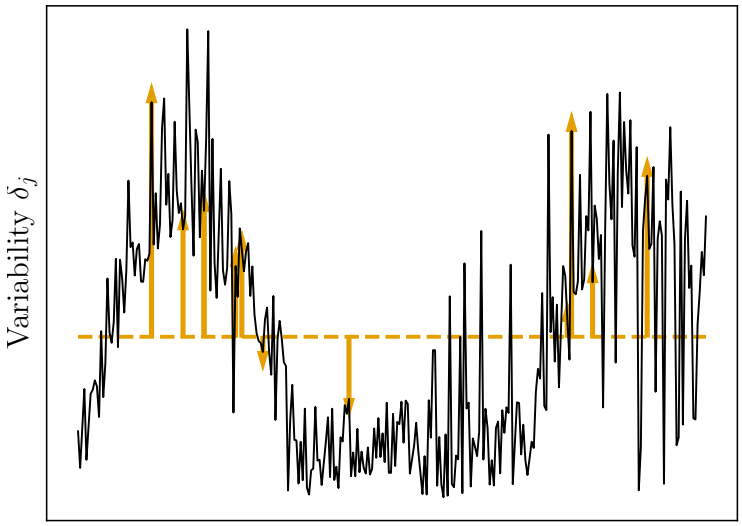

(b)

Figure 4.10: An example of the variability $\delta_j(t)$ of AGN j shown in solid black, plotted against the variability $\delta_j(t_\alpha)$ evaluated at the neutrino arrival times t_α, depicted by solid orange arrows. The dashed orange line indicates the zero point, $\delta_j = 0$. In the top figure the neutrinos arrive randomly, and thus a cross correlation between these two quantities would become zero. In the bottom figure the neutrinos are sourced from AGN and thus are biased towards appearing when the intensity is higher, leading to nonzero correlation.

if AGN are determined from angular information to contribute a fraction f of the observed neutrinos, then a correspondence between instantaneous AGN luminosity and neutrino luminosity can be established with a signal-to-noise of $\left[\langle\sigma^2_{\rm var}\rangle\,/2\right]^{1/2}$ times the value in Eq. (4.43).

4.2.3.3 IceCube, KM3NET, and Baikal-GVD

We now present numerical results including the sky-averaged effective areas for IceCube, KM3NET, and Baikal-GVD for the regions of sky that overlap with those surveyed by Rubin—to a first approximation, though, they are all comparable. We take the angular resolution of IceCube to be 0.5° and those for KM3NET and Baikal-GVD to be 0.2°. The total exposure time is taken to be 10 years. We plot the SNR from angular information alone, from timing, and from the total, in Fig. 4.11. The green curve there shows the signal-to-noise for a measurement where f is inferred only from a correlation of the neutrino arrival time with AGN variability, assuming our canonical value for $\langle F^2\rangle\,/\,\langle F\rangle^2$.

4.2.4 Discussion

We clarify four assumptions and present three comments. First, our main assumption is linearity between neutrino number and AGN bolometric luminosity. Even if linearity holds true, various AGN may have different proportionality constants due to some additional specification of AGN class (e.g. this

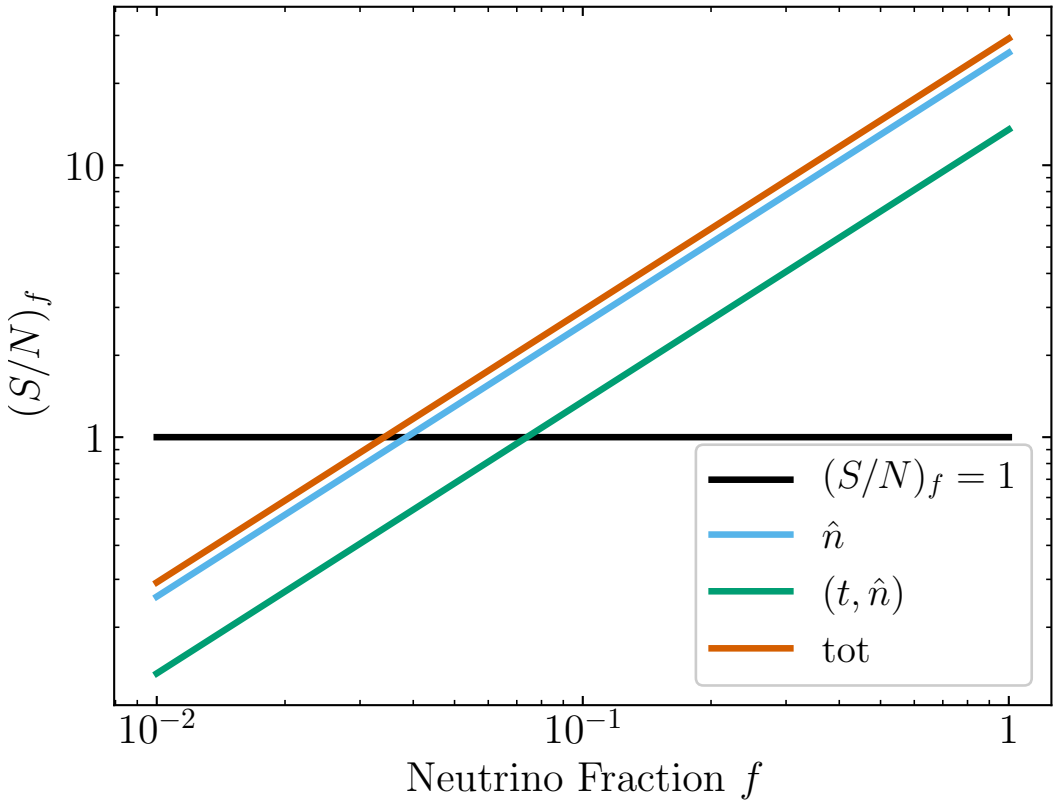

Figure 4.11: The signal-to-noise ratio $(S/N)_f$ for measuring the HEAN neutrino fraction f using both temporal and spatial data from Rubin's i band, IceCube, KM3NeT, and Baikal-GVD. Since pure spatial correlation dominates the SNR, the result is not very sensitive to the underlying AGN variability parameters. IceCube contributes $\sim 8\%$ of the total SNR, while KM3NeT and Baikal-GVD each give $\sim 46\%$.

scenario already occurs with redshift). This will then be encoded in a change to $\langle F^2 \rangle / \langle F \rangle^2$. Additional classes in the variability properties will change the value of $\langle \sigma^2_{\rm var} \rangle$ relative to the value obtained in our canonical model. It is also possible that the number of neutrinos is not linear in the AGN's bolometric luminosity, but some power γ, with $0 \leq \gamma \leq 2$ [191]. We leave the investigation of both these cases for future work.

Second, we chose a specific form (the damped random walk) for the intensity autocorrelation function for AGN. This form, while applicable to a majority of AGN, has some exceptions. Changes in the slope, break, as well as additional slopes and breaks, are all required to encapsulate a greater range of AGN morphologies. However, for our forecast analysis, such changes will only result in a rescaling of the scaled variance $\langle F^2 \rangle / \langle F \rangle^2$. In particular, if the change in the variability properties shifts the variability timescales outside of the measurable window allowed by the Rubin cadence, then the prospects to detect a neutrino-AGN temporal correlation will decrease, while if more power is concentrated in this window, they may become stronger.

Third, we set the time delay between the neutrino signal and AGN variability to zero. This was done for simplicity, and in reality there should be an expected delay depending on where within the AGN the neutrino was created and where the variability is sourced. We leave formalizing this description for future work.

Fourth, we assumed that neutrinos travel along the line of sight unimpeded. The presence of neutrino self-interactions [232] can change this description, altering the spatial and temporal coincidence presented here [233, 234]. We also leave exploration of this scenario for future work.

In our analysis, we consider cross-correlating the entire Rubin catalog with several high-energy neutrino maps. Cross-correlating only a sub-population of the Rubin catalog, instead, could yield a higher signal-to-noise, as given by our estimation in Eq. 4.38. If possible, certain sub-populations would then be able to be detected or ruled out as definitive sources at higher significance. It is worth noting, however, that for a given source model of high-energy neutrino production the expected signal also decreases with a smaller sub-population (if that smaller population removes sources in the model of interest). Therefore, reducing the number of AGN in a cross-correlation study will not always yield more promising results. Regardless, we have shown here that, even without maximizing the signal-to-noise for a given source model, future AGN/neutrino cross-correlations will still be able to detect signals even if the Rubin catalog only contributes to a tenth of the entire HEAN flux.

Measurements of the neutrino fraction f have covariance with measurements of AGN variability parameters. Therefore, in principle the error in measurements of f should be larger than that presented here. However, given Rubin's precise measurements of an AGN's variability parameters, we expect

such degradation of measurement fidelity to be slight and our forecast to hold.

Finally, we choose to neglect energy dependence in our analysis in order to obtain conservative sensitivity estimates that are model-independent. In general, it is expected that sources with a harder spectrum are easier to detect, and prior work shows that inclusion of such model-dependency improves the sensitivity by a factor of ~ 2 (depending on the source spectrum assumed) [229]. We expect that most of the AGN that will be detected by Rubin will be radio-quiet.

4.2.5 Conclusion

In this work, we investigated the prospects to detect an angular cross-correlation between AGN surveyed by Rubin and energetic neutrinos. We then discussed further the prospects to detect a cross-correlation between AGN variability and neutrino arrival times.

With this aim, we first modelled the spatial cross-correlation between a single AGN and a population of neutrinos and found a neutrino-counting measure. More specifically, the contributions to this correlation were from counting neutrinos sourced by that AGN and from counting neutrinos with other sources that have nonzero overlap with that AGN due to angular error.

AGN may emit electromagnetic radiation along with HEANs, and to account for this possibility, we also modelled a temporal-and-spatial cross-correlation.

For simplicity, we assumed that, for each AGN, the number of neutrinos emitted is proportional to the electromagnetic intensity of that AGN.

Using both of these correlations, we then forecasted their individual and total abilities to measure the fraction f of HEAN from Rubin-observed AGN. The HEANs are detected by a combination of IceCube, KM3NeT, and Bakail-GVD, and we assumed an IceCube-like sky-averaged effective area for each experiment. In accordance with previous work, we took all AGN in the Rubin sample to be measured with high signal-to-noise. We thus found that, given 10 years of observation time, temporal and spatial cross-correlations will be able to establish an association between energetic neutrinos and the AGN in Rubin even if such AGN contribute only $\sim 10\%$ of the neutrino background. Finally, given that the background noise scales with $N_{\rm AGN}^{-1/2}$, it should be possible to establish a correlation between neutrinos and some specific subclass of AGN, even if those AGN contribute less than $\sim 10\%$ of the neutrino background.

4.2.6 Assumption of uniform background

In this subsection, we justify that the assumption of uniform distribution for the background events (i.e., $B_i = (4\pi f_{\rm sky})^{-1}$) does not affect our forecasted sensitivity.

We simulate 5000 sources with their sky locations drawn from a uniform distribution on a 2D sphere. Then, following the procedures in Ref. [193],

we calculate the limit/sensitivity that can be set by evaluating the maximum-likelihood estimator (Eq. (4.33)). The limit is calculated for two different cases. First is using IceCube's 10 years of data (track events) and the realistic background PDFs which are derived from the data [193]. The second is using the simulated data which consists of the same number of track events with arrival directions drawn from uniform distributions of right ascension and $\cos(\text{zenith angle})$ and the corresponding background PDF, $B_i = (4\pi f_{\text{sky}})^{-1}$. The 95% limit (sensitivity) is set by a deviation of $\ln \mathcal{L}$ from when $f = 0$ by 3.84, i.e., $\Delta \ln \mathcal{L} = -3.84$. Note that $f = 0$ means all the events come from the background.

Figure 4.12 shows the result. The likelihood curves are close for the two cases and the 95% upper limits on n_s are within a factor of two, where $n_s = f \times N_\nu$ is the total number of neutrinos coming from the sources.

4.3 Cosmic Strings

IceCube routinely detects high-energy astrophysical neutrinos (HEANs) with TeV-PeV energies that follow a power law flux spectrum with spectral index $\gamma = 2.53$ [235]. Explanations for the source of this flux have ranged from gamma-ray bursts [236–242], FR0 quasars [205], blazars [191,243,244], radio-bright AGN [193,224,245], choked jet supernovae [213,214], pulsar wind neb-

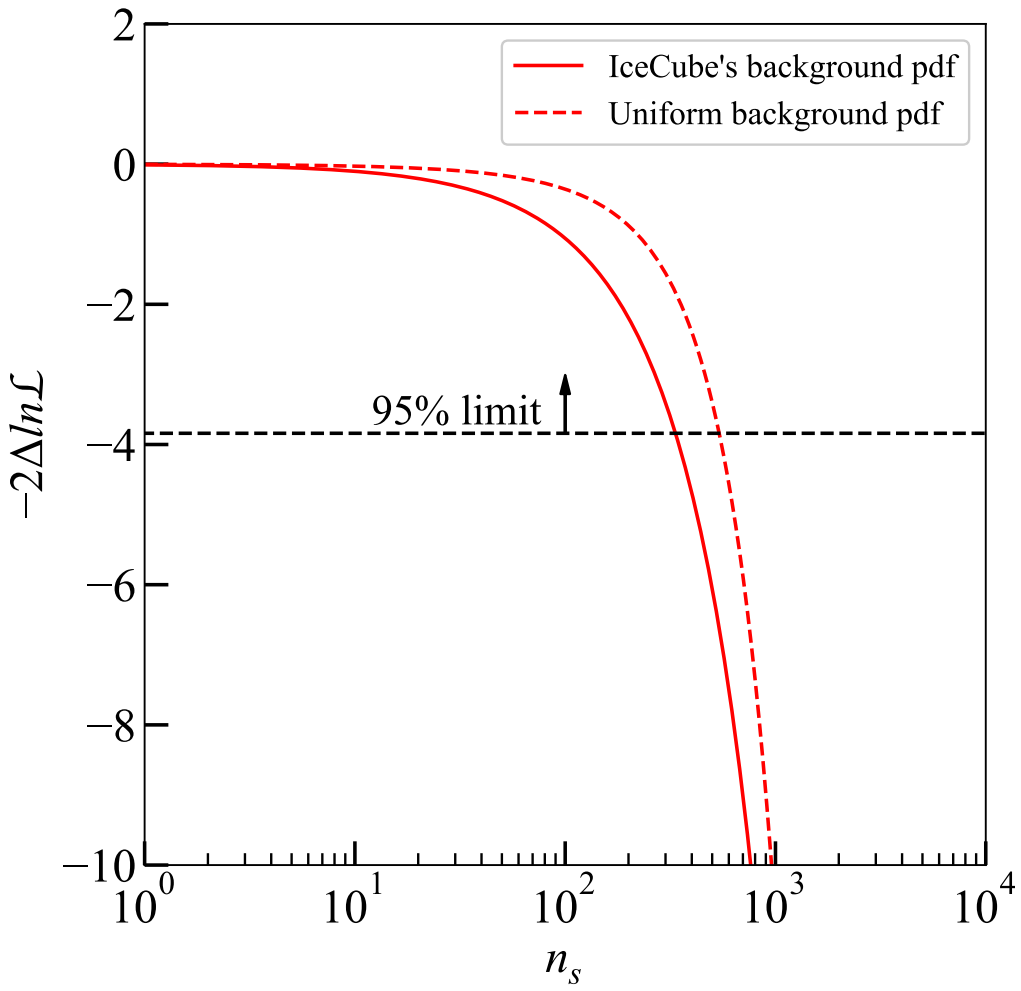

Figure 4.12: Forecasted sensitivities to a catalog of simulated 5000 source from numerical calculations of the maximum-likelihood estimator (Eq. (4.33)). Solid line uses IceCube's 10 years of data and the corresponding background PDF. Dashed line uses the same number of simulated events with arrival directions drawn from uniform distributions of right ascension and $\cos(\text{zenith angle})$ and the corresponding background PDF, $B_i = (4\pi f_{\text{sky}})^{-1}$.

ulae [246], and more. However, none of these propositions have been succesful at explaining the majority of the observed spectrum [247]. One additional possibility is that cosmic string loops source these neutrinos. More concretely,

the actual mechanism of emission could be due to the radiation of particles from string features, known as quasi-cusps, -kinks, or kink-kink collisions, that generically occur during the evolution of cosmic string loops. These particles could either be the neutrinos themselves (direct neutrino emission) or a parent particle which then decays into neutrinos (indirect neutrino emission).

The emission of neutrinos due to the decay of a real scalar radiated from cusps and kinks has previously been considered in the ultra-high energy range [2, 216]. Moreover, the energy spectrum of various Standard Model (SM) particles near the string has been extensively computed in the context of dark strings coupling through Higgs portal operator [248–250]. More generally, the program of calculating emission from cosmic strings also includes the radiation of gravitational waves, cosmic rays, and more [251–256].

In this work we extend and refine these calculations in several manners. First, we calculate the optical depth of HEANs using all seven channels of Standard Model neutrino self-interactions and thus including the energy dependence of the neutrino horizon. Then, we perform this calculation for all three types of string features: quasi-cusps, -kinks, and kink-kink collisions. Prior work has only considered the first two in the scenario of neutrino emission. In addition, we calculate the emission from a real scalar not only in the scenario of a cascade of particles, but also the direct decay into neutrinos. Moreover, we present the first calculation for the emission of neutrinos directly

from cosmic strings via a 2-body decay interaction and the Aharonov-Bohm coupling. Finally, we incorporate the shrinking of loops due to particle radiation into the loop distribution function, a factor ignored in earlier neutrino emission papers. Using these calculations, we present the viable parameter space for neutrino emission for each of the models chosen. Moreover, we find that for these models, cosmic strings can only contribute at most around 45% of the observed HEAN flux. Since the models represent a wide selection of possible emission mechanisms, we conclude it is unlikely that a single population of cosmic strings can create the entirety of the HEAN background. However, as a subdominant component, cosmic strings may still contribute enough to create a bump in the spectrum.

This work is organized as follows. In Sec. 4.4 we present the general formalism in order to calculate the differential flux of neutrinos observed at IceCube from an arbitrary source and then particularize to the case of a cosmic string loop population. For this population, we introduce four interaction terms between cosmic strings and neutrinos using an effective field theory approach in Sec. 4.5. These interactions cover both direct and indirect neutrino emission, each of which is split into two further cases. We use these interaction terms to then calculate the energy spectrum of neutrinos emitted at the locality of the string in Sec. 4.6. We follow up this calculation and then specify the form of the cosmic string loop number density in Sec. 4.7. Ultimately, we combine both

the energy spectrum of neutrinos with the cosmic string loop number density to calculate the observed differential flux of neutrinos through the formalism presented in the beginning, shown in Eq. (4.80). Using this flux, we constrain both the fraction of neutrinos attributed to emission from cosmic strings in the IceCube spectrum and the phenomenological parameter space for neutrino emission in Sec. 4.8. We discuss and conclude in Sec. 4.9 and 4.10.

4.4 Neutrino Specific Flux

The specific flux $\Phi_i(t, E)$ of neutrinos ν_i (number of astrophysical neutrinos per unit conformal time per unit comoving area per unit energy) at cosmic time t and observed energy E from a source S_i is [232]

$$\Phi_i(t, E) = \int_{-\infty}^{t} dt' [a(t)/a(t')] e^{-\tau_i(t', t, E)} S_i\{t', [a(t)/a(t')E\}, \tag{4.44}$$

where $a(t)$ is the scale factor and $\tau_i(t', t, E)$ is the optical depth of a neutrino ν_i of energy E between times t' and t.

For a single cosmic string loop, the spectrum of emitted neutrinos is a function of the loop length L, and so the source function is the integral over all loop

contributions,

$$S^e_{i,a}(t,E) = \sum_a c \int_0^\infty dL \frac{d\dot{N}^e_{i,a}(t,L,E)}{dN_{\rm loop} dE} \frac{dn_{\rm loop}(t,L)}{dL}, \tag{4.45}$$

with $dn_{\rm loop}(t,L)/dL$ the number of cosmic string loops per comoving volume per loop length, and $d\dot{N}^e_{i,a}/dN_{\rm loop}dE$ the number of neutrinos ultimately produced from string feature a and emission model e per unit time per loop per neutrino energy E. The string features we consider are quasi-cusps, quasi-kinks, and kink-kink collisions, shown in Fig. 4.13, so that the label a takes values $a \in \{qc, qk, kk\}$. We present the different emission models in Sec. 4.5. In general, a loop can contain multiple features at once (e.g. a string could have 4 quasi-kinks and quasi-cusp). Here, for simplicity, we assume that only a single feature exists on every loop. We then write the emitted neutrino spectrum as

$$\frac{d\dot{N}^e_{i,a}(t,L,E)}{dN_{\rm loop}dE} = \frac{1}{[(L/2)/c]} \int dE_p \frac{dN^e_i(E,E_p)}{dN^e_a dE} \frac{dN^e_a(E_p,L)}{dE_p}, \tag{4.46}$$

with $[(L/2)/c]$ the period of oscillation for a cosmic string loop, $dN^e_i/dN^e_a dE$ the number of neutrinos emitted per parent particle per unit neutrino energy E, and dN^e_a/dE_p the number of parent particles emitted from string feature a per unit parent particle energy E_p.

If neutrinos are emitted directly from the cosmic string and there is no parent particle, we set $dN^e_i(E,E_p)/dN^e_a dE(E,E_p) = \delta(E-E_p)\delta^i_e$ with $\delta(x)$ the Dirac

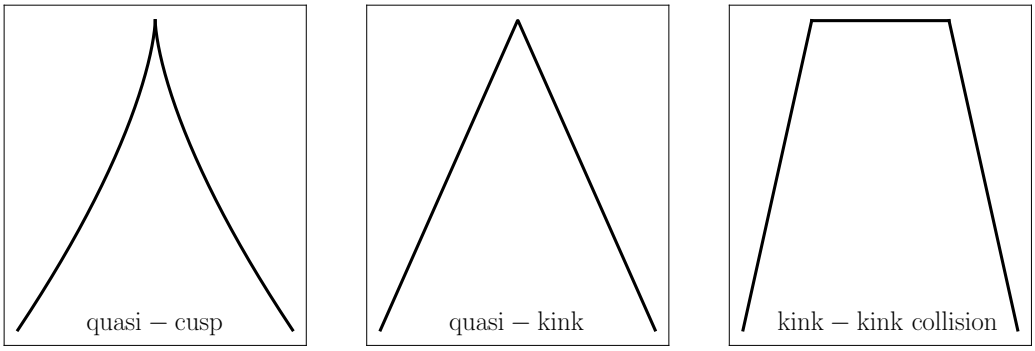

Figure 4.13: Picture of quasi-cusps, quasi-kinks, and kink-kink collisions.

delta function and δ_i^j the kronecker delta function that determines if the neutrino i is the same as the emitted particle in emission model e.

Roughly speaking, the cosmic string phenomenology is then encoded in the emitted neutrino spectrum, and the cosmic string population dynamics in its number density.

Neutrino self-interactions (νSI) in the Standard Model (SM) induce scattering between HEANs and cosmic background neutrinos and thus a nonzero HEAN optical depth. We evaluate the total HEAN optical depth following Ref. [154], including all seven channels of SM νSI. These channels lead to a sharply defined neutrino horizon at redshift z_{ν_i}. That is, an observer located at redshift $z(t)$ will not see neutrinos of a given energy E originating from a redshift $z(t') > z_{\nu,i}(t, E)$. Therefore, in order to simplify our expressions, we

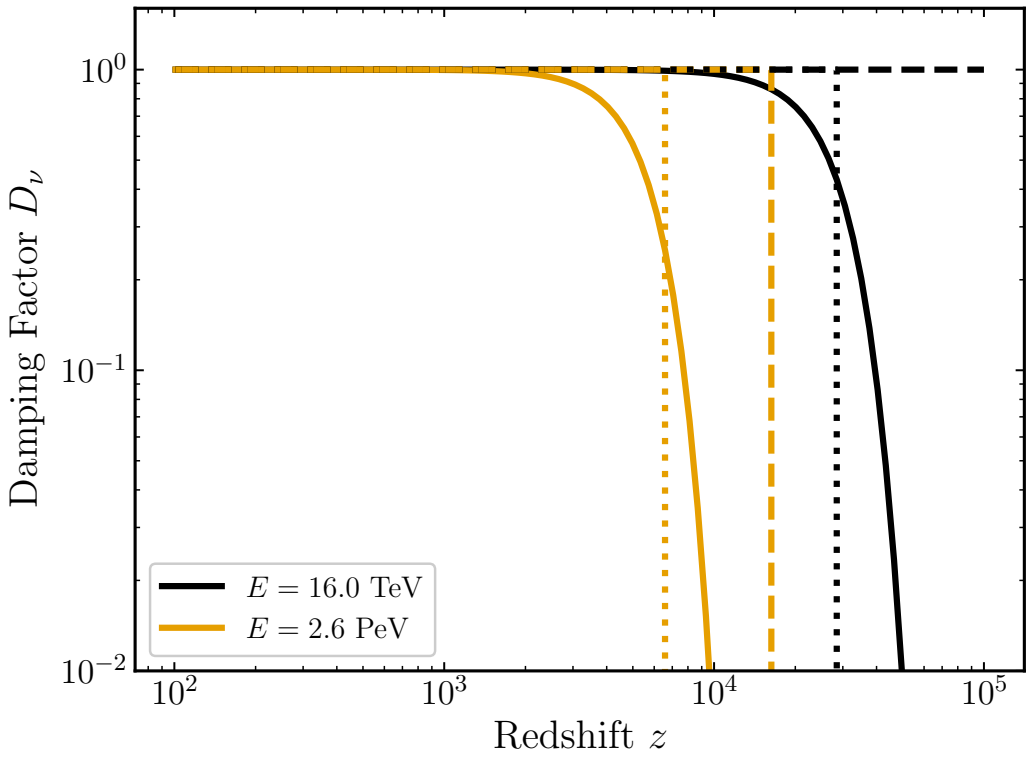

Figure 4.14: The HEAN damping factor D_{ν_i}. The solid lines indicate the complete damping factor, the dashed the approximation given by Ref. [2], and the dotted are given by our approximation in Eq. (4.47)

will take the following approximation

$$D_{\nu_i}(t', t, E) \equiv e^{-\tau_i(t', t, E)} = \Theta[z_{\nu_i}(t, E) - z(t')], \tag{4.47}$$

for the damping factor, with z_{ν_i} defined by the expression $D_{\nu_i}\{t'[z_{\nu,i}(t, E)], t, E\} = \exp(-1)$. We show both the complete HEAN optical depth and our approximation in Fig. 4.14 for some typical energies.

4.5 Cosmic String Phenomenology

Cosmic strings are topological defects formed after a $U(1)$ symmetry-breaking phase transition occurs in the Universe and are characterized by their tension μ. Then there are two broad phenomenological categories by which neutrinos may be emitted from this string. First, the string may directly couple to neutrinos. Second, it may indirectly couple to neutrinos; i.e. it may emit some intermediary particle which then eventually converts to some number of neutrinos. In either case, we model the free string loop action using the Nambu-Goto action for a infinitely long straight string, as locally the string loop is straight, regardless of any features

$$\mathcal{L}_{\rm str} = -\frac{\mu}{\hbar c}\int d^2\sigma\sqrt{-\gamma}\delta^4[x^\mu - X^\mu(\sigma,\tau)], \tag{4.48}$$

where $\hbar$ is Planck's constant, $g \equiv \det g_{\mu\nu}$ is the determinant of the spacetime metric $g_{\mu\nu}$, and γ the analogous quantity for the induced worldsheet metric $\gamma_{ab} = g_{\mu\nu}X^\mu_{,a}X^\nu_{,b}$ with worldsheet coordinates (σ,τ). We take the background metric to be flat $g_{\mu\nu} = \eta_{\mu\nu} = \mathrm{diag}(-1,1,1,1)$.

This string then has stress-energy tensor

$$T^{\rm str}_{\mu\nu}(x^\mu) = \frac{-\mu}{\sqrt{-g}}\int d^2\sigma\sqrt{-\gamma}\gamma_{ab}X^{,a}_\mu X^{,b}_\nu\delta^4[x^\mu - X^\mu(\sigma,\tau)] \tag{4.49}$$

with trace

$$T_{\rm str}(x^\mu) = -2\mu \int d^2\sigma \sqrt{-\gamma} \delta^4 \left[x^\mu - X^\mu(\sigma,\tau)\right], \tag{4.50}$$

where we neglect any backreaction of interactions onto the string as for the models we consider they are small. When considering interactions with this string we take an effective field theory approach and remain agnostic to any particular ultraviolet theory constraints.

4.5.1 Direct Coupling

For simplicity, we consider only a single neutrino species of mass $m_\nu = \hbar/(c\lambda_\nu)$ and take it to be a Dirac fermion. Thus its free Lagrangian is

$$\mathcal{L}^\nu_{\rm free} = -\bar{\nu}\left(i\gamma^\mu\partial_\mu - \lambda_\nu^{-1}\right)\nu, \tag{4.51}$$

with γ^μ the gamma matrices. There are two versions of direct cosmic string coupling we consider. First, the neutrinos may couple directly to the string worldsheet through a two-body interaction, so that its interaction is

$$\mathcal{L}^{(2)}_{\rm int} = \frac{g^{(2)}}{2}\left(\frac{\hbar c}{\mu^3}\right)^{1/2} \bar{\nu}\nu T_{\rm str}, \tag{4.52}$$

with $g^{(2)}$ the two-body interaction coupling. Second, neutrinos may couple through some gauge flux that permeates through the string in an Aharonov-Bohm (AB) fashion [257]

$$\mathcal{L}_{\rm int}^{\rm AB} = g_\nu \bar{\nu} \gamma^\mu V_\mu \nu, \tag{4.53}$$

with g_ν the charge of the neutrino under V_μ, V_μ a classical background field induced by the flux $\Phi = (2\pi/g_\nu)\theta_q$ the string carries, and θ_q the AB phase around the string. In the Lorentz gauge, this background field is writen as [258]

$$V_\mu = -\frac{i\Phi}{2} \int \frac{d^4k}{(2\pi)^4} \frac{p^\nu}{p^2} \int d\sigma_{\mu\nu} e^{-ik\cdot[x^\mu - X^\mu(\sigma,\tau)]}, \tag{4.54}$$

with $d\sigma_{\mu\nu} = d^2\sigma \epsilon^{\mu\nu\alpha\beta} \epsilon^{ab} X^\alpha_{,a} X^\beta_{,b}$ the worldsheet area element and $\epsilon^{i..j}$ the Levi-Civita symbol. Note that this field has support outside of the string, unlike the purely local interaction considered above.

4.5.2 Indirect Coupling

For indirect emission of neutrinos, we consider the intermediary particle to be a real scalar ϕ of mass $m_\phi = \hbar/(c\lambda_\phi)$. As a result, there is only one cosmic

string Lagrangian to write down

$$\mathcal{L} = \mathcal{L}_{\rm str} + \mathcal{L}^{\phi}_{\rm free} + \mathcal{L}^{\phi}_{\rm int}, \tag{4.55}$$

$$\mathcal{L}^{\phi}_{\rm free} = -\left(\frac{1}{2}\partial_\mu\phi\partial^\mu\phi + \frac{1}{2}\lambda_\phi^{-2}\phi^2\right), \tag{4.56}$$

$$\mathcal{L}^{\phi}_{\rm int} = \frac{\alpha}{(4\mu\hbar c)^{1/2}}\phi T_{\rm str}, \tag{4.57}$$

with, α is the scalar coupling constant.

In order to obtain neutrinos indirectly we consider two scenarios. First, the scalar particle decays directly into neutrinos via a Yukawa interaction

$$\mathcal{L}_{\rm Yu} = g_{\rm Yu}\bar{\nu}\phi\nu. \tag{4.58}$$

Alternatively, the scalar particle couples to some gauge boson - either a hidden sector gauge boson or the gluon, and these gauge fields have interactions which lead to a cascade of particles being emitted which end in neutrinos. For example, if it is the gluon, hadronic cascades produce pions which then lead to neutrino emission. For concreteness, we write down an example Lagrangian as

$$\mathcal{L}_{\rm casc} = \alpha\ell_{\rm P}\phi G_{\mu\nu}G^{\mu\nu}, \tag{4.59}$$

with $\ell_{\rm p}$ the Planck length and $G_{\mu\nu}$ the gluon field strength tensor.

4.6 Particle Emission

Given a model for cosmic string interactions with neutrinos, we now write the number spectrum of particles emitted from cosmic string loops. However, this spectrum depends not only on the phenomenology of the interactions, but also the feature of the string that emits the particle. Thus, in what follows, for each interaction considered we specify the type of feature as well.

In order to calculate the spectrum of emitted particles we take the leading-order S-matrix approach. Thus, we calculate the probability of creating a state $\langle k_1, s_1; \ldots; k_N, s_N|$ with N particles with momenta k_i and spin s_i out of the vacuum $|0\rangle$ given an interacting term,

$$\mathcal{A}_e(\mathbf{k}, \mathbf{s}) = i \int d^4x \, \langle k_1, s_1; \ldots; k_N, s_N| \, \mathcal{L}^e_{\rm int} \, |0\rangle \tag{4.60}$$

$$dN^e_a = \sum_{i=1}^{N_s} \sum_{s_{a_i}} \prod_{j=1}^{N} \frac{d^3k_j}{(2\pi)^2 \omega_j} |\mathcal{A}_e(\mathbf{k}, \mathbf{s})|^2, \tag{4.61}$$

with N_s the number of particles with non-zero spins, N the number of particles, a_i the map from spin particle number to particle number (e.g. a particle could be the 1st particle with spin but the 5th overall particle in a list) and the sum s_{a_i} goes over the possible spin values of particle a_i. Lower bounds on the energy of the resulting spectrum arise from integrating over the worldsheet. Upper bounds on the energy of the spectrum arise from the requirement that the energy of the particle is smaller than the string energy scale. For more details

we refer the reader to Ref. [249]. While both of these cutoffs in reality have a slight softening, they still decay rapidly and so here we approximate them as sharp discontinuous transitions.

The average power emitted from a cosmic string over one period of oscillation is therefore

$$dP_a^e = \frac{1}{[(L/2)/c]} \sum_{i=1}^{N_s} \sum_{s_{a_i}} \prod_{j=1}^{N} \frac{d^3 k_j}{(2\pi)^2 \omega_j} \left(\sum_{k=1}^{N} \omega_k \right) |\mathcal{A}_e(\mathbf{k}, \mathbf{s})|^2. \tag{4.62}$$

In order to complete the description of the string feature, several quantities must also be defined detailing the shape of the string feature in question. Rather than defining these quantities precisely, here we simply tabulate the numerical constants that encode their behavior, assuming that shape effects are $\mathcal{O}(1)$. Following this procedure, these constants then take a range of values: $\Theta \in [0.42, 3.6]$ and $\psi \in [0.047, 0.23]$. We define the rest of these constants in Table 4.1. For a first-principle definition of these parameters and their values we refer the reader to Ref. [249].

a	qc	qk	kk
$\mathcal{S}_a$	$[0.2, 10]$	$[0.1, 20]$	$[1, 500]$
$\mathcal{T}_a$	$[0.5, 50]$	$[1, 200]$	$[0.2, 200]$

Table 4.1: Range of values for cosmic-string shape-dependent variables, assuming the shape parameters are $\mathcal{O}(1)$.

4.6.1 Direct Coupling

First, we present the spectrum of neutrinos directly emitted from cosmic string loops with quasi-cusps, quasi-kinks, and kink-kink collisions.

4.6.1.1 Two-Body

For both quasi-cusps and quasi-kinks, the momenta of both emitted (nearly massless) fermions are parallel to one another, and thus the emission is helicity suppressed. For kink-kink collisions that emit relativistic neutrinos,

$$\frac{dN_{kk}^{(2)}}{dE} = \tilde{\Gamma}_{kk}^{(2)} \frac{E}{\mu\hbar c} \left[1 + \left(\frac{E^2}{\mu\hbar c} \right)^{1/2} \right]^{-3}, \tag{4.63}$$

$$P_{kk}^{(2)} = \Gamma_{kk}^{(2)} \frac{\mu c}{L/\ell_{(2)}}, \tag{4.64}$$

with $m_\nu c^2 \ll E \leq (\mu\hbar c)^{1/2}$ and $\tilde{\Gamma}_{kk}^{(2)} = 4\left[g^{(2)}\right]^2 \mathcal{S}_{kk}/(3\pi^2)$, $\Gamma_{kk}^{(2)} = (37/5)\tilde{\Gamma}_{kk}^{(2)}$ and $\ell_{(2)} = (\hbar c/\mu)^{1/2}$.

4.6.1.2 Aharonov-Bohm

In AB emission, there are no obvious suppressions, and so we write down the spectrum and power for all emission types in the relativistic limit,

$$\frac{dN_a^{\rm AB}}{dE} = \tilde{\Gamma}_a^{\rm AB}\left(\frac{\hbar c}{L}\right)^{q_a^{\rm AB}} \times \left[\frac{1}{(E+E_{\rm min}^{{\rm AB},a})^{1+q_a^{\rm AB}}} - \frac{1}{(E+E_{\rm max}^{{\rm AB},a})^{1+q_a^{\rm AB}}}\right], \tag{4.65}$$

$$P_a^{\rm AB} = \Gamma_a^{\rm AB}\frac{\mu c}{(L/\ell_{\rm AB})^{p_a^{\rm AB}}}, \tag{4.66}$$

with $\tilde{\Gamma}_{qc}^{\rm AB} = (2\pi\theta_q)^2\psi^{-4/3}\Theta^2/[32(2\pi)^4]\mathcal{T}_{qc}$, $\tilde{\Gamma}_{qk}^{\rm AB} = [3\mathcal{T}_{qk}/(4\mathcal{T}_{qc})](2/\Theta)\tilde{\Gamma}_{qc}^{\rm AB}$, $\tilde{\Gamma}_{kk}^{\rm AB} = (\mathcal{T}_{kk}/\mathcal{T}_{qc})(2\Theta^2)^{-1}\psi^{4/3}\tilde{\Gamma}_{qc}^{\rm AB}$, and $\ell_{\rm AB} = (\hbar c/\mu)^{1/2}$. We define all other variables in Table 4.2.

a	qc	qk	kk
$q_a^{\rm AB}$	0	$1/3$	0
$p_a^{\rm AB}$	$1/2$	$4/3$	1
$\Gamma_a^{\rm AB}$	$\log(16)\tilde{\Gamma}_{qc}^{\rm AB}$	$18(1-2^{-1/3})\tilde{\Gamma}_{qk}^{\rm AB}$	$\log(16)\tilde{\Gamma}_{kk}^{\rm AB}$
$E_{\rm min}^{{\rm AB},a}$	$\psi m_\nu c^2\sqrt{m_\nu cL/\hbar}$	$\psi m_\nu c^2\sqrt{m_\nu cL/\hbar}$	$m_\nu c^2$
$E_{\rm max}^{{\rm AB},a}$	$[(\mu^2L^2)(\mu\hbar c)]^{1/4}$	$(\mu\hbar c)^{1/2}$	$(\mu\hbar c)^{1/2}$

Table 4.2: AB variable definitions

4.6.2 Indirect Coupling

Now, we present the spectrum of neutrinos indirectly emitted from cosmic string loops. More concretely, we first present the spectrum of real scalar parti-

cles directly emitted from string loops with quasi-cusps, quasi-kinks, and kink-kink collisions. Then, we write the spectrum of neutrinos emitted from a real scalar.

Once again, there are no obvious suppressions, and so the string feature spectra and emitted power are

$$\frac{dN_a^\phi}{dE_\phi} = \tilde{\Gamma}_a^\phi \left(\frac{E_\phi L}{\hbar c}\right)^{q_a^\phi} \frac{\mu \hbar c}{E_\phi^3}, \tag{4.67}$$

$$P_a^\phi = \frac{\Gamma_a^\phi \mu c}{(L/\ell_\phi)^{p_a^\phi}}, \tag{4.68}$$

with E_ϕ the lab frame energy of the ϕ particle (different from the neutrino energy E) and $\ell_\phi = \ell_{\rm Yu} = \ell_{\rm casc} = \lambda_\phi$. All other variable definitions are placed in Table 4.3. After the real scalar is emitted, we assume it emits neutrinos instantaneously.

a	qc	qk	kk
q_a^ϕ	$2/3$	$1/3$	0
p_a^ϕ	$1/2$	1	1
$\tilde{\Gamma}_a^\phi$	$\alpha^2 \mathcal{S}_{qc}^\phi \Theta^2/[2(2\pi)^2]$	$\alpha^2 \mathcal{S}_{qk}^\phi \Theta/[2(2\pi)^2]$	$\alpha^2 \mathcal{S}_{kk}^\phi/(2\pi)^2$
Γ_a^ϕ	$6\psi^{-1/3}\tilde{\Gamma}_{qc}^\phi$	$6\psi^{-2/3}\tilde{\Gamma}_{qk}^\phi$	$2\tilde{\Gamma}_{kk}^\phi$
$E_{\rm min}^{\phi,a}$	$\psi m_\phi c^2 \sqrt{m_\phi c L/\hbar}$	$\psi m_\phi c^2 \sqrt{m_\phi c L/\hbar}$	$m_\phi c^2$
$E_{\rm max}^{\phi,a}$	$[(\mu^2 L^2)(\mu \hbar c)]^{1/4}$	$(\mu \hbar c)^{1/2}$	$(\mu \hbar c)^{1/2}$

Table 4.3: Variable definitions for the real scalar ϕ

4.6.2.1 Yukawa

Through a Yukawa coupling, two neutrinos are emitted from the heavy real scalar ϕ with an isotropic (i.e flat energy) spectrum

$$\frac{dN^{\rm Yu}}{dE} = \frac{1}{E_\phi}, \tag{4.69}$$

with $m_\nu \ll E \leq E_\phi$.

Therefore, the total number of neutrinos emitted from a cosmic string loop is also independent of the neutrino energy,

$$\frac{dN_a^{\rm Yu}}{dE} = \tilde{\Gamma}_a^{\rm Yu} \left(\frac{\lambda_\phi}{L}\right)^{q_a^{\rm Yu}} \frac{\mu\lambda_\phi^2}{\hbar c} \frac{1}{m_\phi c^2}, \tag{4.70}$$

with all variable definitions in Table 4.4.

a	qc	qk	kk
$q_a^{\rm Yu}$	$1/2$	0	0
$\tilde{\Gamma}_a^{\rm Yu}$	$(3/7)\psi^{-7/3}\tilde{\Gamma}_{qc}^{\phi}$	$(3/8)\psi^{-8/3}\tilde{\Gamma}_{qk}^{\phi}$	$(1/3)\tilde{\Gamma}_{kk}^{\phi}$
$E_{\rm min}^{\rm Yu,a}$	$m_\nu c^2$	$m_\nu c^2$	$m_\nu c^2$
$E_{\rm max}^{\rm Yu,a}$	$E_{\rm max}^{\phi,qc}$	$E_{\rm max}^{\phi,qk}$	$E_{\rm max}^{\phi,kk}$

Table 4.4: Yukawa variable definitions

4.6.2.2 Cascade

After the heavy scalar decays, a cascade of particles decays ensues, of which neutrinos are one of the end products. In according with previous studies [259–

262], we assume that the decay spectra follows a power law with index ~ -2 and that approximately all of the energy is transferred to pions, which then decay to give half of their energy to neutrinos. After imposing conservation of energy in the decay between neutrinos and the heavy real scalar we obtain

$$\frac{dN^{\rm casc}}{dE} = \frac{b_*}{2}\frac{E_\phi}{E^2}, \tag{4.71}$$

with $b_* = \log\left(E^{\rm casc}_{\rm max}/E^{\rm casc}_{\rm min}\right)^{-1}$. As a result, the total number of neutrinos emitted from a cosmic string loop is

$$\frac{dN^{\rm casc}_a}{dE} = \tilde{\Gamma}^{\rm casc}_a b_* \left(\frac{\lambda_\phi}{L}\right)^{q^{\rm casc}_a} \frac{\mu\lambda_\phi}{E^2}, \tag{4.72}$$

with all variable definitions in Table 4.5.

a	qc	qk	kk
$q^{\rm casc}_a$	$-1/2$	0	0
$\Gamma^{\rm casc}_a$	$(1/4)\Gamma^\phi_{qc}$	$(1/4)\Gamma^\phi_{qk}$	$(1/4)\Gamma^\phi_{kk}$
$E^{\rm casc,a}_{\rm min}$	$(1/2)\sqrt{m_\phi c^2 Q_h}$	$(1/2)\sqrt{m_\phi c^2 Q_h}$	$(1/2)\sqrt{m_\phi c^2 Q_h}$
$E^{\rm casc,a}_{\rm max}$	$0.1E^{\phi,qc}_{\rm max}$	$0.1E^{\phi,qk}_{\rm max}$	$0.1E^{\phi,kk}_{\rm max}$

Table 4.5: Cascade variable definitions, with $Q_h = 1$ GeV the hadronization energy scale.

4.7 String Loop Population

A loop of initial length L_i at time t_i will contract as it radiates energy from various string features. For the string interaction models presented here, this energy may either be in the form of gravitational waves, neutrinos, or real scalar fields. However, we do not consider emission via all these channels at once. Instead, in order to determine the evolution of the loop distribution function, we consider emission in a pair of channels: first, from gravitational waves and second, from a single specified particle model. This choice is done because cosmic string loops are always expected to radiate gravitationally and our models are an addition beyond the standard framework. As a result, the center of mass energy μL of a loop decrease over time according to

$$\mu \frac{dL}{dt} = -\Gamma_g G\mu^2 c^{-3} - P_a^e, \tag{4.73}$$

with $\Gamma_g \in [50, 100]$. The first term encodes loop emission of gravitational waves, while the second term specifies the emission e from string feature a. Moreover, loops with length $L > L_a^e = \ell_e \left[(\Gamma_a^e/\Gamma_g)/(G\mu c^{-4})\right]^{1/p_a^e}$ emit more energy in the form of gravitational waves than from emission e from string feature a.

In general, Eq.(4.73) does not have an analytic solution for arbitrary initial loop length. However, loops with $L_i < L_a^e$ will always emit more particles than gravitational waves, and those with $L_i \gg L_a^e$ more gravitational waves than

particles. Therefore we solve for the evolution of loop length with these two conditions. Moreover, in practice, the conditon $L_i \gg L_a^e$ is relaxed to $L_i > L_a^e$, so that there are only two regimes:

$$L(t_i, t, L_i) = \left[L_i^{1+p_a^e} - (L_{\rm min}^{e,a})^{1+p_a^e}\right]^{\frac{1}{1+p_a^e}} \Theta\left(L_a^e - L_i\right) + \left[L_i - \Gamma_g G\mu c^{-3}(t-t_i)\right] \Theta\left(L_i - L_a^e\right), \tag{4.74}$$

which can be piecewise-inverted to solve for L_i as a function of L. Here, $L_{\rm min}^{e,a} = \left[(1+p_a^e)\Gamma_a^e c(t-t_i)\ell_e^{p_a^e}\right]^{1/(1+p_a^e)}$.

While some cosmic string loops are present at the initial $U(1)$ phase transition, most are formed after string segments intersect and commute, breaking off into smaller loops. Here, we assume this string loop population has relaxed to a steady-state self-similar solution. As a result, we neglect terms that involve string collision and string self-interactions. While these loops are produced both during periods of radiation and matter domination, those produced during matter domination are less abundant [263]. Therefore, we write the

loop distribution as $dn^{\rm loop}/dL = dn_r^{\rm loop}/dL$, with

$$\frac{dn_r^{\rm loop}(t,L)}{dL} = \frac{\zeta_r}{2}\frac{a_{\rm eq}^3}{[a(t_{\rm eq})\chi(t_{\rm eq})]^{3/2}L_0^{5/2}}\left(\frac{L}{L_0}\right)^p \times \begin{cases} \Theta\left(\beta_r - \frac{L}{2ct}\right) & t \le t_{\rm eq} \\ \Theta\left(\beta_r - \frac{L_{eq}}{2ct_{\rm eq}}\right) & t > t_{\rm eq} \end{cases} \tag{4.75}$$

the distribution of loops created during radiation-domination at a time t. Moreover, $t_{\rm eq}$ is the time of matter-radiation equality, χ the comoving horizon distance, $\zeta_r = 1.04$ a normalization factor, $\beta_r = 0.05$ the typical scale of loops produced radiation domination relative to the size of the horizon. Finally, $L_0 = L_i(0,t,L)$ and $L_{\rm eq} = L_i(t_{\rm eq},t,L)$ are the lengths of a loop at $t = 0$ and $t_{\rm eq}$. We show some example distributions for cosmic string loops in Fig. 4.15 and Fig. 4.16.

4.8 Results

Given the emission spectra of neutrinos from a single cosmic string loop, as well as the distribution of cosmic string loops, we now present both the source function and flux for each phenomenological case. We then use the dominant flux to place an upper bound on the fraction f_a^e of HEAN sourced by cosmic string loops. The bounds are obtained in the following manner.

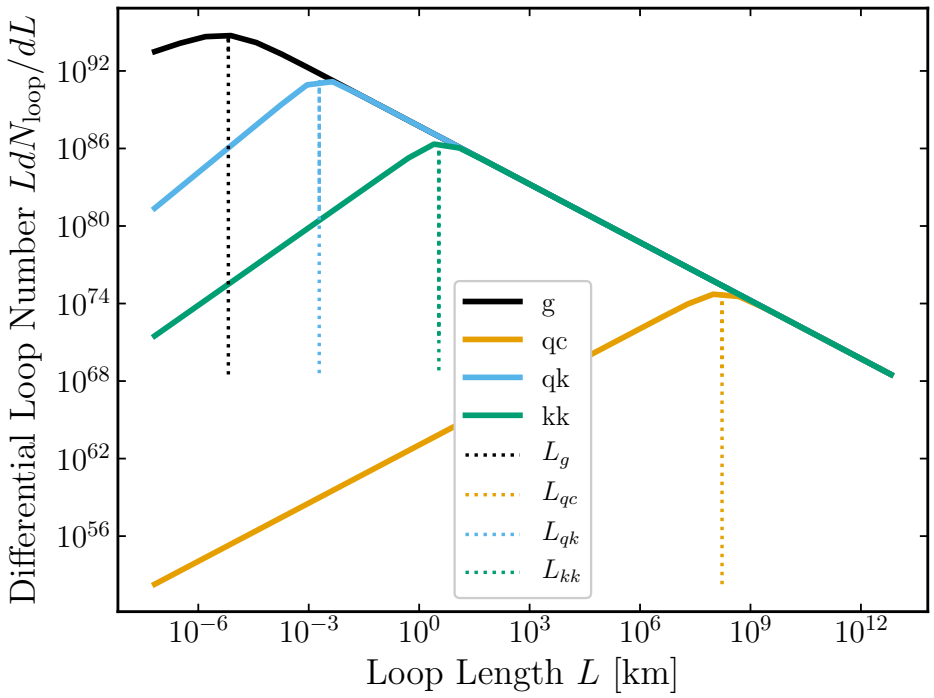

Figure 4.15: The differential loop number $dN_{\rm loop}/dL = \chi^3 dn_{\rm loop}/dL$, with χ the size of the comoving horizon, evaluated at $z = 0$. The solid black line is the number assuming only gravitational emission, while the solid orange (blue) [green] line is due to both gravitational emission and AB emission from quasi-cusps (quasi-kinks) [kink-kink collisions]. The vertical dotted lines indicate the length $L^{e,a}_{\rm min}$.

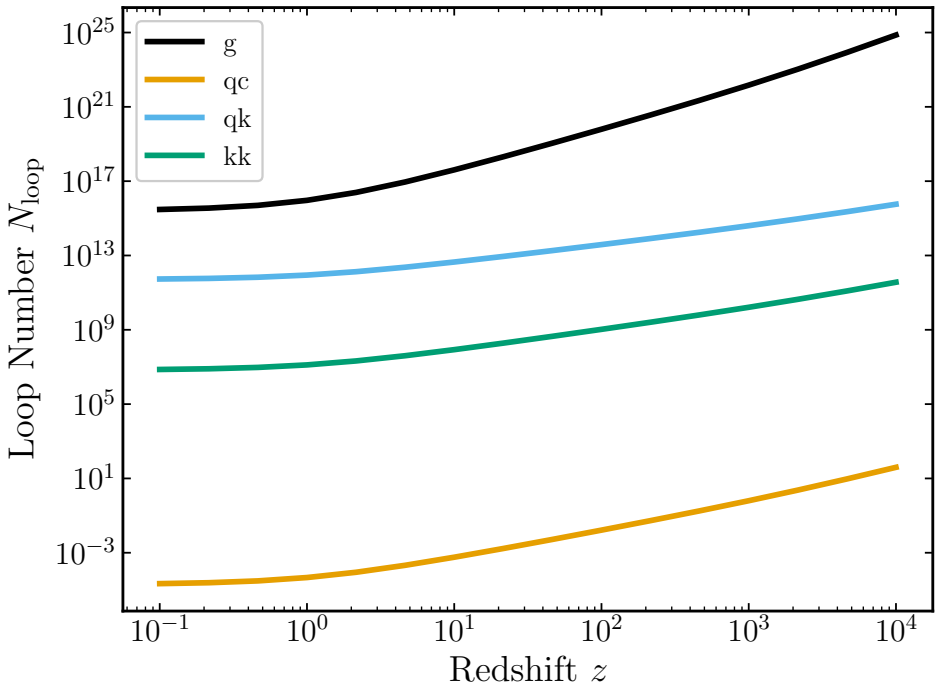

Figure 4.16: The number of loops $N_{\rm loop} = \chi^3 n_{\rm loop}$, with χ the size of the comoving horizon, as a function of redshift. The label and color scheme follows that of Fig. 4.15. Hence, loop distributions with smaller $L_{\rm min}$ have higher numbers.

First, evaluating Eq. (4.45), we obtain

$$S_a^e(t,E) = cA_a^e \frac{dN_a^e[E, L_{\rm min}^{e,a}(t)]}{dE} \frac{dn_{\rm loop}[0, L_{\rm min}^{e,a}(t)]}{dL}, \tag{4.76}$$

$$\begin{aligned} A_a^e \equiv & \frac{4}{1+p_a^e} \frac{\Gamma\left(\frac{5+2q_a^e}{2+2p_a^e}\right)}{\Gamma\left(\frac{7+2p_a^e+2q_a^e}{2+2p_a^e}\right)} \\ & \times_2 F_1\left[1+\frac{3}{2+2p_a^e}, \frac{5+2q_a^e}{2+2p_a^e}, \frac{7+2p_a^e+2q_a^e}{2+2p_a^e}, -1\right] \end{aligned} \tag{4.77}$$

with $\Gamma(n)$ the Gamma function, and ${}_2F_1(a,b,c,d)$ a hypergeometric function. In this expression, we remind that $a \in \{qc, qk, kk\}$ and $e \in \{(2), \mathrm{AB}, \mathrm{Yu}, \mathrm{casc}\}$.

We define the index of the local energy spectrum through the expression $dN_a^e/dE \propto E^{-\gamma_a^e}$. Using Eq. (4.47) and Eq. (4.76), we evaluate Eq. (4.44), after changing variables from time to redshift via $dt/dz = -1/[H(z)(1+z)]$, to obtain

$$\Phi_a^e(t,E) = I_a^e(t,E) \frac{c^2}{H_0} \frac{dN_a^e[E, L_{\rm min}^{e,a}(t)]}{dE} \frac{dn_{\rm loop}[0, L_{\rm min}^{e,a}(t)]}{dL} \tag{4.78}$$

$$I_a^e(t,E) \equiv A_a^e \int_{z(t)}^{z_\nu(t,E)} \frac{dz}{E(z)} (1+z)^{-\gamma_a^e} f(z)^{-(q_a^e+\frac{5}{2})/(p_a^e+1)}, \tag{4.79}$$

with $H(z) = H_0 E(z)$ the Hubble parameter, H_0 Hubble's constant, $E(z) = [\Omega_m(1+z)^3 + (1-\Omega_m) + \Omega_r(1+z)^4]^{1/2}$ for ΛCDM, Ω_m the matter-density parameter, Ω_r the radiation-density parameter , and $f(z) = t(z)/t$. We present the values for $I_a^e(t_0, E_{\rm min})$ in Table 4.6 using Planck 2018 parameters [73].

To make easy connection with observation, we reparametrize the neutrino

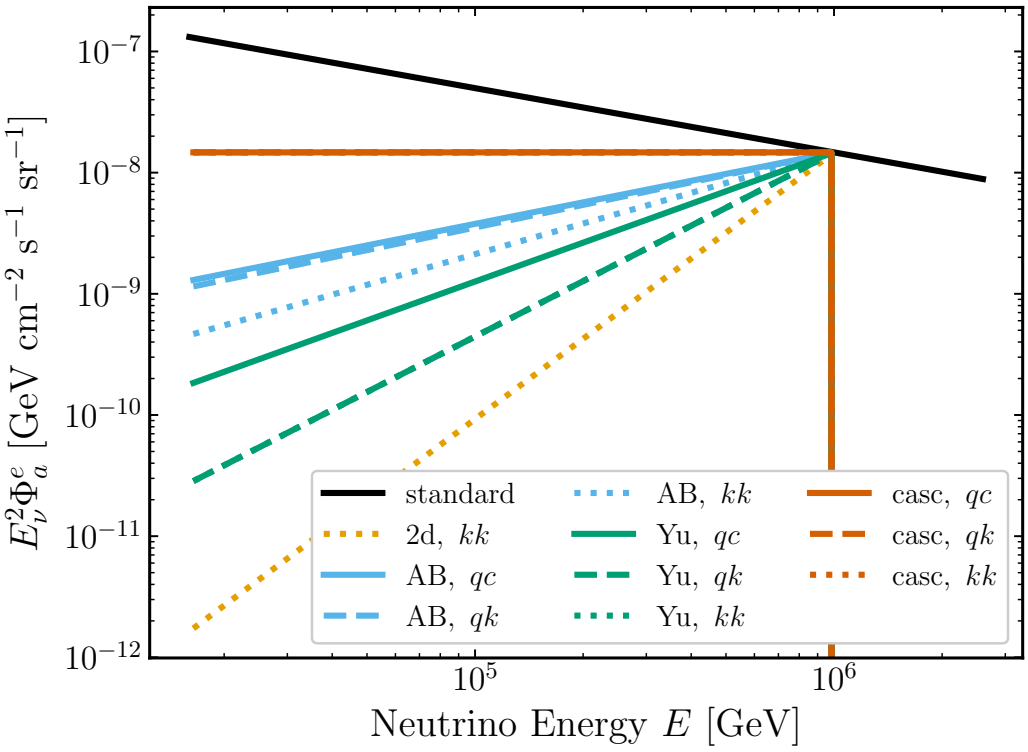

Figure 4.17: Spectra of HEAN emitted from cosmic strings using Eq. (4.80) compared to the observed HEAN spectrum (in solid black) using Eq. (4.82). The orange (blue) [green] {red} line indicates HEAN emission via the (2) (AB) [Yu] {casc} model. Moreover, solid (dashed) [dotted] lines indicate that the string population contains quasi-cusps (quasi-kinks) [kink-kink collisions]. We choose $E_{\rm max}^{e,a} = 10^6$ GeV. For large enough amplitude values, the spectrum may appear as a bump before the sharp cutoff.

I_a^e	qc	qk	kk
(2)	N/A	N/A	4.35×10^{10}
AB	94900	15.2	241
Yu	3.25×10^{11}	2.40×10^6	2.40×10^6
casc	2.56	2.04	2.04

Table 4.6: Tabulated values for $I_a^e(t_0, E_{\rm min})$, $E_{\rm min} = 16$ TeV, with a specified by the column and e by the row. For emission of type (2), quasi-cusps and -kinks are helicity suppressed and so we do not consider them here.

spectrum $\Phi_a^e(t_0, E)$ today as a power law with a sharp cutoff,

$$\Phi_a^e(t_0, E) \simeq C_0 B_a^e (E/E_0)^{-\beta_a^e} \Theta\left(E - E_{\rm max}^{e,a}\right) \Theta\left(E - E_{\rm min}^{e,a}\right), \tag{4.80}$$

with $C_0 = 2 \times 10^{-18}$ GeV^{-1}cm^{-2}s^{-1}sr^{-1} and $E_0 = 100$ TeV. Note that, for most cosmic string parameter values, $E_{\rm min}^{a,e}$ is much smaller than observed HEAN energies and so the low-energy cutoff can be ignored. We write this equation as an approximate equality as the spectral index β_a^e has a nonzero running with energy, $d\beta_a^e/dE \neq 0$. However, this running is small and so we average its value over the observed energy range. Moreover, note that $\beta_a^e \neq \gamma_a^e$ as the energy dependence of the neutrino horizon shifts the spectral index, which we show in Table 4.7. We show the dependence of the amplitude B_a^e on our model parameters in Table 4.8. In order to save space in the table, we include a scaling of the b_* parameter in Eq. (4.81). Using the new parametrization of Eq. (4.80), we plot some example spectra in Fig. 4.17.

β_a^e	qc	qk	kk
(2)	N/A	N/A	-0.27
AB	1.37	1.38	1.14
Yu	0.855	0.439	0.439
casc	2	2	2

Table 4.7: Tabulated values for β_a^e, with a specified by the column and e by the row.

B_a^e	qc	qk	kk
(2)	N/A	N/A	$1.09 \times 10^{-4} \left(\frac{\tilde{\Gamma}^{(2)}_{kk}}{10^{36}}\right)^{-1/4} \left(\frac{G\mu c^4}{4.5\times10^{-26}}\right)^{-3/8}$
AB	$0.383 \left(\frac{\tilde{\Gamma}^{\rm AB}_{qc}}{10^{-25}}\right)^{-2/3} \left(\frac{G\mu c^{-4}}{4.5\times10^{-26}}\right)^{5/12}$	$2.71 \left(\frac{\tilde{\Gamma}^{\rm AB}_{qk}}{10^{6}}\right)^{-3/14} \left(\frac{G\mu c^{-4}}{4.5\times10^{-26}}\right)^{17/21}$	$0.0212 \left(\frac{\tilde{\Gamma}^{\rm AB}_{kk}}{10^{10}}\right)^{-1/4} \left(\frac{G\mu c^{-4}}{4.5\times10^{-26}}\right)^{5/8}$
Yu	$0.569 \left(\frac{\tilde{\Gamma}^{\rm Yu}_{qc}}{10^{-28}}\right)^{-1} \left(\frac{G\mu c^{-4}}{4.5\times10^{26}}\right) \left(\frac{m_\phi c^2}{10^5\ \rm GeV}\right)^{-5/2}$	$9.28 \left(\frac{\tilde{\Gamma}^{\rm Yu}_{qk}}{10^{10}}\right)^{-1/4} \left(\frac{G\mu c^{-4}}{4.5\times10^{26}}\right) \left(\frac{m_\phi c^2}{10^5\ \rm GeV}\right)^{-7/4}$	$62.8 \left(\frac{\tilde{\Gamma}^{\rm Yu}_{kk}}{10^{20}}\right)^{-1/4} \left(\frac{G\mu c^{-4}}{4.5\times10^{-26}}\right) \left(\frac{m_\phi c^2}{10^5\ \rm GeV}\right)^{-7/4}$
casc	$\frac{3.42}{1000} \left(\frac{b_*}{7.4}\right) \left(\tilde{\Gamma}^{\rm casc}_{qc}\right)^{-1/3} \left(\frac{G\mu c^{-4}}{4.5\times10^{-24}}\right) \left(\frac{m_\phi c^2}{10^7\ \rm GeV}\right)^{1/6}$	$28.2 \left(\frac{b_*}{7.4}\right) \left(\tilde{\Gamma}^{\rm casc}_{qk}\right)^{-1/4} \left(\frac{G\mu c^{-4}}{4.6\times10^{-24}}\right) \left(\frac{m_\phi c^2}{10^7\ \rm GeV}\right)^{1/4}$	$307 \left(\frac{b_*}{7.4}\right) \left(\tilde{\Gamma}^{\rm casc}_{kk}\right)^{-1/4} \left(\frac{G\mu c^{-4}}{4.5\times10^{-24}}\right) \left(\frac{m_\phi c^2}{10^7\ \rm GeV}\right)^{1/4}$

Table 4.8: Tabulated values for B_a^e, with a specified by the column and e by the row. The scaling of b_* is shown in Eq. (4.81). Fiducial values are chosen so that they are not ruled out by HEAN spectra observations.

$$\exp\left(b_*\right) = 1640 \left(\frac{G\mu c^{-4}}{4.5\times10^{-24}}\right)^{1/2} \left(\frac{m_\phi c^2}{10^7\ \rm GeV}\right)^{1/2} \tag{4.81}$$

We now identify the viable parameter space of cosmic string HEAN emission subject to the constraint that it not greater than the observed HEAN spectrum, $\Phi_a^e(E) \leq \Phi_{\rm HEAN}(E)$, for all energies. We model the observed HEAN spectrum as a power law with spectral index $\gamma = 2.53$ [235],

$$\Phi_{\rm HEAN}(E) = C_0 \Phi_0 \left(E/E_0\right)^{-\gamma}, \tag{4.82}$$

with $\Phi_0 = 1.66$. We take the observed HEAN energy range to be $E_{\rm min} =$

$16\ \mathrm{TeV} \leq E \leq E_{\mathrm{max}} = 2.6\ \mathrm{PeV}$. As a result, the three equations

$$B_a^e \leq \Phi_0 \left(E_{\mathrm{max}}^{e,a}/E_0\right)^{\beta_a^e - \gamma}, \tag{4.83}$$

$$E_{\mathrm{min}} \leq E_{\mathrm{max}}^{e,a} \leq E_{\mathrm{max}}, \tag{4.84}$$

$$E_{\mathrm{min}}^{e,a} \leq E_{\mathrm{max}}^{e,a} \tag{4.85}$$

define a region in the cosmic string parameter space that is viable to contribute to the HEAN flux and whose upper bound we show in Fig. 4.18. Parameters that are above this upper bound are ruled out, as they would lead to a HEAN spectrum larger than what we observe. In order to relate these equations to the original parameters, one can use the formulas listed in Tables 4.7 and 4.8, along with the definition of $E_{\mathrm{max}}^{e,a}$ listed in the Tables in Sec 4.6.

The fraction f_a^e of observed neutrinos associated with a cosmic string spectrum given by emission model e and string feature a is then

$$f_a^e = \frac{\int_{E_{\mathrm{min}}}^{E_{\mathrm{max}}} dE A_{\mathrm{eff}}(E) \Phi_a^e(t_0, E)}{\int_{E_{\mathrm{min}}}^{E_{\mathrm{max}}} dE A_{\mathrm{eff}}(E) \Phi_{\mathrm{HEAN}}(E)}, \tag{4.86}$$

with $A_{\mathrm{eff}}(E)$ the effective area of IceCube for muon neutrinos, which we take from Ref. [180]. We plot the maximum contribution of cosmic string loops [i.e. when $\Phi_a^e(t_0, E_{\mathrm{max}}^{e,a}) = \Phi_{\mathrm{HEAN}}(E_{\mathrm{max}}^{e,a})$]in Fig. 4.19.

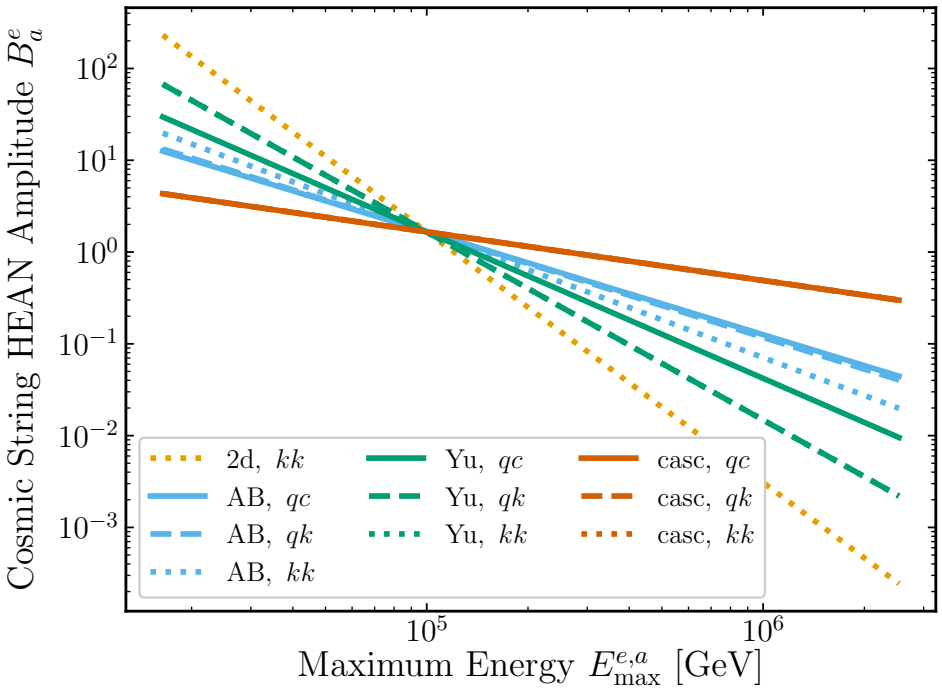

Figure 4.18: The maximum amplitude B_a^e of HEANs that come from a population of cosmic string loops using Eq. (4.83). The orange (blue) [green] {red} line indicates HEAN emission via the (2) (AB) [Yu] {casc} model. Moreover, solid (dashed) [dotted] lines indicate that the string population contains quasi-cusps (quasi-kinks) [kink-kink collisions]. All lines intersect at $E_{\rm max}^{e,a} = E_0$ by construction of our parameterization. Values of B_a^e above a given line are ruled out. Table 4.8 translates these amplitudes into cosmic string parameters.

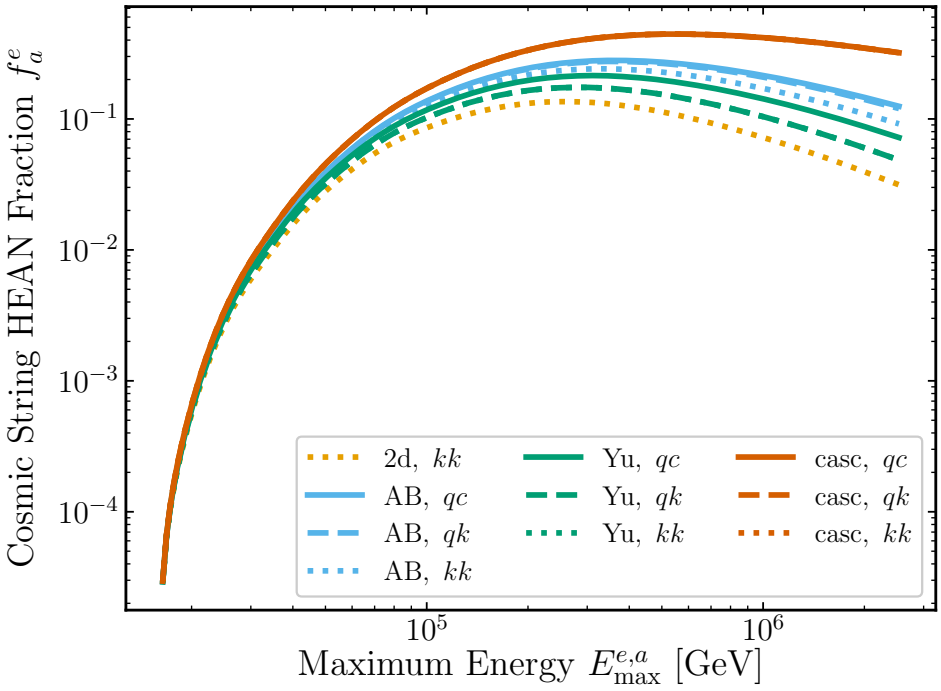

Figure 4.19: The maximum fraction of HEANs that come from a population of cosmic string loops using Eq. (4.86). The orange (blue) [green] {red} line indicates HEAN emission via the (2) (AB) [Yu] {casc} model. Moreover, solid (dashed) [dotted] lines indicate that the string population contains quasi-cusps (quasi-kinks) [kink-kink collisions].

4.9 Discussion

We clarify five assumptions and present six comments. First, in each model of neutrino emission we assume a single neutrino. If there are multiple neutrino species coupled to the string, then energy extracted from the loop will be a sum over all neutrino emission channels. Moreover, since cosmic strings are distant objects, then the observed spectrum of neutrinos will be a sum of the spectrum of each neutrino channel weighed by the corresponding probability of oscillating into that neutrino. Note that even if there is only one neutrino coupled, then flavor oscillations will decrease the spectral amplitude in that flavor. Regardless, the effects of oscillations can always be absorbed into a redefintion of $\tilde{\Gamma}$ and so our results can be scaled appropriately to include them.

Second, if the neutrino is a Majorana fermion instead of a Dirac fermion, then $\bar{\nu} = \nu^{\mathrm{T}}\mathcal{C}$ with $\mathcal{C}$ the charge conjugation matrix. This replacement will not change the spectral index, and should not change the amplitude of emission by more than an $\mathcal{O}(1)$ coefficient.

Third, for the indirect emission models, we assume the heavy real scalar instantaneously decays into neutrinos.

Fourth, we did not consider cosmic string loop populations with multiple features (e.g. loops that have both quasi-kinks and -cusps). Since cusps extract more energy from the string than kinks and quasi-kinks, but typically have

smaller amplitudes, we expect that the presence of cusps would decrease the expected amplitude in the HEAN energy range (or alternatively, the presence of kinks to increase the amplitude). Thus, our results safely represent an upper limit on the possible contribution of cosmic strings to the HEAN spectrum.

Fifth, we assume that the population of cosmic string is characterized by a single string tension value. Instead, it is possible that there exists multiple varieties of cosmic strings in the Universe, with each cosmic string characterized by a different string tension, and thus the resulting spectrum would be the sum of these two types of strings. In addition, the string tension may have some time dependence [264], leading to a HEAN spectrum that would be average over the distribution of tension values. Both of these cases are beyond the scope of this work.

While we do consider a wide variety of emission models here, the list is not exhaustive. For example, we did not consider 2-body emission of real scalars from cosmic strings than then decay in HEAN. In the case of 2-body emission of real scalars, this model would not change the spectrum index of emission relative to its 1-body counterpart. This similarily is because the index is controlled by the Yukawa and cascade decays. Therefore, while the precise values for the amplitude $\tilde{\Gamma}$ may change, the maximum contribution to the HEAN spectrum will not. In other cases, unless the spectral index of emission just so happens to match the one of the observed spectrum, we expect our limit, of no more than

45% of HEANs to come from cosmic strings, to hold.

In addition to emission models, it is also possible that cosmic strings collide and annihilate with one another into neutrinos. However, cosmic strings are very thin and so their annihilation cross-section is very small. Thus, we do not expect such a process to contribute greatly.

Even though we find that the models presented are a subdominant portion of the total spectrum, the presence of a sharp cutoff implies that HEANs from cosmic strings may present as a distinct bump in the observed HEAN spectrum, opening up the possibility for their detection. Moreover, if cosmic strings exist, their gravitational wells would alter energies of traversing photons. Hence, in principle, cross correlations of HEAN maps with the cosmic microwave background would be able to distinguish cosmic strings from other subdominant contributions, although we expect such a signal to be very small.

In each of our plots in Sec. 4.8, the region to the right of the orange dashed line requires either values of the coupling constant or string feature parameters that are greater than $\mathcal{O}(1)$. It is both difficult to create such a theory and is at odds with the perturbative approach we took to calculating the spectra. Despite this, we leave this region in our plots as it may be the case other models with similar effective parameters and spectral indices are viable.

Moreover, in these plots, we only consider the constraints on the effective parameters describing HEAN emission from cosmic strings. At higher neu-

trino energies, where current and future experiments like ANITA [265] and POEMMA [266] can observe neutrinos, there will be additional constraints. The future upgrade of IceCube-Gen2 [247] will also allow detections of HEANs at lower energies, thus extending the range of our plots. In addition, in the cascade case, there will be an emission of gamma rays that go along with the neutrinos. Treatment of both of these effects are a work in progress and beyond the scope of this work.

Finally, we note that since we took an effective field theory approach to our problem, the parameter spaces we have identified may be constrained once linked to a corresponding UV completion. However, it is not inconceivable that these UV completions will still have unconstrained parameter spaces for HEAN emission. Regardless, such an investigation is beyond the scope of this work.

4.10 Conclusion

In this work we quantified the possible contribution of cosmic strings to the HEAN spectrum for a wide variety of models. First, we presented the general formula for calculating neutrino emission from distant sources and updated the calculation for the HEAN optical depth compared to previous works on cosmic string emission. In doing so, we both employed a more accurate numerical

approach and included all seven channels of Standard Model neutrino self-interactions.

Then, in order to classify possible models, we took an effective field theory approach and delineated two avenues of HEAN production: direct and indirect. In direct emission, the cosmic string emits HEANs through a direct coupling of neutrinos to the cosmic string, while in indirect emission the cosmic string emits a particle which then decays into HEANs. For both direct and indirect emission we consider two models each. That is, we considered direct emission of HEANs via a two-body emission and a Aharonov-Bohm coupling. For indirect emission, we considered the emission of a heavy real scalar which then decays into HEANs either from a Yukawa coupling or through a hadronic cascade. Aside from the cascade case, all other calculations have not been done before.

In addition to the particular cosmic string phenomenology, the energy spectrum of HEANs is also determined by the geometry of the string. In particular, efficient cosmic-string particle emission must come either from quasi-cusps, quasi-kinks, or kink-kink collisions on the string. Previous work has not considered emission from kink-kink collisions. Therefore, for each emission model and string feature, we then calculated the local energy spectrum of HEANs emitted from the cosmic string.

Next, we calculated the distribution of cosmic string loops that emit both

gravitational waves and a given neutrino emission model that specifies a string feature. These loops are created during radiation domination and then shrink as they emit energy. We note again that the shrinking due to non-gravitational emission has not been considered in previous works. In doing this calculation, we then also identified the dominant forms of energy emission in cosmic string loops and delineated their corresponding regimes.

With the local energy spectrum and cosmic-string loop distribution specified, we then calculated the HEAN energy spectrum today using the Boltzmann equation for each emission model and string feature and obtained a simple power law in with a sharp cutoff in Eq. (4.80). With these spectra, we then required each one must be less than the observed HEAN spectrum. This requirement led us to identify and constrain the corresponding parameter space of HEAN emission. As a result, we found that, with the models presented, cosmic strings can contribute no more than $\sim 45\%$ of HEANs.

Bibliography

[1] M. G. Aartsen *et al.*, "Characteristics of the diffuse astrophysical electron and tau neutrino flux with six years of IceCube high energy cascade data," *Phys. Rev. Lett.*, vol. 125, no. 12, p. 121104, 2020.

[2] V. Berezinsky, E. Sabancilar, and A. Vilenkin, "Extremely High Energy Neutrinos from Cosmic Strings," *Phys. Rev. D*, vol. 84, p. 085006, 2011.

[3] P. A. R. Ade *et al.*, "Planck 2015 results. XIII. Cosmological parameters," *Astron. Astrophys.*, vol. 594, p. A13, 2016.

[4] G. Hinshaw *et al.*, "Nine-Year Wilkinson Microwave Anisotropy Probe (WMAP) Observations: Cosmological Parameter Results," *Astrophys. J. Suppl.*, vol. 208, p. 19, 2013.

[5] B. J. Carr and S. W. Hawking, "Black holes in the early Universe," *Mon. Not. Roy. Astron. Soc.*, vol. 168, pp. 399–415, 1974.

[6] S. Bird, I. Cholis, J. B. Muñoz, Y. Ali-Haïmoud, M. Kamionkowski, E. D.

Kovetz, A. Raccanelli, and A. G. Riess, "Did LIGO detect dark matter?" *Phys. Rev. Lett.*, vol. 116, no. 20, p. 201301, 2016.

[7] S. Clesse and J. García-Bellido, "The clustering of massive Primordial Black Holes as Dark Matter: measuring their mass distribution with Advanced LIGO," *Phys. Dark Univ.*, vol. 15, pp. 142–147, 2017.

[8] M. S. Turner, "Windows on the Axion," *Phys. Rept.*, vol. 197, pp. 67–97, 1990.

[9] G. G. Raffelt, "Astrophysical methods to constrain axions and other novel particle phenomena," *Phys. Rept.*, vol. 198, pp. 1–113, 1990.

[10] D. Cadamuro and J. Redondo, "Cosmological bounds on pseudo Nambu-Goldstone bosons," *JCAP*, vol. 02, p. 032, 2012.

[11] D. J. E. Marsh, "Axion Cosmology," *Phys. Rept.*, vol. 643, pp. 1–79, 2016.

[12] G. Carosi, A. Friedland, M. Giannotti, M. J. Pivovaroff, J. Ruz, and J. K. Vogel, "Probing the axion-photon coupling: phenomenological and experimental perspectives. A snowmass white paper," in *Community Summer Study 2013: Snowmass on the Mississippi*, 9 2013.

[13] A. Kusenko, "Sterile neutrinos: The Dark side of the light fermions," *Phys. Rept.*, vol. 481, pp. 1–28, 2009.

[14] G. Jungman, M. Kamionkowski, and K. Griest, "Supersymmetric dark matter," *Phys. Rept.*, vol. 267, pp. 195–373, 1996.

[15] L. Bergström, "Nonbaryonic dark matter: Observational evidence and detection methods," *Rept. Prog. Phys.*, vol. 63, p. 793, 2000.

[16] D. Hooper and S. Profumo, "Dark Matter and Collider Phenomenology of Universal Extra Dimensions," *Phys. Rept.*, vol. 453, pp. 29–115, 2007.

[17] K. M. Zurek, "Asymmetric Dark Matter: Theories, Signatures, and Constraints," *Phys. Rept.*, vol. 537, pp. 91–121, 2014.

[18] G. Bertone, D. Hooper, and J. Silk, "Particle dark matter: Evidence, candidates and constraints," *Phys. Rept.*, vol. 405, pp. 279–390, 2005.

[19] K. Kaneta, H.-S. Lee, and S. Yun, "Portal Connecting Dark Photons and Axions," *Phys. Rev. Lett.*, vol. 118, no. 10, p. 101802, 2017.

[20] D. Ejlli, "Axion mediated photon to dark photon mixing," *Eur. Phys. J. C*, vol. 78, no. 1, p. 63, 2018.

[21] K. Choi, S. Lee, H. Seong, and S. Yun, "Gamma-ray spectral modulations induced by photon-ALP-dark photon oscillations," *Phys. Rev. D*, vol. 101, no. 4, p. 043007, 2020.

[22] L. Marzola, M. Raidal, and F. R. Urban, "Oscillating Spin-2 Dark Matter," *Phys. Rev. D*, vol. 97, no. 2, p. 024010, 2018.

[23] D. P. Finkbeiner and N. Weiner, "Exciting Dark Matter and the INTEGRAL/SPI 511 keV signal," *Phys. Rev. D*, vol. 76, p. 083519, 2007.

[24] M. T. Ressell, "Limits to the radiative decay of the axion," *Phys. Rev. D*, vol. 44, pp. 3001–3020, 1991.

[25] M. Kamionkowski, "Diffuse gamma-rays from WIMP decay and annihilation," in *NATO Advanced Study Institute: The Gamma Ray Sky with Compton Gro and Sigma*, 4 1994.

[26] J. M. Overduin and P. S. Wesson, "Dark matter and background light," *Phys. Rept.*, vol. 402, pp. 267–406, 2004.

[27] S. Furlanetto, S. P. Oh, and F. Briggs, "Cosmology at Low Frequencies: The 21 cm Transition and the High-Redshift Universe," *Phys. Rept.*, vol. 433, pp. 181–301, 2006.

[28] M. F. Morales and J. S. B. Wyithe, "Reionization and Cosmology with 21 cm Fluctuations," *Ann. Rev. Astron. Astrophys.*, vol. 48, pp. 127–171, 2010.

[29] E. D. Kovetz *et al.*, "Line-Intensity Mapping: 2017 Status Report," 9 2017.

[30] K. Bandura *et al.*, "Canadian Hydrogen Intensity Mapping Experiment

(CHIME) Pathfinder," *Proc. SPIE Int. Soc. Opt. Eng.*, vol. 9145, p. 22, 2014.

[31] O. Doré *et al.*, "Cosmology with the SPHEREX All-Sky Spectral Survey," 12 2014.

[32] M. A. Bershady, M. T. Ressell, and M. S. Turner, "Telescope search for multi-eV axions," *Phys. Rev. Lett.*, vol. 66, pp. 1398–1401, 1991.

[33] D. Grin, G. Covone, J.-P. Kneib, M. Kamionkowski, A. Blain, and E. Jullo, "A Telescope Search for Decaying Relic Axions," *Phys. Rev. D*, vol. 75, p. 105018, 2007.

[34] Y. Gong, A. Cooray, K. Mitchell-Wynne, X. Chen, M. Zemcov, and J. Smidt, "Axion decay and anisotropy of near-IR extragalactic background light," *Astrophys. J.*, vol. 825, no. 2, p. 104, 2016.

[35] P. C. Breysse, E. D. Kovetz, and M. Kamionkowski, "Carbon Monoxide Intensity Mapping at Moderate Redshifts," *Mon. Not. Roy. Astron. Soc.*, vol. 443, no. 4, pp. 3506–3512, 2014.

[36] A. R. Pullen, O. Dore, and J. Bock, "Intensity Mapping across Cosmic Times with the $Ly\alpha$ Line," *Astrophys. J.*, vol. 786, p. 111, 2014.

[37] M. T. Ressell and M. S. Turner, "The Grand Unified Photon Spectrum:

A Coherent View of the Diffuse Extragalactic Background Radiation," *Comments Astrophys.*, vol. 14, p. 323, 1990.

[38] R. Hill, K. W. Masui, and D. Scott, "The Spectrum of the Universe," *Appl. Spectrosc.*, vol. 72, no. 5, pp. 663–688, 2018.

[39] "www.ccatobservatory.org," www.ccatobservatory.org.

[40] T. Y. Li, R. H. Wechsler, K. Devaraj, and S. E. Church, "Connecting CO Intensity Mapping to Molecular Gas and Star Formation in the Epoch of Galaxy Assembly," *Astrophys. J.*, vol. 817, no. 2, p. 169, 2016.

[41] A. Barlis, S. Hailey-Dunsheath, C. M. Bradford, C. McKenney, H. G. Le Duc, and J. Aguirre, "Development of low-noise kinetic inductance detectors for far-infrared astrophysics," in *APS April Meeting Abstracts*, ser. APS Meeting Abstracts, vol. 2017, Jan. 2017, p. R4.007.

[42] P. C. Breysse and M. Rahman, "Feeding cosmic star formation: Exploring high-redshift molecular gas with CO intensity mapping," *Mon. Not. Roy. Astron. Soc.*, vol. 468, no. 1, pp. 741–750, 2017.

[43] F. Chen, J. M. Cline, A. Fradette, A. R. Frey, and C. Rabideau, "Exciting dark matter in the galactic center," *Phys. Rev. D*, vol. 81, p. 043523, 2010.

[44] H. An, M. Pospelov, and J. Pradler, "Direct constraints on charged excitations of dark matter," *Phys. Rev. Lett.*, vol. 109, p. 251302, 2012.

[45] D. P. Finkbeiner and N. Weiner, "X-ray line from exciting dark matter," *Phys. Rev. D*, vol. 94, no. 8, p. 083002, 2016.

[46] H. Okada and T. Toma, "3.55 keV X-ray Line Signal from Excited Dark Matter in Radiative Neutrino Model," *Phys. Lett. B*, vol. 737, pp. 162–166, 2014.

[47] K. Schutz and T. R. Slatyer, "Self-Scattering for Dark Matter with an Excited State," *JCAP*, vol. 01, p. 021, 2015.

[48] A. Berlin, A. DiFranzo, and D. Hooper, "3.55 keV line from exciting dark matter without a hidden sector," *Phys. Rev. D*, vol. 91, no. 7, p. 075018, 2015.

[49] A. Hektor, G. Hütsi, L. Marzola, and V. Vaskonen, "Constraints on ALPs and excited dark matter from the EDGES 21-cm absorption signal," *Phys. Lett. B*, vol. 785, pp. 429–433, 2018.

[50] R. A. Monsalve, A. E. E. Rogers, J. D. Bowman, and T. J. Mozdzen, "Results from EDGES High-Band: I. Constraints on Phenomenological Models for the Global 21 cm Signal," *Astrophys. J.*, vol. 847, no. 1, p. 64, 2017.

[51] R. Barkana, "Possible interaction between baryons and dark-matter particles revealed by the first stars," *Nature*, vol. 555, no. 7694, pp. 71–74, 2018.

[52] H. Tashiro, K. Kadota, and J. Silk, "Effects of dark matter-baryon scattering on redshifted 21 cm signals," *Phys. Rev. D*, vol. 90, no. 8, p. 083522, 2014.

[53] J. B. Muñoz, E. D. Kovetz, and Y. Ali-Haïmoud, "Heating of Baryons due to Scattering with Dark Matter During the Dark Ages," *Phys. Rev. D*, vol. 92, no. 8, p. 083528, 2015.

[54] C. Dvorkin, K. Blum, and M. Kamionkowski, "Constraining Dark Matter-Baryon Scattering with Linear Cosmology," *Phys. Rev. D*, vol. 89, no. 2, p. 023519, 2014.

[55] W. L. Xu, C. Dvorkin, and A. Chael, "Probing sub-GeV Dark Matter-Baryon Scattering with Cosmological Observables," *Phys. Rev. D*, vol. 97, no. 10, p. 103530, 2018.

[56] T. R. Slatyer and C.-L. Wu, "Early-Universe constraints on dark matter-baryon scattering and their implications for a global 21 cm signal," *Phys. Rev. D*, vol. 98, no. 2, p. 023013, 2018.

[57] K. K. Boddy, V. Gluscevic, V. Poulin, E. D. Kovetz, M. Kamionkowski, and R. Barkana, "Critical assessment of CMB limits on dark matter-baryon scattering: New treatment of the relative bulk velocity," *Phys. Rev. D*, vol. 98, no. 12, p. 123506, 2018.

[58] E. G. Adelberger, B. R. Heckel, and A. E. Nelson, "Tests of the gravitational inverse square law," *Ann. Rev. Nucl. Part. Sci.*, vol. 53, pp. 77–121, 2003.

[59] J. G. Williams, S. G. Turyshev, and D. H. Boggs, "Progress in lunar laser ranging tests of relativistic gravity," *Phys. Rev. Lett.*, vol. 93, p. 261101, 2004.

[60] D. J. Kapner, T. S. Cook, E. G. Adelberger, J. H. Gundlach, B. R. Heckel, C. D. Hoyle, and H. E. Swanson, "Tests of the gravitational inverse-square law below the dark-energy length scale," *Phys. Rev. Lett.*, vol. 98, p. 021101, 2007.

[61] S. Schlamminger, K. Y. Choi, T. A. Wagner, J. H. Gundlach, and E. G. Adelberger, "Test of the equivalence principle using a rotating torsion balance," *Phys. Rev. Lett.*, vol. 100, p. 041101, 2008.

[62] J. Murata and S. Tanaka, "A review of short-range gravity experiments in the LHC era," *Class. Quant. Grav.*, vol. 32, no. 3, p. 033001, 2015.

[63] A. A. Prinz *et al.*, "Search for millicharged particles at SLAC," *Phys. Rev. Lett.*, vol. 81, pp. 1175–1178, 1998.

[64] S. Davidson, S. Hannestad, and G. Raffelt, "Updated bounds on millicharged particles," *JHEP*, vol. 05, p. 003, 2000.

[65] C. Boehm, M. J. Dolan, and C. McCabe, "A Lower Bound on the Mass of Cold Thermal Dark Matter from Planck," *JCAP*, vol. 08, p. 041, 2013.

[66] H. Vogel and J. Redondo, "Dark Radiation constraints on minicharged particles in models with a hidden photon," *JCAP*, vol. 02, p. 029, 2014.

[67] J. H. Chang, R. Essig, and S. D. McDermott, "Supernova 1987A Constraints on Sub-GeV Dark Sectors, Millicharged Particles, the QCD Axion, and an Axion-like Particle," *JHEP*, vol. 09, p. 051, 2018.

[68] J. B. Muñoz and A. Loeb, "A small amount of mini-charged dark matter could cool the baryons in the early Universe," *Nature*, vol. 557, no. 7707, p. 684, 2018.

[69] R. Barkana, N. J. Outmezguine, D. Redigolo, and T. Volansky, "Strong constraints on light dark matter interpretation of the EDGES signal," *Phys. Rev. D*, vol. 98, no. 10, p. 103005, 2018.

[70] A. Berlin, D. Hooper, G. Krnjaic, and S. D. McDermott, "Severely Constraining Dark Matter Interpretations of the 21-cm Anomaly," *Phys. Rev. Lett.*, vol. 121, no. 1, p. 011102, 2018.

[71] R. de Putter, O. Doré, J. Gleyzes, D. Green, and J. Meyers, "Dark Matter Interactions, Helium, and the Cosmic Microwave Background," *Phys. Rev. Lett.*, vol. 122, no. 4, p. 041301, 2019.

[72] E. D. Kovetz, V. Poulin, V. Gluscevic, K. K. Boddy, R. Barkana, and M. Kamionkowski, "Tighter limits on dark matter explanations of the anomalous EDGES 21 cm signal," *Phys. Rev. D*, vol. 98, no. 10, p. 103529, 2018.

[73] N. Aghanim *et al.*, "Planck 2018 results. VI. Cosmological parameters," *Astron. Astrophys.*, vol. 641, p. A6, 2020, [Erratum: Astron.Astrophys. 652, C4 (2021)].

[74] P. Gondolo and G. Gelmini, "Cosmic abundances of stable particles: Improved analysis," *Nucl. Phys. B*, vol. 360, pp. 145–179, 1991.

[75] G. Steigman, B. Dasgupta, and J. F. Beacom, "Precise Relic WIMP Abundance and its Impact on Searches for Dark Matter Annihilation," *Phys. Rev. D*, vol. 86, p. 023506, 2012.

[76] S. Borsanyi *et al.*, "Calculation of the axion mass based on high-temperature lattice quantum chromodynamics," *Nature*, vol. 539, no. 7627, pp. 69–71, 2016.

[77] D. E. Kaplan, G. Z. Krnjaic, K. R. Rehermann, and C. M. Wells, "Atomic Dark Matter," *JCAP*, vol. 05, p. 021, 2010.

[78] J. M. Cline, Z. Liu, and W. Xue, "Millicharged Atomic Dark Matter," *Phys. Rev. D*, vol. 85, p. 101302, 2012.

[79] F.-Y. Cyr-Racine and K. Sigurdson, "Cosmology of atomic dark matter," *Phys. Rev. D*, vol. 87, no. 10, p. 103515, 2013.

[80] M. Tanabashi *et al.*, "Review of Particle Physics," *Phys. Rev. D*, vol. 98, no. 3, p. 030001, 2018.

[81] A. A. Abdo *et al.*, "Observations of Milky Way Dwarf Spheroidal galaxies with the Fermi-LAT detector and constraints on Dark Matter models," *Astrophys. J.*, vol. 712, pp. 147–158, 2010.

[82] K. K. Boddy and J. Kumar, "Indirect Detection of Dark Matter Using MeV-Range Gamma-Ray Telescopes," *Phys. Rev. D*, vol. 92, no. 2, p. 023533, 2015.

[83] R. Bartels, D. Gaggero, and C. Weniger, "Prospects for indirect dark matter searches with MeV photons," *JCAP*, vol. 05, p. 001, 2017.

[84] M. Kawasaki, K. Kohri, and N. Sugiyama, "MeV scale reheating temperature and thermalization of neutrino background," *Phys. Rev. D*, vol. 62, p. 023506, 2000.

[85] A. Kudo and M. Yamaguchi, "Inflation with low reheat temperature and cosmological constraint on stable charged massive particles," *Phys. Lett. B*, vol. 516, pp. 151–155, 2001.

[86] K. Ichikawa, M. Kawasaki, and F. Takahashi, "The Oscillation effects

on thermalization of the neutrinos in the Universe with low reheating temperature," *Phys. Rev. D*, vol. 72, p. 043522, 2005.

[87] C. M. Gaskell and E. S. Klimek, "Variability of Active Galactic Nuclei from Optical to X-ray Regions," *Astronomical and Astrophysical Transactions*, vol. 22, no. 4-5, pp. 661–680, Aug. 2003.

[88] A. Lawrence, "Clues to the Structure of AGN Through Massive Variability Surveys," in *Astronomical Surveys and Big Data*, ser. Astronomical Society of the Pacific Conference Series, A. Mickaelian, A. Lawrence, and T. Magakian, Eds., vol. 505, Jun. 2016, p. 107.

[89] P. Padovani, D. M. Alexander, R. J. Assef, B. De Marco, P. Giommi, R. C. Hickox, G. T. Richards, V. Smolčić, E. Hatziminaoglou, V. Mainieri, and M. Salvato, "Active galactic nuclei: what's in a name?" , vol. 25, no. 1, p. 2, Aug. 2017.

[90] L. F. Sartori, K. Schawinski, B. Trakhtenbrot, N. Caplar, E. Treister, M. J. Koss, C. M. Urry, and C. E. Zhang, "A model for AGN variability on multiple time-scales," , vol. 476, no. 1, pp. L34–L38, May 2018.

[91] A. R. Green, I. M. McHardy, and H. J. Lehto, "On the nature of rapid X-ray variability in active galactic nuclei." , vol. 265, pp. 664–680, Dec. 1993.

[92] M. Gliozzi, W. Brinkmann, C. Räth, I. E. Papadakis, H. Negoro, and H. Scheingraber, "On the nature of X-ray variability in Ark 564," , vol. 391, pp. 875–886, Sep. 2002.

[93] W. Ishibashi and T. J. L. Courvoisier, "X-ray variability time scales in active galactic nuclei," , vol. 504, no. 1, pp. 61–66, Sep. 2009.

[94] S. Collier and B. M. Peterson, "Characteristic Ultraviolet/Optical Timescales in Active Galactic Nuclei," , vol. 555, no. 2, pp. 775–785, Jul. 2001.

[95] B. Czerny, "The Role of the Accretion Disk in AGN Variability," in *AGN Variability from X-Rays to Radio Waves*, ser. Astronomical Society of the Pacific Conference Series, C. M. Gaskell, I. M. McHardy, B. M. Peterson, and S. G. Sergeev, Eds., vol. 360, Dec. 2006, p. 265.

[96] P. Arévalo and P. Uttley, "Investigating a fluctuating-accretion model for the spectral-timing properties of accreting black hole systems," , vol. 367, no. 2, pp. 801–814, Apr. 2006.

[97] P. Uttley, R. Edelson, I. M. McHardy, B. M. Peterson, and A. Markowitz, "Correlated Long-Term Optical and X-Ray Variations in NGC 5548," , vol. 584, no. 2, pp. L53–L56, Feb. 2003.

[98] P. Arévalo, P. Uttley, P. Lira, E. Breedt, I. M. McHardy, and E. Churazov,

"Correlation and time delays of the X-ray and optical emission of the Seyfert Galaxy NGC 3783," , vol. 397, no. 4, pp. 2004–2014, Aug. 2009.

[99] I. M. McHardy, D. T. Cameron, T. Dwelly, S. Connolly, P. Lira, D. Emmanoulopoulos, J. Gelbord, E. Breedt, P. Arevalo, and P. Uttley, "Swift monitoring of NGC 5548: X-ray reprocessing and short-term UV/optical variability," , vol. 444, no. 2, pp. 1469–1474, Oct. 2014.

[100] B. Vazquez, P. Galianni, M. Richmond, A. Robinson, D. J. Axon, K. Horne, T. Almeyda, M. Fausnaugh, B. M. Peterson, M. Bottorff, J. Gallimore, M. Eltizur, H. Netzer, T. Storchi-Bergmann, A. Marconi, A. Capetti, D. Batcheldor, C. Buchanan, G. Stirpe, M. Kishimoto, C. Packham, E. Perez, C. Tadhunter, J. Upton, and V. Estrada-Carpenter, "Spitzer Space Telescope Measurements of Dust Reverberation Lags in the Seyfert 1 Galaxy NGC 6418," , vol. 801, no. 2, p. 127, Mar. 2015.

[101] C. G. Mundell, P. Ferruit, N. Nagar, and A. S. Wilson, "Radio Variability in Seyfert Nuclei," , vol. 703, no. 1, pp. 802–815, Sep. 2009.

[102] F. A. Aharonian, M. V. Barkov, and D. Khangulyan, "Scenarios for Ultrafast Gamma-Ray Variability in AGN," , vol. 841, no. 1, p. 61, May 2017.

[103] J. L. Ryan, A. Siemiginowska, M. A. Sobolewska, and J. Grindlay, "Characteristic Variability Timescales in the Gamma-Ray Power Spectra of Blazars," , vol. 885, no. 1, p. 12, Nov. 2019.

[104] B. Rajput, C. S. Stalin, and S. Rakshit, "Long term γ-ray variability of blazars," , vol. 634, p. A80, Feb. 2020.

[105] S. Kozłowski, C. S. Kochanek, D. Stern, M. L. N. Ashby, R. J. Assef, J. J. Bock, C. Borys, K. Brand, M. Brodwin, M. J. I. Brown, R. Cool, A. Cooray, S. Croft, A. Dey, P. R. Eisenhardt, A. Gonzalez, V. Gorjian, R. Griffith, N. Grogin, R. Ivison, J. Jacob, B. T. Jannuzi, A. Mainzer, L. Moustakas, H. Röttgering, N. Seymour, H. A. Smith, S. A. Stanford, J. R. Stauffer, I. S. Sullivan, W. van Breugel, S. P. Willner, and E. L. Wright, "Mid-infrared Variability from the Spitzer Deep Wide-field Survey," , vol. 716, no. 1, pp. 530–543, Jun. 2010.

[106] S. M. LaMassa, S. Cales, E. C. Moran, A. D. Myers, G. T. Richards, M. Eracleous, T. M. Heckman, L. Gallo, and C. M. Urry, "The Discovery of the First "Changing Look" Quasar: New Insights Into the Physics and Phenomenology of Active Galactic Nucleus," , vol. 800, no. 2, p. 144, Feb. 2015.

[107] C. L. MacLeod, N. P. Ross, A. Lawrence, M. Goad, K. Horne, W. Burgett, K. C. Chambers, H. Flewelling, K. Hodapp, N. Kaiser, E. Magnier, R. Wainscoat, and C. Waters, "A systematic search for changing-look quasars in SDSS," , vol. 457, no. 1, pp. 389–404, Mar. 2016.

[108] Q. Yang, X.-B. Wu, X. Fan, L. Jiang, I. McGreer, J. Shangguan, S. Yao,

B. Wang, R. Joshi, R. Green, F. Wang, X. Feng, Y. Fu, J. Yang, and Y. Liu, "Discovery of 21 New Changing-look AGNs in the Northern Sky," , vol. 862, no. 2, p. 109, Aug. 2018.

[109] LSST Science Collaboration, P. A. Abell, J. Allison, S. F. Anderson, J. R. Andrew, J. R. P. Angel, L. Armus, D. Arnett, S. J. Asztalos, T. S. Axelrod, S. Bailey, D. R. Ballantyne, J. R. Bankert, W. A. Barkhouse, J. D. Barr, L. F. Barrientos, A. J. Barth, J. G. Bartlett, A. C. Becker, J. Becla, T. C. Beers, J. P. Bernstein, R. Biswas, M. R. Blanton, J. S. Bloom, J. J. Bochanski, P. Boeshaar, K. D. Borne, M. Bradac, W. N. Brandt, C. R. Bridge, M. E. Brown, R. J. Brunner, J. S. Bullock, A. J. Burgasser, J. H. Burge, D. L. Burke, P. A. Cargile, S. Chandrasekharan, G. Chartas, S. R. Chesley, Y.-H. Chu, D. Cinabro, M. W. Claire, C. F. Claver, D. Clowe, A. J. Connolly, K. H. Cook, J. Cooke, A. Cooray, K. R. Covey, C. S. Culliton, R. de Jong, W. H. de Vries, V. P. Debattista, F. Delgado, I. P. Dell'Antonio, S. Dhital, R. Di Stefano, M. Dickinson, B. Dilday, S. G. Djorgovski, G. Dobler, C. Donalek, G. Dubois-Felsmann, J. Durech, A. Eliasdottir, M. Eracleous, L. Eyer, E. E. Falco, X. Fan, C. D. Fassnacht, H. C. Ferguson, Y. R. Fernandez, B. D. Fields, D. Finkbeiner, E. E. Figueroa, D. B. Fox, H. Francke, J. S. Frank, J. Frieman, S. Fromenteau, M. Furqan, G. Galaz, A. Gal-Yam, P. Garnavich, E. Gawiser, J. Geary, P. Gee, R. R. Gibson, K. Gilmore, E. A. Grace, R. F. Green, W. J.

Gressler, C. J. Grillmair, S. Habib, J. S. Haggerty, M. Hamuy, A. W. Harris, S. L. Hawley, A. F. Heavens, L. Hebb, T. J. Henry, E. Hileman, E. J. Hilton, K. Hoadley, J. B. Holberg, M. J. Holman, S. B. Howell, L. Infante, Z. Ivezic, S. H. Jacoby, B. Jain, R, Jedicke, M. J. Jee, J. Garrett Jernigan, S. W. Jha, K. V. Johnston, R. L. Jones, M. Juric, M. Kaasalainen, Styliani, Kafka, S. M. Kahn, N. A. Kaib, J. Kalirai, J. Kantor, M. M. Kasliwal, C. R. Keeton, R. Kessler, Z. Knezevic, A. Kowalski, V. L. Krabbendam, K. S. Krughoff, S. Kulkarni, S. Kuhlman, M. Lacy, S. Lepine, M. Liang, A. Lien, P. Lira, K. S. Long, S. Lorenz, J. M. Lotz, R. H. Lupton, J. Lutz, L. M. Macri, A. A. Mahabal, R. Mandelbaum, P. Marshall, M. May, P. M. McGehee, B. T. Meadows, A. Meert, A. Milani, C. J. Miller, M. Miller, D. Mills, D. Minniti, D. Monet, A. S. Mukadam, E. Nakar, D. R. Neill, J. A. Newman, S. Nikolaev, M. Nordby, P. O'Connor, M. Oguri, J. Oliver, S. S. Olivier, J. K. Olsen, K. Olsen, E. W. Olszewski, H. Oluseyi, N. D. Padilla, A. Parker, J. Pepper, J. R. Peterson, C. Petry, P. A. Pinto, J. L. Pizagno, B. Popescu, A. Prsa, V. Radcka, M. J. Raddick, A. Rasmussen, A. Rau, J. Rho, J. E. Rhoads, G. T. Richards, S. T. Ridgway, B. E. Robertson, R. Roskar, A. Saha, A. Sarajedini, E. Scannapieco, T. Schalk, R. Schindler, S. Schmidt, S. Schmidt, D. P. Schneider, G. Schumacher, R. Scranton, J. Sebag, L. G. Seppala, O. Shemmer, J. D. Simon, M. Sivertz, H. A. Smith, J. Allyn Smith, N. Smith, A. H. Spitz,

A. Stanford, K. G. Stassun, J. Strader, M. A. Strauss, C. W. Stubbs, D. W. Sweeney, A. Szalay, P. Szkody, M. Takada, P. Thorman, D. E. Trilling, V. Trimble, A. Tyson, R. Van Berg, D. Vanden Berk, J. VanderPlas, L. Verde, B. Vrsnak, L. M. Walkowicz, B. D. Wandelt, S. Wang, Y. Wang, M. Warner, R. H. Wechsler, A. A. West, O. Wiecha, B. F. Williams, B. Willman, D. Wittman, S. C. Wolff, W. M. Wood-Vasey, P. Wozniak, P. Young, A. Zentner, and H. Zhan, "LSST Science Book, Version 2.0," *arXiv e-prints*, p. arXiv:0912.0201, Dec. 2009.

[110] S. Kozłowski, C. S. Kochanek, A. Udalski, Ł. Wyrzykowski, I. Soszyński, M. K. Szymański, M. Kubiak, G. Pietrzyński, O. Szewczyk, K. Ulaczyk, R. Poleski, and OGLE Collaboration, "Quantifying Quasar Variability as Part of a General Approach to Classifying Continuously Varying Sources," , vol. 708, no. 2, pp. 927–945, Jan. 2010.

[111] C. M. Peters, G. T. Richards, A. D. Myers, M. A. Strauss, K. B. Schmidt, Ž. Ivezić, N. P. Ross, C. L. MacLeod, and R. Riegel, "Quasar Classification Using Color and Variability," , vol. 811, no. 2, p. 95, Oct. 2015.

[112] N. R. Butler and J. S. Bloom, "Optimal Time-series Selection of Quasars," , vol. 141, no. 3, p. 93, Mar. 2011.

[113] Y. Choi, R. R. Gibson, A. C. Becker, Ž. Ivezić, A. J. Connolly, C. L. MacLeod, J. J. Ruan, and S. F. Anderson, "Variability-based Active Galac-

tic Nucleus Selection Using Image Subtraction in the SDSS and LSST Era," , vol. 782, no. 1, p. 37, Feb. 2014.

[114] N. Palanque-Delabrouille, C. Magneville, C. Yèche, I. Pâris, P. Petitjean, E. Burtin, K. Dawson, I. McGreer, A. D. Myers, G. Rossi, D. Schlegel, D. Schneider, A. Streblyanska, and J. Tinker, "The extended Baryon Oscillation Spectroscopic Survey: Variability selection and quasar luminosity function," , vol. 587, p. A41, Mar. 2016.

[115] P. Sánchez-Sáez, P. Lira, R. Cartier, N. Miranda, L. C. Ho, P. Arévalo, F. E. Bauer, P. Coppi, and C. Yovaniniz, "The QUEST-La Silla AGN Variability Survey: Selection of AGN Candidates through Optical Variability," , vol. 242, no. 1, p. 10, May 2019.

[116] D. De Cicco, F. E. Bauer, M. Paolillo, S. Cavuoti, P. Sánchez-Sáez, W. N. Brandt, G. Pignata, M. Vaccari, and M. Radovich, "A random forest-based selection of optically variable AGN in the VST-COSMOS field," , vol. 645, p. A103, Jan. 2021.

[117] C. M. Gaskell and A. J. Benker, "AGN Reddening and Ultraviolet Extinction Curves from Hubble Space Telescope Spectra," *arXiv e-prints*, p. arXiv:0711.1013, Nov. 2007.

[118] P. Uttley, I. M. McHardy, and S. Vaughan, "Non-linear X-ray variability

in X-ray binaries and active galaxies," , vol. 359, no. 1, pp. 345–362, May 2005.

[119] B. C. Kelly, M. Sobolewska, and A. Siemiginowska, "A Stochastic Model for the Luminosity Fluctuations of Accreting Black Holes," , vol. 730, no. 1, p. 52, Mar. 2011.

[120] C. L. MacLeod, Ž. Ivezić, C. S. Kochanek, S. Kozłowski, B. Kelly, E. Bullock, A. Kimball, B. Sesar, D. Westman, K. Brooks, R. Gibson, A. C. Becker, and W. H. de Vries, "Modeling the Time Variability of SDSS Stripe 82 Quasars as a Damped Random Walk," , vol. 721, no. 2, pp. 1014–1033, Oct. 2010.

[121] C. L. MacLeod, Ž. Ivezić, B. Sesar, W. de Vries, C. S. Kochanek, B. C. Kelly, A. C. Becker, R. H. Lupton, P. B. Hall, G. T. Richards, S. F. Anderson, and D. P. Schneider, "A Description of Quasar Variability Measured Using Repeated SDSS and POSS Imaging," , vol. 753, no. 2, p. 106, Jul. 2012.

[122] Y. Zu, C. S. Kochanek, S. Kozłowski, and A. Udalski, "Is Quasar Optical Variability a Damped Random Walk?" , vol. 765, no. 2, p. 106, Mar. 2013.

[123] S. Kozłowski, "A degeneracy in DRW modelling of AGN light curves," , vol. 459, no. 3, pp. 2787–2789, Jul. 2016.

[124] ——, "Limitations on the recovery of the true AGN variability parameters using damped random walk modeling," , vol. 597, p. A128, Jan. 2017.

[125] V. P. Kasliwal, M. S. Vogeley, and G. T. Richards, "Are the variability properties of the Kepler AGN light curves consistent with a damped random walk?" , vol. 451, no. 4, pp. 4328–4345, Aug. 2015.

[126] K. L. Smith, R. F. Mushotzky, P. T. Boyd, M. Malkan, S. B. Howell, and D. M. Gelino, "The Kepler Light Curves of AGN: A Detailed Analysis," , vol. 857, no. 2, p. 141, Apr. 2018.

[127] O. González-Martín and S. Vaughan, "X-ray variability of 104 active galactic nuclei. XMM-Newton power-spectrum density profiles," , vol. 544, p. A80, Aug. 2012.

[128] S. Kozłowski, "A Method to Measure the Unbiased Decorrelation Timescale of the AGN Variable Signal from Structure Functions," , vol. 835, no. 2, p. 250, Feb. 2017.

[129] L. F. Sartori, B. Trakhtenbrot, K. Schawinski, N. Caplar, E. Treister, and C. Zhang, "A Forward Modeling Approach to AGN Variability–Method Description and Early Applications," , vol. 883, no. 2, p. 139, Oct. 2019.

[130] V. P. Kasliwal, M. S. Vogeley, and G. T. Richards, "Extracting information from AGN variability," , vol. 470, no. 3, pp. 3027–3048, Sep. 2017.

[131] C. J. Burke, Y. Shen, O. Blaes, C. F. Gammie, K. Horne, Y.-F. Jiang, X. Liu, I. M. McHardy, C. W. Morgan, S. Scaringi, and Q. Yang, "A characteristic optical variability time scale in astrophysical accretion disks," *Science*, vol. 373, no. 6556, pp. 789–792, Aug. 2021.

[132] Ž. Ivezić and C. MacLeod, "Optical variability of quasars: a damped random walk," in *Multiwavelength AGN Surveys and Studies*, A. M. Mickaelian and D. B. Sanders, Eds., vol. 304, Jul. 2014, pp. 395–398.

[133] P. F. Hopkins, G. T. Richards, and L. Hernquist, "An Observational Determination of the Bolometric Quasar Luminosity Function," , vol. 654, no. 2, pp. 731–753, Jan. 2007.

[134] T. Araki, F. Kaneko, Y. Konishi, T. Ota, J. Sato, and T. Shimomura, "Cosmic neutrino spectrum and the muon anomalous magnetic moment in the gauged $L_{\hat{I}\mathbb{E}-L_{\check{I}}}$ model," *Phys. Rev. D*, vol. 91, no. 3, p. 037301, 2015.

[135] T. Araki, F. Kaneko, T. Ota, J. Sato, and T. Shimomura, "MeV scale leptonic force for cosmic neutrino spectrum and muon anomalous magnetic moment," *Phys. Rev. D*, vol. 93, no. 1, p. 013014, 2016.

[136] G. Barenboim, P. B. Denton, and I. M. Oldengott, "Constraints on inflation with an extended neutrino sector," *Phys. Rev. D*, vol. 99, no. 8, p. 083515, 2019.

[137] B. J. P. Jones and J. Spitz, "Neutrino Flavor Transformations from New Short-Range Forces," 11 2019.

[138] *Neutrino Non-Standard Interactions: A Status Report*, vol. 2, 2019.

[139] J. F. Beacom, "The Diffuse Supernova Neutrino Background," *Ann. Rev. Nucl. Part. Sci.*, vol. 60, pp. 439–462, 2010.

[140] S. Ando, J. F. Beacom, and H. Yuksel, "Detection of neutrinos from supernovae in nearby galaxies," *Phys. Rev. Lett.*, vol. 95, p. 171101, 2005.

[141] S. Böser, M. Kowalski, L. Schulte, N. L. Strotjohann, and M. Voge, "Detecting extra-galactic supernova neutrinos in the Antarctic ice," *Astropart. Phys.*, vol. 62, pp. 54–65, 2015.

[142] S. Horiuchi, J. F. Beacom, and E. Dwek, "The Diffuse Supernova Neutrino Background is detectable in Super-Kamiokande," *Phys. Rev. D*, vol. 79, p. 083013, 2009.

[143] K. Ioka and K. Murase, "IceCube PeV–EeV neutrinos and secret interactions of neutrinos," *PTEP*, vol. 2014, no. 6, p. 061E01, 2014.

[144] I. M. Shoemaker and K. Murase, "Probing BSM Neutrino Physics with Flavor and Spectral Distortions: Prospects for Future High-Energy Neutrino Telescopes," *Phys. Rev. D*, vol. 93, no. 8, p. 085004, 2016.

[145] S. Shalgar, I. Tamborra, and M. Bustamante, "Core-collapse supernovae stymie secret neutrino interactions," *Phys. Rev. D*, vol. 103, no. 12, p. 123008, 2021.

[146] J. Baker, H. Goldberg, G. Perez, and I. Sarcevic, "Probing late neutrino mass properties with supernova neutrinos," *Phys. Rev. D*, vol. 76, p. 063004, 2007.

[147] M. Uehara, "A Unitarized chiral approach to f(0)(980) and a(0)(980) states and nature of light scalar resonances," 4 2004.

[148] K. Blum, A. Hook, and K. Murase, "High energy neutrino telescopes as a probe of the neutrino mass mechanism," 8 2014.

[149] K. C. Y. Ng and J. F. Beacom, "Cosmic neutrino cascades from secret neutrino interactions," *Phys. Rev. D*, vol. 90, no. 6, p. 065035, 2014, [Erratum: Phys.Rev.D 90, 089904 (2014)].

[150] M. Bustamante, C. Rosenstrøm, S. Shalgar, and I. Tamborra, "Bounds on secret neutrino interactions from high-energy astrophysical neutrinos," *Phys. Rev. D*, vol. 101, no. 12, p. 123024, 2020.

[151] Y. Farzan and S. Palomares-Ruiz, "Dips in the Diffuse Supernova Neutrino Background," *JCAP*, vol. 06, p. 014, 2014.

[152] M. Ibe and K. Kaneta, "Cosmic neutrino background absorption line in

the neutrino spectrum at IceCube," *Phys. Rev. D*, vol. 90, no. 5, p. 053011, 2014.

[153] Y. S. Jeong, S. Palomares-Ruiz, M. H. Reno, and I. Sarcevic, "Probing secret interactions of eV-scale sterile neutrinos with the diffuse supernova neutrino background," *JCAP*, vol. 06, p. 019, 2018.

[154] Y. Ema, R. Jinno, and T. Moroi, "Cosmic-Ray Neutrinos from the Decay of Long-Lived Particle and the Recent IceCube Result," *Phys. Lett. B*, vol. 733, pp. 120–125, 2014.

[155] K. V. Berghaus, M. D. Diamond, and D. E. Kaplan, "Decays of Long-Lived Relics and Their Signatures at IceCube," *JHEP*, vol. 05, p. 145, 2019.

[156] K. Bays *et al.*, "Supernova Relic Neutrino Search at Super-Kamiokande," *Phys. Rev. D*, vol. 85, p. 052007, 2012.

[157] N. Blinov, K. J. Kelly, G. Z. Krnjaic, and S. D. McDermott, "Constraining the Self-Interacting Neutrino Interpretation of the Hubble Tension," *Phys. Rev. Lett.*, vol. 123, no. 19, p. 191102, 2019.

[158] M. Berbig, S. Jana, and A. Trautner, "The Hubble tension and a renormalizable model of gauged neutrino self-interactions," *Phys. Rev. D*, vol. 102, no. 11, p. 115008, 2020.

[159] C. Athanassopoulos *et al.*, "Candidate events in a search for anti-muon-neutrino —> anti-electron-neutrino oscillations," *Phys. Rev. Lett.*, vol. 75, pp. 2650–2653, 1995.

[160] ——, "Evidence for anti-muon-neutrino —> anti-electron-neutrino oscillations from the LSND experiment at LAMPF," *Phys. Rev. Lett.*, vol. 77, pp. 3082–3085, 1996.

[161] ——, "Evidence for neutrino oscillations from muon decay at rest," *Phys. Rev. C*, vol. 54, pp. 2685–2708, 1996.

[162] A. Aguilar-Arevalo *et al.*, "Evidence for neutrino oscillations from the observation of $\bar{\nu}_e$ appearance in a $\bar{\nu}_\mu$ beam," *Phys. Rev. D*, vol. 64, p. 112007, 2001.

[163] A. A. Aguilar-Arevalo *et al.*, "A Search for Electron Neutrino Appearance at the $\Delta m^2 \sim 1eV^2$ Scale," *Phys. Rev. Lett.*, vol. 98, p. 231801, 2007.

[164] ——, "Event Excess in the MiniBooNE Search for $\bar{\nu}_\mu \to \bar{\nu}_e$ Oscillations," *Phys. Rev. Lett.*, vol. 105, p. 181801, 2010.

[165] ——, "Improved Search for $\bar{\nu}_\mu \to \bar{\nu}_e$ Oscillations in the MiniBooNE Experiment," *Phys. Rev. Lett.*, vol. 110, p. 161801, 2013.

[166] G. Mention, M. Fechner, T. Lasserre, T. A. Mueller, D. Lhuillier, M. Cri-

bier, and A. Letourneau, "The Reactor Antineutrino Anomaly," *Phys. Rev. D*, vol. 83, p. 073006, 2011.

[167] A. A. Aguilar-Arevalo *et al.*, "Significant Excess of ElectronLike Events in the MiniBooNE Short-Baseline Neutrino Experiment," *Phys. Rev. Lett.*, vol. 121, no. 22, p. 221801, 2018.

[168] B. Dasgupta and J. Kopp, "Cosmologically Safe eV-Scale Sterile Neutrinos and Improved Dark Matter Structure," *Phys. Rev. Lett.*, vol. 112, no. 3, p. 031803, 2014.

[169] S. Hannestad, R. S. Hansen, and T. Tram, "How Self-Interactions can Reconcile Sterile Neutrinos with Cosmology," *Phys. Rev. Lett.*, vol. 112, no. 3, p. 031802, 2014.

[170] S. K. Agarwalla, S. S. Chatterjee, and A. Palazzo, "Signatures of a Light Sterile Neutrino in T2HK," *JHEP*, vol. 04, p. 091, 2018.

[171] C. Giganti, S. Lavignac, and M. Zito, "Neutrino oscillations: The rise of the PMNS paradigm," *Prog. Part. Nucl. Phys.*, vol. 98, pp. 1–54, 2018.

[172] C. Giunti and M. Laveder, "Neutrino mixing," 10 2003.

[173] I. Esteban, M. C. Gonzalez-Garcia, A. Hernandez-Cabezudo, M. Maltoni, and T. Schwetz, "Global analysis of three-flavour neutrino oscillations:

synergies and tensions in the determination of θ_{23}, δ_{CP}, and the mass ordering," *JHEP*, vol. 01, p. 106, 2019.

[174] S. Ando and K. Sato, "Relic neutrino background from cosmological supernovae," *New J. Phys.*, vol. 6, p. 170, 2004.

[175] K. Kotake, K. Sato, and K. Takahashi, "Explosion mechanism, neutrino burst, and gravitational wave in core-collapse supernovae," *Rept. Prog. Phys.*, vol. 69, pp. 971–1144, 2006.

[176] J. F. Beacom and M. R. Vagins, "GADZOOKS! Anti-neutrino spectroscopy with large water Cherenkov detectors," *Phys. Rev. Lett.*, vol. 93, p. 171101, 2004.

[177] C. Simpson *et al.*, "Sensitivity of Super-Kamiokande with Gadolinium to Low Energy Anti-neutrinos from Pre-supernova Emission," *Astrophys. J.*, vol. 885, p. 133, 2019.

[178] A. Strumia and F. Vissani, "Precise quasielastic neutrino/nucleon cross-section," *Phys. Lett. B*, vol. 564, pp. 42–54, 2003.

[179] R. Laha, J. F. Beacom, B. Dasgupta, S. Horiuchi, and K. Murase, "Demystifying the PeV Cascades in IceCube: Less (Energy) is More (Events)," *Phys. Rev. D*, vol. 88, p. 043009, 2013.

[180] M. G. Aartsen *et al.*, "Evidence for High-Energy Extraterrestrial Neutrinos at the IceCube Detector," *Science*, vol. 342, p. 1242856, 2013.

[181] C. Lunardini and I. Tamborra, "Diffuse supernova neutrinos: oscillation effects, stellar cooling and progenitor mass dependence," *JCAP*, vol. 07, p. 012, 2012.

[182] K. Møller, A. M. Suliga, I. Tamborra, and P. B. Denton, "Measuring the supernova unknowns at the next-generation neutrino telescopes through the diffuse neutrino background," *JCAP*, vol. 05, p. 066, 2018.

[183] J. Stettner, "Measurement of the Diffuse Astrophysical Muon-Neutrino Spectrum with Ten Years of IceCube Data," *PoS*, vol. ICRC2019, p. 1017, 2020.

[184] R. Abbasi *et al.*, "The IceCube high-energy starting event sample: Description and flux characterization with 7.5 years of data," *Phys. Rev. D*, vol. 104, p. 022002, 2021.

[185] ——, "IceCube Data for Neutrino Point-Source Searches Years 2008-2018," 1 2021.

[186] M. G. Aartsen *et al.*, "Neutrino emission from the direction of the blazar TXS 0506+056 prior to the IceCube-170922A alert," *Science*, vol. 361, no. 6398, pp. 147–151, 2018.

[187] ——, "Multimessenger observations of a flaring blazar coincident with high-energy neutrino IceCube-170922A," *Science*, vol. 361, no. 6398, p. eaat1378, 2018.

[188] T. Glüsenkamp, "Analysis of the cumulative neutrino flux from Fermi-LAT blazar populations using 3 years of IceCube data," *EPJ Web Conf.*, vol. 121, p. 05006, 2016.

[189] A. Palladino and F. Vissani, "Can BL Lacertae emission explain the neutrinos above 0.2 PeV?" *Astron. Astrophys.*, vol. 604, p. A18, 2017.

[190] K. Murase, F. Oikonomou, and M. Petropoulou, "Blazar Flares as an Origin of High-Energy Cosmic Neutrinos?" *Astrophys. J.*, vol. 865, no. 2, p. 124, 2018.

[191] C. Yuan, K. Murase, and P. Mészáros, "Complementarity of Stacking and Multiplet Constraints on the Blazar Contribution to the Cumulative High-Energy Neutrino Intensity," *Astrophys. J.*, vol. 890, p. 25, 2020.

[192] D. Smith, D. Hooper, and A. Vieregg, "Revisiting AGN as the source of IceCube's diffuse neutrino flux," *JCAP*, vol. 03, p. 031, 2021.

[193] B. Zhou, M. Kamionkowski, and Y.-f. Liang, "Search for High-Energy Neutrino Emission from Radio-Bright AGN," *Phys. Rev. D*, vol. 103, no. 12, p. 123018, 2021.

[194] S. Adrian-Martinez *et al.*, "Letter of intent for KM3NeT 2.0," *J. Phys. G*, vol. 43, no. 8, p. 084001, 2016.

[195] A. D. Avrorin *et al.*, "Baikal-GVD: status and prospects," *EPJ Web Conf.*, vol. 191, p. 01006, 2018.

[196] K. Murase, M. Ahlers, and B. C. Lacki, "Testing the Hadronuclear Origin of PeV Neutrinos Observed with IceCube," *Phys. Rev. D*, vol. 88, no. 12, p. 121301, 2013.

[197] R.-Y. Liu, K. Wang, R. Xue, A. M. Taylor, X.-Y. Wang, Z. Li, and H. Yan, "Hadronuclear interpretation of a high-energy neutrino event coincident with a blazar flare," *Phys. Rev. D*, vol. 99, no. 6, p. 063008, 2019.

[198] J. P. Rachen and P. Meszaros, "Photohadronic neutrinos from transients in astrophysical sources," *Phys. Rev. D*, vol. 58, p. 123005, 1998.

[199] W. Winter, "Photohadronic Origin of the TeV-PeV Neutrinos Observed in IceCube," *Phys. Rev. D*, vol. 88, p. 083007, 2013.

[200] J. C. Rodríguez-Ramírez, E. M. de Gouveia Dal Pino, and R. Alves Batista, "Very-high-energy Emission from Magnetic Reconnection in the Radiative-inefficient Accretion Flow of SgrA," *Astrophys. J.*, vol. 879, no. 1, p. 6, 2019.

[201] T. Inoue, "Bell-Instability-Mediated Spectral Modulation of Hadronic

Gamma Rays from a Supernova Remnant Interacting with a Molecular Cloud," *Astrophys. J.*, vol. 872, no. 1, p. 46, 2019.

[202] S. S. Kimura, K. Murase, and P. Mészáros, "Soft gamma rays from low accreting supermassive black holes and connection to energetic neutrinos," *Nature Commun.*, vol. 12, no. 1, p. 5615, 2021.

[203] K. Mannheim, "High-energy neutrinos from extragalactic jets," *Astropart. Phys.*, vol. 3, pp. 295–302, 1995.

[204] K. Murase, Y. Inoue, and C. D. Dermer, "Diffuse Neutrino Intensity from the Inner Jets of Active Galactic Nuclei: Impacts of External Photon Fields and the Blazar Sequence," *Phys. Rev. D*, vol. 90, no. 2, p. 023007, 2014.

[205] F. Tavecchio, C. Righi, A. Capetti, P. Grandi, and G. Ghisellini, "High-energy neutrinos from FR0 radio-galaxies?" *Mon. Not. Roy. Astron. Soc.*, vol. 475, no. 4, pp. 5529–5534, 2018.

[206] F. W. Stecker and M. H. Salamon, "High-energy neutrinos from quasars," *Space Sci. Rev.*, vol. 75, pp. 341–355, 1996.

[207] K. Murase, S. S. Kimura, and P. Meszaros, "Hidden Cores of Active Galactic Nuclei as the Origin of Medium-Energy Neutrinos: Critical

Tests with the MeV Gamma-Ray Connection," *Phys. Rev. Lett.*, vol. 125, no. 1, p. 011101, 2020.

[208] Y. Inoue, D. Khangulyan, and A. Doi, "On the Origin of High-energy Neutrinos from NGC 1068: The Role of Nonthermal Coronal Activity," *Astrophys. J. Lett.*, vol. 891, no. 2, p. L33, 2020.

[209] E. M. Gutiérrez, F. L. Vieyro, and G. E. Romero, "Nonthermal processes in hot accretion flows onto supermassive black holes: An inhomogeneous model," *Astron. Astrophys.*, vol. 649, p. A87, 2021.

[210] Y. Inoue, D. Khangulyan, and A. Doi, "Gamma-ray and Neutrino Signals from Accretion Disk Coronae of Active Galactic Nuclei," *Galaxies*, vol. 9, no. 2, p. 36, 2021.

[211] N. Senno, K. Murase, and P. Meszaros, "Choked Jets and Low-Luminosity Gamma-Ray Bursts as Hidden Neutrino Sources," *Phys. Rev. D*, vol. 93, no. 8, p. 083003, 2016.

[212] K. Murase, S. S. Kimura, B. T. Zhang, F. Oikonomou, and M. Petropoulou, "High-Energy Neutrino and Gamma-Ray Emission from Tidal Disruption Events," *Astrophys. J.*, vol. 902, no. 2, p. 108, 2020.

[213] N. Senno, K. Murase, and P. Mészáros, "Constraining high-energy neu-

trino emission from choked jets in stripped-envelope supernovae," *JCAP*, vol. 01, p. 025, 2018.

[214] A. Esmaili and K. Murase, "Constraining high-energy neutrinos from choked-jet supernovae with IceCube high-energy starting events," *JCAP*, vol. 12, p. 008, 2018.

[215] J. Necker *et al.*, "Searching for High-Energy Neutrinos from Core-Collapse Supernovae with IceCube," *PoS*, vol. ICRC2021, p. 1116, 2021.

[216] C. Lunardini and E. Sabancilar, "Cosmic Strings as Emitters of Extremely High Energy Neutrinos," *Phys. Rev. D*, vol. 86, p. 085008, 2012.

[217] L. A. Anchordoqui, T. C. Paul, L. H. M. da Silva, D. F. Torres, and B. J. Vlcek, "What IceCube data tell us about neutrino emission from star-forming galaxies (so far)," *Phys. Rev. D*, vol. 89, no. 12, p. 127304, 2014.

[218] P. Padovani and E. Resconi, "Are both BL Lacs and pulsar wind nebulae the astrophysical counterparts of IceCube neutrino events?" *Mon. Not. Roy. Astron. Soc.*, vol. 443, no. 1, pp. 474–484, 2014.

[219] S. Sahu and L. S. Miranda, "Some possible sources of IceCube TeV–PeV neutrino events," *Eur. Phys. J. C*, vol. 75, p. 273, 2015.

[220] R. Moharana and S. Razzaque, "Angular correlation of cosmic neutrinos

with ultrahigh-energy cosmic rays and implications for their sources," *JCAP*, vol. 08, p. 014, 2015.

[221] K. Emig, C. Lunardini, and R. Windhorst, "Do high energy astrophysical neutrinos trace star formation?" *JCAP*, vol. 12, p. 029, 2015.

[222] S. Ando, I. Tamborra, and F. Zandanel, "Tomographic Constraints on High-Energy Neutrinos of Hadronuclear Origin," *Phys. Rev. Lett.*, vol. 115, no. 22, p. 221101, 2015.

[223] M. G. Aartsen *et al.*, "Time-Integrated Neutrino Source Searches with 10 Years of IceCube Data," *Phys. Rev. Lett.*, vol. 124, no. 5, p. 051103, 2020.

[224] A. Plavin, Y. Y. Kovalev, Y. A. Kovalev, and S. Troitsky, "Observational Evidence for the Origin of High-energy Neutrinos in Parsec-scale Nuclei of Radio-bright Active Galaxies," *Astrophys. J.*, vol. 894, no. 2, p. 101, 2020.

[225] K. Fang, A. Banerjee, E. Charles, and Y. Omori, "A Cross-Correlation Study of High-energy Neutrinos and Tracers of Large-Scale Structure," *Astrophys. J.*, vol. 894, no. 2, p. 112, 2020.

[226] R. Abbasi *et al.*, "A search for neutrino emission from cores of Active Galactic Nuclei," 11 2021.

[227] ——, "Time-Integrated Searches for Point-like Sources of Neutrinos with the 40-String IceCube Detector," *Astrophys. J.*, vol. 732, p. 18, 2011.

[228] M. G. Aartsen *et al.*, "Search for Time-independent Neutrino Emission from Astrophysical Sources with 3 yr of IceCube Data," *Astrophys. J.*, vol. 779, p. 132, 2013.

[229] J. Braun, J. Dumm, F. De Palma, C. Finley, A. Karle, and T. Montaruli, "Methods for point source analysis in high energy neutrino telescopes," *Astropart. Phys.*, vol. 29, pp. 299–305, 2008.

[230] J. Braun, M. Baker, J. Dumm, C. Finley, A. Karle, and T. Montaruli, "Time-Dependent Point Source Search Methods in High Energy Neutrino Astronomy," *Astropart. Phys.*, vol. 33, pp. 175–181, 2010.

[231] C. Creque-Sarbinowski, M. Kamionkowski, and B. Zhou, "AGN variability in the age of VRO," 10 2021.

[232] C. Creque-Sarbinowski, J. Hyde, and M. Kamionkowski, "Resonant neutrino self-interactions," *Phys. Rev. D*, vol. 103, no. 2, p. 023527, 2021.

[233] S. Koren, "Neutrino – Dark Matter Scattering and Coincident Detections of UHE Neutrinos with EM Sources," *JCAP*, vol. 09, p. 013, 2019.

[234] K. Murase and I. M. Shoemaker, "Neutrino Echoes from Multimessenger Transient Sources," *Phys. Rev. Lett.*, vol. 123, no. 24, p. 241102, 2019.

[235] A. Schneider, "Characterization of the Astrophysical Diffuse Neutrino Flux with IceCube High-Energy Starting Events," *PoS*, vol. ICRC2019, p. 1004, 2020.

[236] E. Waxman and J. N. Bahcall, "High-energy neutrinos from cosmological gamma-ray burst fireballs," *Phys. Rev. Lett.*, vol. 78, pp. 2292–2295, 1997.

[237] R. Abbasi *et al.*, "Search for muon neutrinos from Gamma-Ray Bursts with the IceCube neutrino telescope," *Astrophys. J.*, vol. 710, pp. 346–359, 2010.

[238] ——, "Limits on Neutrino Emission from Gamma-Ray Bursts with the 40 String IceCube Detector," *Phys. Rev. Lett.*, vol. 106, p. 141101, 2011.

[239] ——, "An absence of neutrinos associated with cosmic-ray acceleration in γ-ray bursts," *Nature*, vol. 484, pp. 351–353, 2012.

[240] M. G. Aartsen *et al.*, "Search for Prompt Neutrino Emission from Gamma-Ray Bursts with IceCube," *Astrophys. J. Lett.*, vol. 805, no. 1, p. L5, 2015.

[241] ——, "An All-Sky Search for Three Flavors of Neutrinos from Gamma-Ray Bursts with the IceCube Neutrino Observatory," *Astrophys. J.*, vol. 824, no. 2, p. 115, 2016.

[242] ——, "Extending the search for muon neutrinos coincident with gamma-ray bursts in IceCube data," *Astrophys. J.*, vol. 843, no. 2, p. 112, 2017.

[243] ——, "The contribution of Fermi-2LAC blazars to the diffuse TeV-PeV neutrino flux," *Astrophys. J.*, vol. 835, no. 1, p. 45, 2017.

[244] D. Hooper, T. Linden, and A. Vieregg, "Active Galactic Nuclei and the Origin of IceCube's Diffuse Neutrino Flux," *JCAP*, vol. 02, p. 012, 2019.

[245] A. V. Plavin, Y. Y. Kovalev, Y. A. Kovalev, and S. V. Troitsky, "Directional Association of TeV to PeV Astrophysical Neutrinos with Radio Blazars," *Astrophys. J.*, vol. 908, no. 2, p. 157, 2021.

[246] M. G. Aartsen *et al.*, "IceCube Search for High-Energy Neutrino Emission from TeV Pulsar Wind Nebulae," *Astrophys. J.*, vol. 898, no. 2, p. 117, 2020.

[247] ——, "IceCube-Gen2: the window to the extreme Universe," *J. Phys. G*, vol. 48, no. 6, p. 060501, 2021.

[248] J. M. Hyde, A. J. Long, and T. Vachaspati, "Dark Strings and their Couplings to the Standard Model," *Phys. Rev. D*, vol. 89, p. 065031, 2014.

[249] A. J. Long, J. M. Hyde, and T. Vachaspati, "Cosmic Strings in Hidden Sectors: 1. Radiation of Standard Model Particles," *JCAP*, vol. 09, p. 030, 2014.

[250] A. J. Long and T. Vachaspati, "Cosmic Strings in Hidden Sectors: 2. Cosmological and Astrophysical Signatures," *JCAP*, vol. 12, p. 040, 2014.

[251] T. Vachaspati and A. Vilenkin, "Gravitational Radiation from Cosmic Strings," *Phys. Rev. D*, vol. 31, p. 3052, 1985.

[252] M. Hindmarsh, "Gravitational radiation from kinky infinite strings," *Phys. Lett. B*, vol. 251, pp. 28–33, 1990.

[253] B. Allen and E. P. S. Shellard, "Gravitational radiation from cosmic strings," *Phys. Rev. D*, vol. 45, pp. 1898–1912, 1992.

[254] T. Vachaspati, "Cosmic Rays from Cosmic Strings with Condensates," *Phys. Rev. D*, vol. 81, p. 043531, 2010.

[255] T. Damour and A. Vilenkin, "Gravitational wave bursts from cusps and kinks on cosmic strings," *Phys. Rev. D*, vol. 64, p. 064008, 2001.

[256] P. Auclair, D. A. Steer, and T. Vachaspati, "Particle emission and gravitational radiation from cosmic strings: observational constraints," *Phys. Rev. D*, vol. 101, no. 8, p. 083511, 2020.

[257] K. Jones-Smith, H. Mathur, and T. Vachaspati, "Aharonov-Bohm Radiation," *Phys. Rev. D*, vol. 81, p. 043503, 2010.

[258] M. G. Alford and F. Wilczek, "Aharonov-Bohm Interaction of Cosmic Strings with Matter," *Phys. Rev. Lett.*, vol. 62, p. 1071, 1989.

[259] V. Berezinsky and M. Kachelriess, "Monte Carlo simulation for jet fragmentation in SUSY QCD," *Phys. Rev. D*, vol. 63, p. 034007, 2001.

[260] S. Sarkar and R. Toldra, "The High-energy cosmic ray spectrum from relic particle decay," *Nucl. Phys. B*, vol. 621, pp. 495–520, 2002.

[261] C. Barbot and M. Drees, "Detailed analysis of the decay spectrum of a super heavy X particle," *Astropart. Phys.*, vol. 20, pp. 5–44, 2003.

[262] R. Aloisio, V. Berezinsky, and M. Kachelriess, "Fragmentation functions in SUSY QCD and UHECR spectra produced in top - down models," *Phys. Rev. D*, vol. 69, p. 094023, 2004.

[263] E. J. Copeland, T. W. B. Kibble, and D. A. Steer, "The Evolution of a network of cosmic string loops," *Phys. Rev. D*, vol. 58, p. 043508, 1998.

[264] M. Yamaguchi, "Cosmological evolution of cosmic strings with time dependent tension," *Phys. Rev. D*, vol. 72, p. 043533, 2005.

[265] A. V. Olinto *et al.*, "The POEMMA (Probe of Extreme Multi-Messenger Astrophysics) observatory," *JCAP*, vol. 06, p. 007, 2021.

[266] P. W. Gorham *et al.*, "Constraints on the ultrahigh-energy cosmic neutrino flux from the fourth flight of ANITA," *Phys. Rev. D*, vol. 99, no. 12, p. 122001, 2019.

Vita

Cyril Creque-Sarbinowski was born in Cleveland, Ohio, in 1995. Cyril attended the Cleveland School of Science and Medicine high school at the John Hay Campus between 2010-2013. Cyril then went on to attend the Massachusetts Institute of Technology in 2013 and double majored in Mathematics and Physics. After receiving a Bachelor's degree in 2017, Cyril joined Johns Hopkins University as a graduate student and started working under the supervision of Prof. Marc Kamionkowski. Starting August 2022, Cyril will be a Flatiron Research Fellow at the Center for Computational Astrophysics.